February, 2015

MASTER THESIS

DYNAMIC BEHAVIOR OF HYBRID MAGNETIC SHIELDS FOR SATELLITE-BASED TES ARRAYS

Anne Bergen

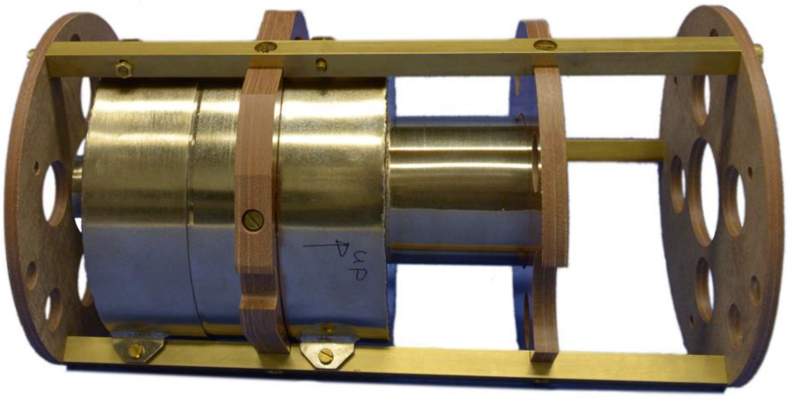

FACULTY OF SCIENCE AND TECHNOLOGY
CHAIR OF ENERGY, MATERIALS AND SYSTEMS (EMS)

EXAMINATION COMMITTEE
Dr. Marc Dhallé
Prof. dr. ir. Marcel ter Brake
Prof. dr. ir. Hans Hilgenkamp

UNIVERSITEIT TWENTE.

Abstract

The core of this MSc assignment is an in-depth experimental study of a hybrid μ-metal/superconductor shield assembly developed at SRON to protect their TES arrays from the magnetic background fields in the satellite-based X-ray observatory Athena.

In technological terms the study served to check whether the present shield is adequate and − as a secondary goal − to validate the relatively straightforward modeling tools that were used in its design. In scientific terms, the assignment was to investigate the dynamic behavior of such shields, i.e. to quantify the influence of the thermal/magnetic history on their behavior. Specifically, the difference between a so-called 'Field-Cooled' (FC) and 'Zero-Field Cooled' (ZFC) superconducting transition was studied. The data provide a baseline for future work, where an attempt shall be made to manipulate magnetic flux during this transition.

In the design phase, SRON developed several models to predict the shielding capability of their hybrid shield, which consists of an outer high-permeability shield and inner superconducting enclosure. 'Static' models solve the Laplace equation for a scalar magnetic potential in the current-free regions of space, taking the shield properties into account by applying appropriate boundary conditions. For the high-μ shield, the chosen boundary condition imposes that parallel magnetic field components at its surface are zero. For the superconducting shield, the normal magnetic field component is assumed to be zero. The tacit assumption is that these static solutions provide a good approximation when the system is ZFC and the superconductor is − and has always been − in the Meissner state. To model the shield assembly in a FC situation, however, it is essential that the history of the sample is taken into account. Accordingly, we call these models 'dynamic'. For a type II superconductor, a FC scenario implies that the vortex state needs to be crossed (even when the final operation point is well within the Meissner state) and flux can remain pinned at microscopic material defects. To describe these effects macroscopically, several models are evaluated for possible use in future work. From these, the 'unconstrained H-formulation' proved to be most promising. This numerical approach rewrites the Maxwell- and constitutive material equations in terms of the auxiliary field $\mathbf{H}$. A suitable relation between the electric field $\mathbf{E}$ and current density $\mathbf{J}$ (e.g. a power law) can then be used to describe the superconductor. Rather than using a power law, SRON modeled the superconductor as an 'ideal conductor', meaning that all magnetic flux that passes through the superconductor before cool-down becomes trapped once it is below its critical temperature.

Such model assumptions (purely parallel or perpendicular fields in the static models and infinite conductivity in the dynamic ones) can only be approximations of reality: the resulting predictions need to be validated. Therefore, a careful experimental campaign was planned and executed. The 'reduced field', defined as the ratio between the externally applied- and internally measured magnetic field, was determined along the shield's axis of rotational symmetry for both the hybrid assembly and for the superconducting shield by itself. In ZFC situations, the agreement between the measured data and the static model predictions is remarkably good.

Measurements of the reduced field on a single superconducting shield revealed a clear difference between the ZFC and FC procedures, regardless of the direction of the applied magnetic field. These deviations are due to the influence of flux that becomes trapped either 'geometrically' (treading apertures in the shield) or 'microscopically' (vortices treading the material itself). The presence of the latter type of flux trapping was confirmed by a hysteresis-like response to alternating fields. Also, the magnitude of the internal magnetic field after cool-down in a transverse applied field could only be explained by taking into account microscopic flux pinning. Both types of flux trapping cannot be described with the static models, but are predicted (at least qualitatively) by the unconstrained H-model. In future work it might be possible to eliminate − or at least reduce − entrapment with a controlled cool-down process involving a large temperature gradient.

As a last, but technologically very important conclusion it was found that the hybrid design meets the Athena mission requirements regardless of the cooling scenario. Even though further developments may allow to eliminate the μ-metal outer shield − enabling a more compact and light-weight design − the present hybrid provides an adequate solution for the shielding of the TES arrays.

Contents

1 Introduction

The first chapter of this MSc report sketches the general background of the assignment. First it is shown that for the developed satellite-based sensors magnetic shielding is an essential part of the design. The TES detectors exploit the superconducting transition, a phenomenon that is used also in their shielding and is thus central in this work. Therefore, basic introduction to superconductivity and the associated terminology is furnished. After a detailed sketch of the problem, the research questions that are addressed in this study are given. The chapter ends with a short description of the structure of the report.

1.1 Background

Space exploration has always fascinated people of a wide variety of ages and cultures. Nowadays it takes a central role in science-fiction novels and movies, but even those who are not interested in fiction have to admit that outer space allures to the curiosity of the human mind: what is beyond (life on) Earth? While the observation of objects in space has been an important part of the history of Science for over centuries, its actual exploration started only in the previous century when the first man-made objects were launched into space. Since then, space exploration missions have been a driving factor in the development of new science and technology. The curiosity to know more about our environment beyond our planet has also brought people together. A good example is the European Space Agency, or in short ESA. This international organization is a platform for cooperation among European states and coordinates the resources of its members to develop Europe's space capability. Recently ESA has selected Athena ("Advanced Telescope for High-Energy Astrophysics") as its second 'large-class' science mission[1]. Citing the ESA director of Science and Robotic Exploration:

"Athena will be a state-of-the-art observatory that will provide a significant leap forward in scientific capabilities compared with previous X-ray missions, and will address fundamental open questions in astrophysics."[1]

– Alvaro Giménez

These 'fundamental open questions' involve the development of stars and galaxies over time, including the formation and evolution of black holes. Athena requires new state-of-the-art scientific instruments to make the mission a success since it pushes the boundaries of current-day physics. As one of ESA's members, the Netherlands contribute to this unique observatory-class X-ray facility, scheduled for launch in 2028. The Dutch Institute for Space Research, SRON, has developed a key part; a 'Focal Plane Assembly' that uses arrays of Mo/Au Transition Edge Sensors (TES) to detect the spectrum of radiation from matter near black holes in order to provide more insight in the origin of the universe[2]. These sensors exploit superconductivity, a phenomenon discovered by the Dutch physicist H. Kamerlingh-Onnes[3]. While measuring the electrical resistivity of mercury at low temperatures, he observed a sudden and complete disappearance of the resistance below a well-defined transition temperature, as is shown in figure 1.1. A TES detector is biased to operate in the steep part of the transition between the normal and superconducting state. Absorption of electromagnetic radiation will lead to a temperature rise and thus to a large change in electrical resistance, so that these micro-calorimeters can detect even a single photon. This does require the superconductor to be correctly biased in its transition regime, which is challenging but possible. Besides temperature, there are however other parameters involved that need to be addressed. The superconductor will also revert to the normal state if the magnetic field or the applied current exceeds a critical limit[3]. This is often represented with a three dimensional graph, the critical surface as shown in figure 1.2. Below the surface the material is superconducting, while above it is in the normal resistive state. Biasing a TES correctly requires control over all three parameters; temperature T, current $\mathbf{I}$ and magnetic flux density $\mathbf{B}$. Controlling T and $\mathbf{I}$ is relatively simple, but control over the magnetic field is not self-evident. Rather than controlling $\mathbf{B}$ actively, it is chosen to shield the sensors from any variation in the external magnetic field.

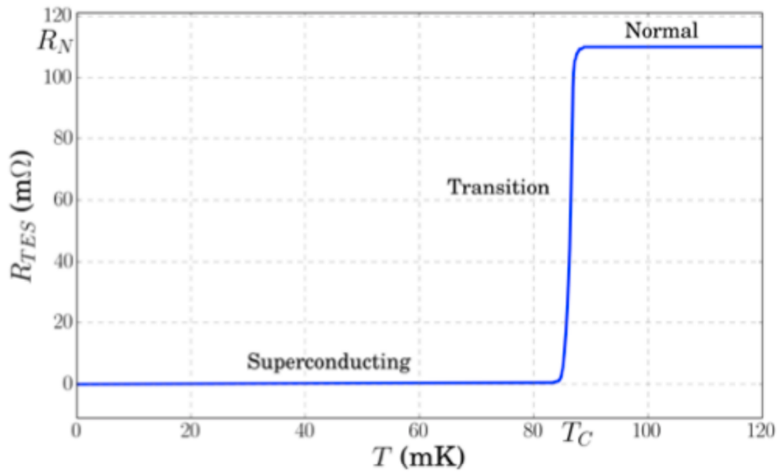

Figure 1.1: *A TES detector uses the transition between the normal and superconducting state. The transition is schematically shown, with on the x-axis the temperature in mK and on the y-axis the electrical resistance in mΩ. A small variation in temperature leads to a large change in resistance[4].*

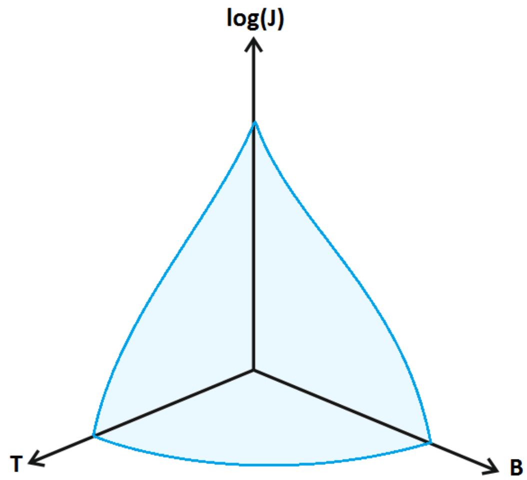

Figure 1.2: *Typical critical surface of a superconductor. Below the surface, the material is in the superconducting state, above it is normal. The surface describes how superconductivity depends on temperature, magnetic field and applied current density.*

There are several possibilities to provide such magnetic shielding, two of them are considered here. First, shielding can be achieved with metals that have a high magnetic permeability (μ). Roughly speaking this causes them to 'attract' magnetic field lines, resulting in a lower magnetic flux density in the desired region[1]. Although this method is relatively straightforward, bulky systems are required to provide sufficient shielding with such high μ-metals, which is not preferred in satellites. The second option is, ironically, to use the same phenomenon that causes the problem in the first place; the interplay between superconductivity and magnetism. In addition to the disappearance of electrical resistance, in sufficient low magnetic field superconductors are also perfect diamagnets: they completely expel field lines from their interior, phenomenon known as the Meissner effect[3]. Type I superconductors exhibit such perfect shielding properties all the way up to the normal state, but their critical temperature T_c and critical field B_c are relatively low so that they are less suited for a satellite design. Type II superconductors generally have higher T_c values and critical fields, but also a more complicated in-field behavior. In addition to the low-field Meissner state, there exists an extra field/temperature region in which magnetic field lines are no longer completely expelled, but enter the material in the form of quantized flux bundles. Such a

[1] This will be specified more precisely in chapter 2.

single 'vortex' is characterized by a supercurrent that circulates around a normal core which points along the external field[5]. Each vortex carries exactly one magnetic flux quantum and can thus be thought of as an isolated flux line that treads the superconductor. Increasing the external magnetic field will cause more vortices to enter the superconductor, up to a point where their normal cores overlap and the superconducting state no longer exists. The external field at which this happens is denoted by the upper critical field B_{c2}. Below a lower critical field B_{c1}, the superconductor behaves similar to a type I conductor and the Meissner state is observed. These different states are shown schematically in figure 1.3.

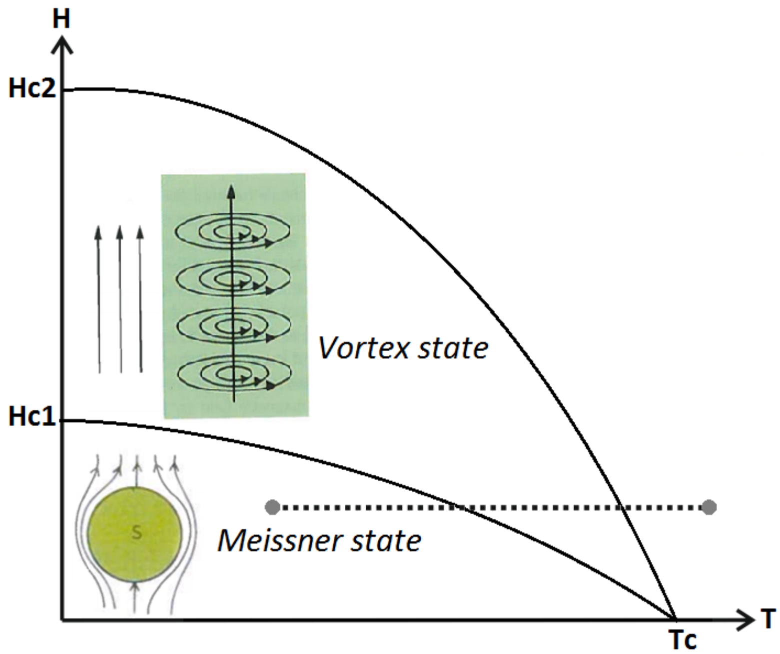

Figure 1.3: *The two states of a type II superconductor shown schematically in a graph with on the x-axis the temperature and on the y-axis the applied field. Below* $B_{c1} = \mu_0 \cdot H_{c1}$ *the superconductor is in the Meissner state and above it is in the vortex state. The dotted line indicates a FC (field-cooling) scenario in which the material enters the Meissner state passing through the vortex state. Figures are adapted from [3].*

Summarizing: TES detectors were designed for the satellite mission Athena, but to work properly they need adequate magnetic shielding which can be provided with a type II superconductor. These superconductors need to be cooled to a sufficient low temperature to ensure that they are in the Meissner state. However, when the material is cooled in presence of an external magnetic field it passes through the vortex state (dotted line in figure 1.3). This may lead to flux entrapment, which in the remainder of this report, is referred to as '*microscopic flux pinning*'[6]. This effect is well understood and even imaged in thin-film structures, where pinning can be associated to energetic surface barriers (figure 1.4)[7]. The exact extent of microscopic pinning in macroscopic structures with a more complex microstructure is unfortunately less well studied, but it may be expected to influence the shielding capabilities of the superconductor.

A second phenomenon that will affect the performance of the superconducting shield is '*geometric flux trapping*'. Suppose that a superconducting ring is placed in an external magnetic field, as schematically shown in figure 1.5. As soon as the external field is removed, Faraday's law dictates that an induced current prevents flux change[3, 5]. As a result, the field inside the ring remains 'frozen-in'. Since the extent of this effect depends on the geometry of the superconductor, it will be referred to as geometric flux trapping.

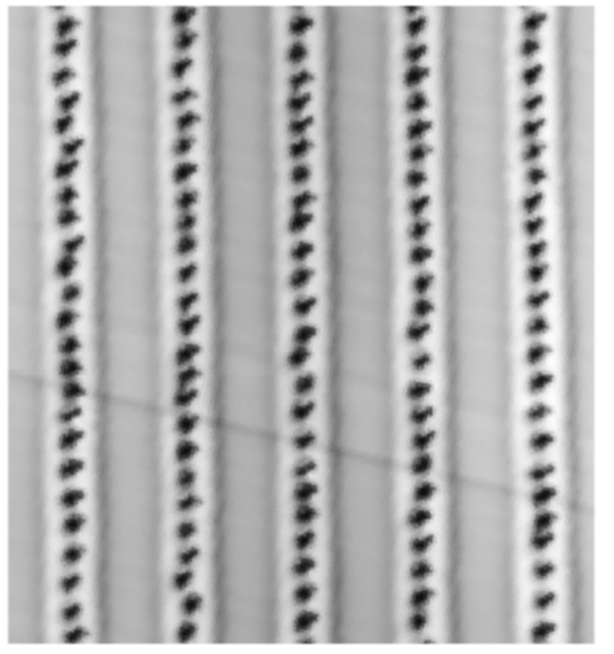

Figure 1.4: *Microscopic flux trapping in field-cooled ($10\,\mu T$) Nb thin-film strips ($30\,\mu m$ wide and $200\,nm$ thick) at $4.2K$. In this scanning-SQUID microscope image, the strips show up as the lighter grey vertical bands, the vortices are the dark dots near their center lines[7].*

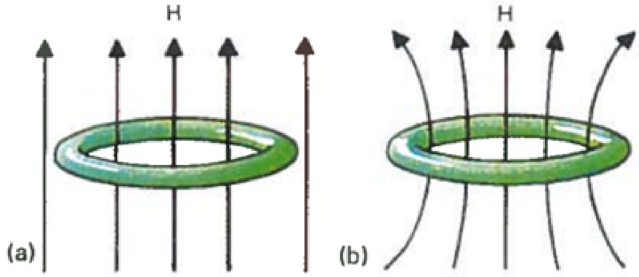

Figure 1.5: *Schematic representation of geometric flux trapping. In a) a superconducting ring is placed in an external magnetic field. In b) this external field is removed. An induced super-current causes the magnetic field inside the ring to be frozen-in[3].*

From a practical point of view, the two flux trapping mechanisms may be considered as a kind of magnetic 'remanence' that influences the magnetic shielding capability of a superconductor. Several techniques were proposed to minimize these effects. Taber et al. proposed a process of iterative expansion of a superconducting foil to reach the required low field for a gravity probe gyroscope experiment[8]. In their setup, a low-field environment is achieved by combining an outer high-μ shield, a superconducting Nb shield and an inner lead-foil shield. This enclosure is deflated before cool-down and inflated once it reaches the Meissner state. Inflating the foil increases the enclosed volume which 'dilutes' the magnetic flux inside it. Multiple iterations are needed to reach the desired low field values. The gyroscope read-out probes are inserted in the shield once the low field is established. Any flux that is present in the probes is flushed by a thermal cycling. As down-sides of this technique, the number of iterative cycles is unknown beforehand; while the system is relatively complex and bulky, making it less suitable for a satellite design.

Fang et al. showed that magnetic flux can be driven out of a thin superconducting cylindrical shell[9]. In their setup a thin shell of Al was kept close to its critical temperature to ensure that the vortices are mobile enough to be swept with a small current. The magnetic field was indeed reduced in this way, but there is a lower limit to the vortex density that can be obtained, imposed by the maximum current that can be applied (the Silsbee critical current for 'fresh' flux entry). Furthermore, this method does not reduce geometric flux trapping, which makes it less suited for the Athena shield that necessarily has relatively large apertures. This latter problem also occurs with the sweeping method proposed by Geng et al., where trapped vortices are moved to any desired location with an Ar laser beam[10]. In addition both methods require additional hardware (weight)[9], a current source[10] or a relative complex laser system.

Instead SRON designed a hybrid shield[2], similar to Xu and Hamilton[11]. In this system an outer high μ-shield establishes a low field environment that reduces the two 'remanence' effects of the inner superconducting shield previously discussed. This combined shield should lower the magnetic flux density below the Athena requirements[2]:

1. A minimum DC reduced field of 10^{-2}, normal to the detector plane (i.e. in the axial shield direction).
2. A minimum AC reduced field of 10^{-5}, normal to the detector plane.

These values are based on a maximum background field in the satellite of $10^{-4}\,T$, estimated from ground based testing. In this report the definition used for the 'reduced field' is:

$$R = \frac{B_{measured}}{B_{applied}} \tag{1.1}$$

To enable SRON's TES involvement in the Athena mission, the most urgent question was: will the hybrid design meet these requirements? More specific: will the μ-shield sufficiently reduce the influence of the two remanence effects in the superconductor? Before this is further examined, however, some additional terminology needs to be introduced unambiguously.

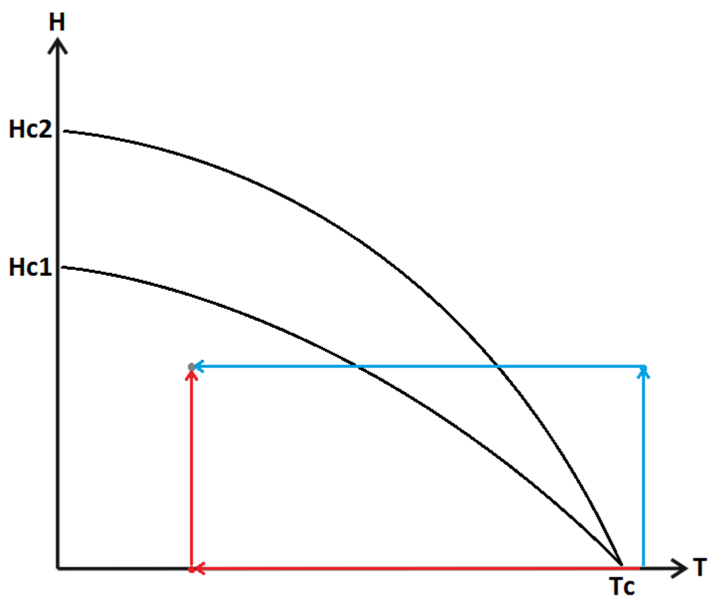

Figure 1.6: *Schematic transition of a type II superconductor with on the x-axis the temperature and on the y-axis the applied field. Below H_{c1} the superconductor is in the Meissner state and above in the vortex state. The blue arrows show the field cooled (FC) situation and the red arrow the ideal zero-field cooled (ZFC) procedure.*

[2]The hybrid design is described in detail in chapter 3.

This report makes a distinction between two cool-down scenarios, schematically depicted in figure 1.6. Ideally, the hybrid design would be cooled in the absence of an external magnetic field. In this situation the vortex regime between B_{c1} and B_{c2} would not be passed so that no microscopic vortex pinning can occur. This ZFC scenario is depicted by the red arrow in the figure. A scenario that is more probable in the actual satellite mission is represented by the blue arrows. In such a FC history an external magnetic field is already present before the hybrid is cooled-down[3].

Because the University of Twente disposes of both sensitive instruments and a magnetically clean environment (see chapter 3), SRON sought a collaboration with UT to validate their shield design. The present MSc assignment was formulated in the frame of this collaboration. The emphasis was on the experimental characterization of a demonstrator shield, but also possible pathways were explored to come to a deeper understanding of the dynamic behavior of a type II superconductor during cool-down in-field. The specific research questions that were formulated are outlined below.

1.2 Research question

The TES detectors that were designed by SRON for the Athena mission need sufficient magnetic shielding to work properly. A hybrid shield system was designed by SRON to meet this requirement. The main goal of the SRON-UT collaboration was to validate the hybrid system. The research questions of this MSc assignment, however, include also more general ones and can be divided in two types.

From a *technological* point of view:

- **Does the present hybrid design meet the shielding requirements?**
- **How do the model predictions compare to the experimental results? (i.e. are the modeling tools used in the design adequate?)**

From a *scientific* standpoint:

- **Is there an observable difference between the shielding properties of the superconductor after a zero-field and field cooled scenario?**
- **If so, which type of model is available (or needs to be developed) to describe the behavior during cool-down?**

These are the main questions that this report seeks to address. Its structure is outlined next.

1.3 Structure of report

Chapter 2 clarifies on what a-priori grounds the hybrid shield system is expected to meet the Athena requirements. The system consists of a high-μ shield and a superconductor. The first question is thus how to model the shielding capacity of these materials. Next we address how to model the combination. Furthermore, how can the materials be modeled in the two distinct cool-down situations? It is shown that the available macroscopic models may be divided in two categories: static or dynamic. The analytical and numerical implementation of both types of model is first reviewed in general terms. Next, the design models used by SRON are explained. It should be stressed that the models themselves were furnished by SRON prior to the MSc assignment and are thus not part of the assignment's original output. However, since one of the main goals of the present work is to validate the design approach experimentally, they are described in some depth. Additionally, we also explore the validity limits of the modeling tools, i.e. we will attempt to delineate what they can and what they can't describe accurately. In the latter case, we will make an inventory of theoretical approaches that may be used in future work.

[3] Athena will orbit the second Sun-Earth Lagrangian point, where the magnetic background field is negligible[12]. However, other instrumentation in the satellite itself may cause field up to 100 μT at the detector location.

Before model predictions and experimental data can be compared, all experimental aspects need to be described in chapter 3. This includes a description of the actual hybrid shield that was assembled at SRON and the experimental validation protocol that was decided upon in discussions between SRON and UT. From the present chapter it is clear that a controlled magnetic field environment is essential in order to do accurate (reduced field) measurements. How such an environment is established is also answered in chapter 3. Finally, the two cool-down situations are described in more detail in this chapter, anticipating future work where the possibility to use only a superconducting shield will be assessed.

The main part of this report is found in chapter 4: the actual experimental results. In this section the most important data are presented and commented upon. The actual interpretation of the results is discussed in chapter 5. In this 'discussion and conclusion' chapter the research questions stated above are answered and an outlook to future development is sketched.

2 Modeling

The previous chapter argued why magnetic shielding is essential for satellite-based TES arrays and formulated the research questions at the basis of this assignment. Here the modeling of the electromagnetic response of the hybrid shield is discussed. Table 2.1 gives an overview of the different model approaches that were used and that are outlined in this chapter. All models solve the Maxwell equations in combination with an adequate description of the materials involved. They can be subdivided in two categories: static and dynamic. A static model reduces the Maxwell equations to the Laplace equation, which may then be solved in numerous ways as discussed in section 2.1. Dynamic models, on the other hand, result in the magnetic diffusion equation which is further discussed in section 2.2. Both approaches require a set of additional relationships that describe the superconductor or the high-μ metal. For the static case, these are a set of boundary conditions. For dynamic models, the constitutive equations may be expressed as a diffusion constant. This is summarized in table 2.1. The specific models that were used by SRON in the design phase of the shield are reviewed in section 2.3. In chapter 4 and 5 of this report they are compared to the experimental data obtained following the two different cool-down situations.

<table>
<tr><th colspan="2">General approach</th></tr>
<tr><td colspan="2">Maxwell equations[1] [13]
$\nabla \times \mathbf{H} = \mathbf{J}$
$\nabla \times \mathbf{E} = -\frac{\partial \mathbf{B}}{\partial t}$
$\nabla \cdot \mathbf{D} = 0$
$\nabla \cdot \mathbf{B} = 0$
[1]For these magnetic models, we assume zero electrical polarization ($e = e_0$) and zero net charge ($\rho_e = 0$)

Constitutive equations [13]
$\mathbf{B} = \mu \cdot \mathbf{H}$
$\mathbf{E} = \rho \cdot \mathbf{J}$</td></tr>
<tr><th>Static models</th><th>Dynamic models</th></tr>
<tr><td>Assumption
$\frac{\partial \mathbf{H}}{\partial t} = 0$

Laplace equation [13]
$\nabla^2 \psi = 0$
$\mathbf{H} = -\nabla \psi$

Solvable with
— Separation of variables [14]
— Green's theorem [19]
— System of dual integral equations [23]

Boundary conditions
— For a superconductor
$\mathbf{H}_\perp = 0$
— For a high-μ metal
$\mathbf{H}_\parallel = 0$</td><td>Assumption
$\frac{\partial \mathbf{H}}{\partial t} \neq 0$

Magnetic diffusion equation
$\nabla \times (\nabla \times \mathbf{H}) = -\frac{1}{D} \frac{\partial \mathbf{H}}{\partial t}$
$D = \frac{\rho}{\mu}$

Solvable with
— A-V formulation [15, 16, 17, 18]
— T-ω formulation [20, 21, 22]
— H-formulation [22, 24, 25]

Constitutive equations
— For a superconductor [15]
$\rho(\mathbf{J}) = \frac{E_C}{J_C} \left(\frac{\mathbf{J}}{J_C} \right)^{n-1}$; $\mu = \mu_0$
— For a high-μ metal[2] [6]
$\rho = \infty$; μ
[2]Reduces to the static case</td></tr>
</table>

Table 2.1: *Overview of the modeling approaches that are outlined in this chapter.*

2.1 Static modeling

This section describes the approach that may be used to derive the shielding capacity of the hybrid system when one does not need to take its history into account. An example is the ZFC procedure described in chapter 1. Since the system is cooled in a zero field environment, the vortex state is not passed during cool-down and no 'remanence' due to geometrically or microscopically trapped flux is expected. Below, we review the possible approaches that can be taken to model such static situation both analytically and numerically.

2.1.1 Analytical description

In addition to adequate shielding, the hybrid system designed by SRON must provide a few other functionalities, i.e. it must have an optical entrance for incoming X-rays and also a wiring fan-out is connecting the TES arrays to the readout electronics. One of the simplest shapes that meets these requirements is an open tube. This results in a hybrid design that consists of an outer cylindrical high-μ metal shield and inner superconducting shield. Although we will see in section 2.3 and in chapter 3 that this is not the optimal shield shape, the high degree of symmetry does allow for a relatively straightforward analytical solution which provides more insight than 'brute-force' numerical modeling. To model the shields analytically, the two materials are treated separately and the entire system is then modeled as a superposition of the two solutions. Moreover, for this description semi-infinite tubes, as shown in figure 2.1, are assessed (in cylindrical coordinates).

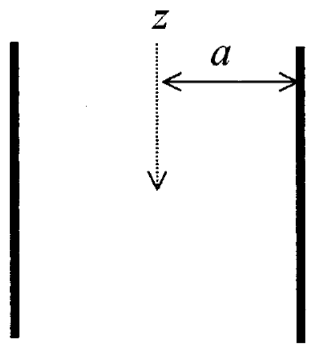

Figure 2.1: *Schematics of a semi-infinite cylinder of radius a, with z the axis of rotational symmetry. This shape is modeled analytically to make a first rough assessment of the shielding capacity of the high-μ metal and superconducting shield[14].*

To determine the shielding capacity of the superconductor and the high-μ metal, the magnetic field inside the cylinder must be determined. In this region there is no current, which permits the use of a magneto-static potential, defined as[13]:

$$\mathbf{H} = -\nabla\psi \tag{2.1}$$

Combination with the Maxwell equation that the divergence of the magnetic flux density is zero, ($\nabla \cdot \mathbf{B} = 0$), yields the well-known Laplace equation[13]:

$$\nabla^2\psi = 0 \tag{2.2}$$

Several approaches to solve the Laplace equation analytically are suggested in literature, e.g. Claycomb[14] solved the Laplace equation by the method of separation of variables, while Vasil'ev[19] used Green's theorem and Badia[23] used a system of dual integral equations. More on the first method is found in appendix A. All solutions require − of course − additional boundary conditions.

A high-μ metal shields the magnetic field by providing a pathway of low magnetic reluctance, as shown in figure 2.2[26]. The magnetic flux density outside the material is described by[13]:

$$\mathbf{B} = \mu_0\mathbf{H} \tag{2.3}$$

While inside the material the following expression holds[13]:

$$\mathbf{B} = \mu \mathbf{H} \tag{2.4}$$

Since magnetic field lines are continuous and closed ($\nabla \cdot \mathbf{B} = 0$) which means that, $\mu > 1$ implies that the two expressions can only be satisfied simultaneously if field lines are 'pulled' towards the material. Inside the sphere of figure 2.2 this leads to a low magnetic field environment. The magnetic reluctance picture allows to make another relevant observation. This reluctance is analogous to the electrical resistance of a circuit and is defined as[27]:

$$R = \frac{l}{\mu A} \tag{2.5}$$

Here l is the length of the magnetic circuit and A its cross-sectional area. It can be deduced that an increase in thickness of the material leads to a lower reluctance and thus to an increase in the shielding capacity. The expression also shows that it is essential to use a material with a high-μ value, such as ferromagnets. In an ideal case, all magnetic flux lines will cross the material. Mathematically, this implies that $\mu \to \infty$ and consequently:

$$\mathbf{H}_{\|} = 0 \tag{2.6}$$

This boundary condition is used in all static modeling approaches involving the high-μ metal (i.e. it is used to solve the Laplace equation and will also be used in a numeric model). Note that this is an asymptotic case. The validity of this assumption is addressed in chapter 5.

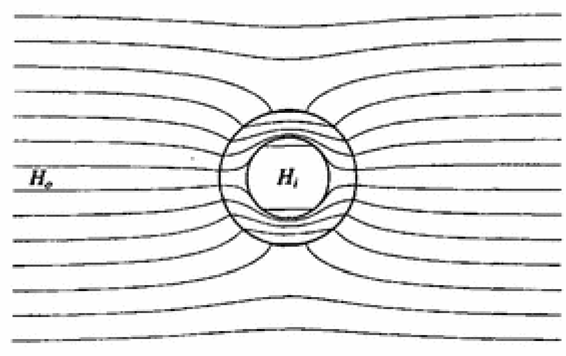

Figure 2.2: *A ferromagnetic sphere in an externally applied field* $\mathbf{H}_0$. *The field inside the sphere,* $\mathbf{H}_i$, *remains small due to the shielding effect of the ferromagnet[26].*

The superconductor, on the other hand, is characterized by the Meissner effect as long as the externally applied magnetic field remains below the first critical value H_{c1}. In the Meissner state, a loss-less shielding current flows on the surface of the superconductor and exactly compensates the external magnetic field in its interior[5]. Nevertheless, the magnetic field does penetrate the superconductor to a certain extent. The associated length scale is the London penetration depth, which is in the order of $100\,nm$ for classical superconductors. Notice that in the absence of demagnetizing effects, this implies that a superconducting layer of less than a micrometer thick results in perfect shielding, whereas reduced field with a μ-metal shield requires a macroscopic wall thickness (equation 2.5). Hence a single superconducting shield would be the preferred solution for satellite designs. However, as mentioned in the introduction, a single superconducting shield could experience significant remanence effects due to geometric or microscopic flux trapping, which will be explored further in chapters 4 and 5. For the present static modeling purposes, we assume that the superconductor is in the 'perfect' Meissner state and that no magnetic field is present in the material. Since field lines are continuous and closed, the following boundary condition must then hold:

$$\mathbf{H}_{\perp} = 0 \tag{2.7}$$

These boundary conditions 2.6 or 2.7 each lead to a unique solution of the Laplace equation. In chapter 4 the reduced field will be characterized with the external magnetic field applied both in the axial- and in the transverse direction to the shield. In appendix A, the static model solutions for the semi-infinite cylindrical shield of figure 2.1 are therefore derived for both field orientations and for both types of material. As an example, in the case of a superconductor in an axial field this results in:

$$\mathbf{H}_{axial,sc} \propto \mathbf{H}_0 \, exp\left(-3.83\frac{z}{a}\right) \tag{2.8}$$

The subscript sc indicates that the model describes the superconductor, a is the radius of the cylinder and $\mathbf{H}_0$ the amplitude of the applied magnetic field. Similar expressions are found for the other situations, all show an exponential decay with a characteristic length-scale that is determined by the radius of the cylinder. Note that for a cylinder of finite length, this exponential decay 'levels off' near the center of the shield[14]. To determine the shielding capacity of even more complex geometries, a piece-by-piece approach may in principle be taken where solutions in separate regions of space are 'stitched together' with the aid of Green's theorem[19]. However, the increased level of mathematical complexity involved tens to obscure the enhanced insight offered by analytical modeling, so that nowadays a numeric approach is generally more preferred.

2.1.2 Numeric approach

Such numeric approaches readily allow more complex geometries to be modeled. To solve the Laplace equation, the same boundary conditions as above are combined with a numerical method. The most commonly used method is the finite element model (FEM) which discretizes a continuous problem in several small elements, known as a 'mesh'[28, 29]. Figure 2.3 illustrates a cylindrical structure cut in tetrahedral elements. At the points where these elements connect, called nodes, the set equation, in the present case 2.2, is evaluated. Errors in the solution may occur due to: the approximation of the domain, the approximation of the solution or numerical computation. The difference between a FEM solution and an exact solution is expressed as the 'accuracy'. A solution 'convergences' when the accuracy increases with increasing number of mesh elements[29]. In the last section of this chapter, the used FEM models designed by SRON will discussed in more detail.

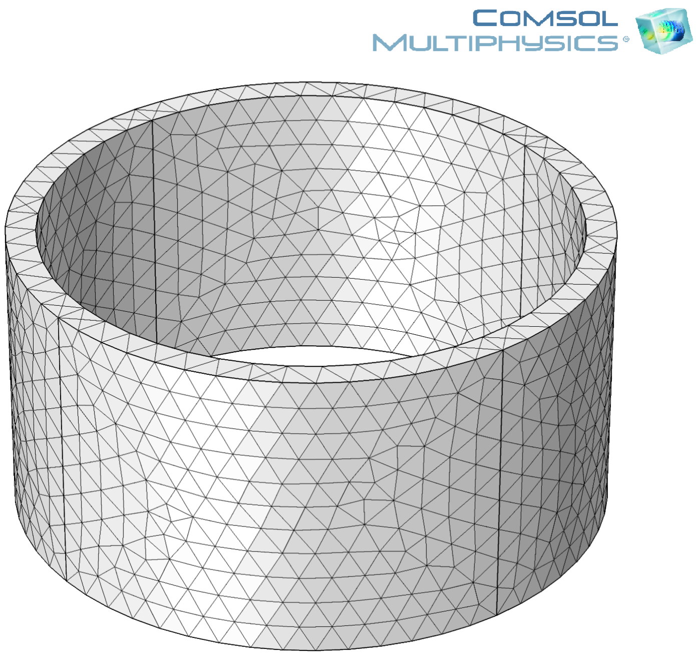

Figure 2.3: *Example of a cylindrical structure cut in tetrahedral elements with the commercial software COMSOL. The Laplace equation can be evaluated at each of the node when sufficient boundary conditions are set (typically at all interfaces and on the surface of a bounding box 'far away'). This is the basis of the FEM.*

2.2 Dynamic modeling

One of the main goals of this study is to assess possible differences in the shield's performance after a ZFC and FC scenario (see chapter 1). The static modeling approach described above is relatively cost-effective in calculation terms, but by definition does not address system history. Therefore SRON also developed a dynamic model. In anticipation of chapter 5, where the validity limits of the models are explored, the underlying assumptions that need to be made are outlined here. It will be shown that the possible presence of microscopically trapped flux requires the superconductor to be modeled macroscopically with a Bean-type critical-state picture. The relation between the macroscopic description and the underlying microscopic physics is given in table 2.2.

Modeling descriptions of superconductors	
Microscopic	**Macroscopic**
Equilibrium, no vortex pinning	Flux flow $\rho = \rho_{FF}$
Non equilibrium, vortex pinning	Bean's critical state model $\mathbf{E} = E_c \left(\frac{\mathbf{J}}{J_C}\right)^n$

Table 2.2: *Relevance between micro- and macroscopic modeling of the states in a type II superconductor, e.g. in equilibrium or non-equilibrium state.*

2.2.1 Analytical description

In chapter 1 it was discussed how in a FC scenario a type II superconductor necessarily passes the vortex state. In this section we argue that in the case of sufficiently strong flux pinning, the vortex state persist also below the lower critical field H_{c1}. Vortex dynamics can be described either macro- or microscopically, but for the present purpose, a macroscopic description is needed. Bean's critical state model was one of the earliest models to describe a type II superconductor on a macroscopic level[30, 31]. He intuited that in a 'hard' superconductor[1] vortices cannot be driven by current-induced Lorentz forces up to a critical current density J_c, and that such currents are therefore carried without flux-flow losses. As a straightforward illustration, suppose that the superconductor is a slab of thickness d and that a magnetic field is applied parallel to it, as shown in figure 2.4.

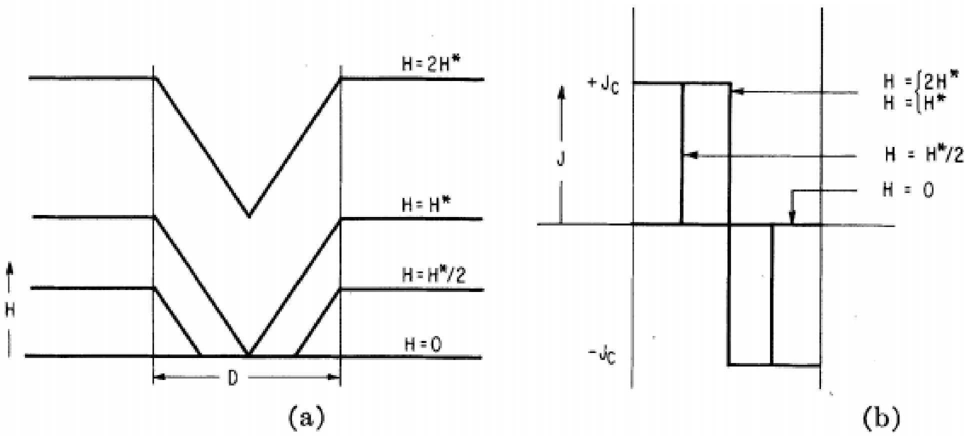

Figure 2.4: *The magnetic flux density (a) and current density (b) in a superconducting slab with a parallel applied field, according to the critical state model first proposed by Bean to describe a type II superconductor on a macroscopic level[31].*

[1] A hard superconductor means that the vortices that penetrate the superconductor are strongly pinned to, for example, material defects[5].

The applied magnetic field is higher than H_{c1}, so that vortices are generated at the slab surface. If this was not opposed by pinning forces (which trap the vortices at material defects, impurities etc.) the Lorentz-type repulsion between them would spread them out over the superconductor's interior, but pinning causes the vortices to 'get stuck' near the surface. As the external field increases and more vortices are generated the repulsive 'magnetic pressure' increases, causing pinned vortices to cascade deeper inwards and establishing a balance between the flux gradient and the pinning forces. In the slab there are now two regions: one with pinned vortices with a current density J_c ($= \frac{1}{\mu_0}\nabla \times \mathbf{B}$) and a flux-free region. This is also illustrated schematically in figure 2.4. Increasing the applied magnetic field further forces the vortices to penetrate deeper in the material. As soon as the current fills the entire superconductor, it is said to be saturated. Reducing the magnetic field at this point leads to a similar situation. The pinning forces oppose the movement of flux, resulting in a flux-frozen region (i.e. a remanent magnetization $\mathbf{M}$) rather than a flux-free region in the superconductor's interior. This cycle is often depicted as a M(H) hysteresis loop as shown in figure 2.5. The figure illustrates that even after the removal of the external field, pinned vortices in the material are revealed by the magnetization of the superconductor. This can be related to the FC situation where the superconductor is cooled through its vortex state. Analogy with the isothermal picture described above suggests that even when cooling causes the applied magnetic field to fall below the lower critical value, vortices are expected to remain present in the material. This justifies the idea to model macroscopic currents and fields in the FC scenario with a critical-state description.

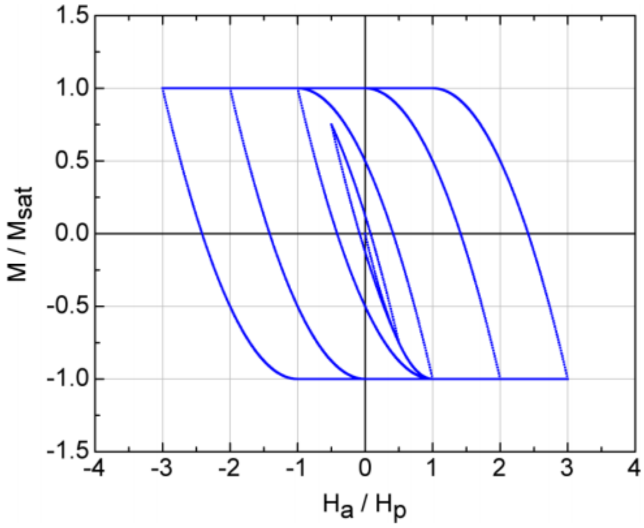

Figure 2.5: *Plot of the magnetization of a hard type II superconductor as a function of applied magnetic field, showing the typical hysteresis loops for a superconducting slab with different maximum applied fields. The magnetization on the y-axis is normalized to the saturation magnetization and the applied field on the x-axis with the penetration field[32].*

For straightforward geometries Bean's critical state model can be used to determine the current profiles and the related magnetic quantities (magnetic field, magnetization etc.) analytically. However, for more complex geometries a numeric approach is needed. Moreover, Bean assumed that the superconductor can sustain current densities up to J_c without any loss whatsoever. Such situation is represented by the thicker E-J characteristic in figure 2.6, where the electric field is plotted as a function of the current density. As mentioned above, currents (or equivalently, flux gradients) exert a Lorentz force on the vortices which is opposed by the pinning forces. In most superconductors, however, vortex movement is e.g. also influenced by thermal agitation leading to 'flux creep'[2]. This is not considered in Bean's model and changes the E-J characteristic as sketched in figure 2.6 by the dotted lines. Several corrections for

[2]Vortices can be thermally activated out of their pinning potential wells and then 'hop' under influence of the Lorentz force to a next pinning site. This process can be described statistically and gives rise to low-level electric fields well before the current density reaches J_c[33, 34].

this behavior were proposed in literature, most commonly by using a power-law type E-J relation. For relatively simple geometries such as the slab in figure 2.5 or cylinders in parallel field it is possible to incorporate a power law analytically to the critical state model, albeit at the cost of increased mathematical complexity. However, for geometries that are more relevant in the context of this report, this needs to be done in numerically.

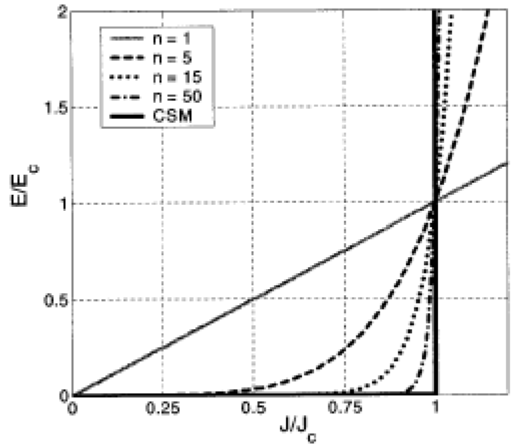

Figure 2.6: *E-J characteristic of a type II superconductor for different values of the power-law index. The thicker black line, with $n \to \infty$, corresponds to Bean's original critical state assumption while $n = 1$ describes a normal conductor[15].*

2.2.2 Numeric approach

In this section the numerical techniques that can be used to model the superconducting shield in a FC procedure are evaluated. As argued in the previous section, this entails modeling the material as a type II superconductor penetrated by vortices. Vortex density gradients can also be thought of as macroscopic currents, making the dynamic case a variation on the eddy-current problem[35]. Before we sketch the numerical strategies that are available, we first describe the typical eddy-current problem and point out the difference (in this context) between a normal metal and a superconductor.

In a typical eddy-current problem a number of assumptions are made: displacement currents are neglected, $e = e_0$, while the conductivity and magnetic permeability are assumed to be independent of the magnetic field. Furthermore, the conducting medium is considered to be isotropic and homogeneous. The Maxwell and constitutive equations can then be combined into a magnetic diffusion equation, mentioned in table 2.1.

$$\nabla \times (\nabla \times \mathbf{H}) = -\frac{\mu}{\rho}\frac{\partial \mathbf{H}}{\partial t} \tag{2.9}$$

As argued above, in a non-equilibrium type II superconductor (i.e. a material with strong flux pinning), the constitutive equation for the electric field needs to be redefined to[15]:

$$\mathbf{E} = E_c \left(\frac{\mathbf{J}}{J_c}\right)^n \tag{2.10}$$

The Maxwell equations with this non-linear constitutive relationship can be solved numerically, although it does require a reformulation of the problem. In literature, various procedures have been suggested, most common are the A-V, the T-ω and the H-formulation. These are briefly described below.

In case of an A-V description of the eddy current problem, the magnetic vector potential $\mathbf{A}$ and scalar electrical potential V are solved simultaneously:

$$\mathbf{B} = \nabla \times \mathbf{A} \tag{2.11}$$

$$\mathbf{E} = -\nabla V - \frac{\partial \mathbf{A}}{\partial t} \tag{2.12}$$

Since:

$$\nabla^2 \mathbf{A} = -\mu \mathbf{J} \tag{2.13}$$
$$\nabla \cdot \mathbf{A} = 0 \tag{2.14}$$

Equation 2.10 can be rewritten to:

$$\frac{\partial \mathbf{A}}{\partial t} - \frac{\rho}{\mu}(\nabla^2 \mathbf{A}) = \frac{\partial \mathbf{A}}{\partial t} - D\nabla^2 \mathbf{A} - \nabla V \tag{2.15}$$

This forms the basis of an A-V formulation. A number of studies have shown that this model reproduces experimental results well[15, 16, 17, 18].

A different approach is to introduce a vector potential $\mathbf{T}$ for the current and combine it with a magnetic scalar potential ϕ:

$$\mathbf{J} = \nabla \times \mathbf{T} \tag{2.16}$$
$$-\nabla\phi = \mathbf{H} - \mathbf{T} \tag{2.17}$$

Such that the following expression can be found:

$$\nabla \times [\rho(\nabla \times \mathbf{T})] = -\mu \frac{\partial}{\partial t} (\mathbf{T} - \nabla\phi) \tag{2.18}$$

Here

$$\nabla^2 \phi = 0 \tag{2.19}$$

Again several authors report a good agreement between these models and analytically determined results[20, 21, 22].

Quite recently the H-formulation has attracted more attention, not in the least because the popular commercial FEM environment COMSOL has implemented the needed properties in its software. In the H-formulation the Maxwell equations are directly formulated in terms of the auxiliary field $\mathbf{H}$, such that:

$$D[\nabla \times (\nabla \times \mathbf{H})] = -\frac{\partial \mathbf{H}}{\partial t} \tag{2.20}$$

The main advantage of this formulation is that it avoids problems related to gauge choice when the magnetic field needs to be determined[22, 24, 25]. Additionally, the boundary conditions can be defined directly in terms of the magnetic field instead of the less intuitive vector potential $\mathbf{A}$ or $\mathbf{T}$. However, the double curl operator can give rise to ill-conditioned matrices at interfaces between different materials. This problem is overcome with the use of ‘edge elements’.

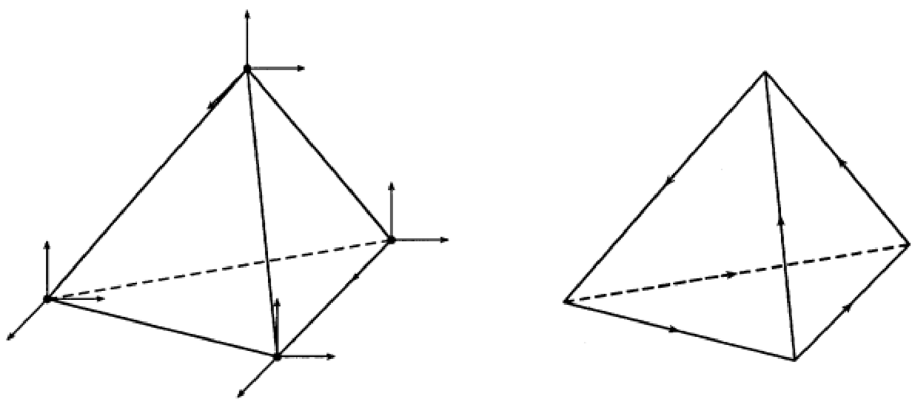

Figure 2.7: *Linear nodal (left) and edge element (right) of a tetrahedral structure[36].*

An extensive description of edge elements is outside the scope of this report. This paragraph gives a brief general introduction to such elements. As mentioned before, a finite element model cuts a structure in numerous cells and evaluates the desired equation at the points where the cells reconnect, the nodes. In case of a vector field, all three components need to be determined, which is schematically shown in figure 2.7, left[36]. In this figure a tetrahedral cell is shown with the four nodes and its coordinate directions. Using these cells implies that all components are continuous functions, which is not unambiguous, a node lies on an interface between several media. Instead, the edge element method redefines the problem along the interconnecting lines between the nodes, the cell edges. The simplest of edge elements, also called Nédélec or Whitney elements, are shown in figure 2.7, right. These elements have six unknowns and are free of divergence, thus avoiding one of the major problems with nodal elements. Such edge elements were used by SRON in their dynamic model of the superconductor, as outlined in the section 2.3.2. However, first the static model designed by SRON is described.

2.3 SRON models

Prior to this work and based on the modeling approaches described above, SRON developed two simulations to predict the shielding properties of their hybrid shield assembly. One of the goals of the present assignment is to make a comparison between these model predictions and the actually observed behavior, so that the validity (limits) of the models can be assessed in view of future design work. Therefore, in this section the SRON models are described in some more detail.

2.3.1 Static model

To mimic the outcome of the ZFC procedure, a static model was designed that solves the Laplace equation with appropriate boundary conditions as outlined in the previous sections. This model is based on a FEM approach implemented on the commercial COMSOL platform. For a transverse applied external field of 100 μT (i.e. thus perpendicular to the axis of rotational symmetry) the predicted magnetic flux density profile is shown in figure 2.8 left, for an axially applied external field of 100 μT (i.e. thus parallel to the axis of rotational symmetry) this is shown in figure 2.8 right and the reduced field along the axis of rotational symmetry is depicted in figure 2.9. This last figure also includes the expected reduced field when the external magnetic field is applied in the transverse direction. From these figures it becomes immediately quite clear that the expected reduced field in the transverse situation is significantly higher (i.e. the shielding capacity is lower, see definition 1.1). This was also analytically determined (e.g. comparing A.17 and A.19 in appendix A) and can be explained by demagnetization effects. Demagnetizing effects are a result of the material's magnetization currents which in turn produces an opposite demagnetization field immediately outside the magnetized object[37]. E.g. for a diamagnetic cylindrical tube in a transverse field this effect causes 'field line crowding' at the aperture of the tube, effectively increasing the field magnitude (visible in figure 2.9 as the 'shoulders' with reduced field > 1 immediately outside the shields in transverse field). Demagnetization fields strongly depends on the geometry of the problem: for an infinite cylinder in an axially applied field it is zero, for the same cylinder in a transverse field its maximum value is as much as half of the applied field. In the axial situation this leads in total to a lower reduced field.

2.3.2 Dynamic model

For the FC situation, SRON developed a dynamic model based on the H-formulation approach discussed in the previous section. Rather than using a full 'superconducting eddy-current' approach combining expressions 2.10 and 2.20, SRON made a few adaptions in order to decrease the computational load while keeping the program suitable for the FC situation. Also this model was implemented in COMSOL, which allows for a time-step profile of the magnetic field. This is shown in figure 2.10; the magnetic field is first built up from zero and then again decreased. In the first stage, the superconductor is modeled in its normal state with a finite resistivity. Once the maximum magnetic field value is reached, the superconducting properties are imposed where after the magnetic field is decreased again. Instead of using the E-J power law 2.10 to describe the superconducting state, SRON models the superconductor

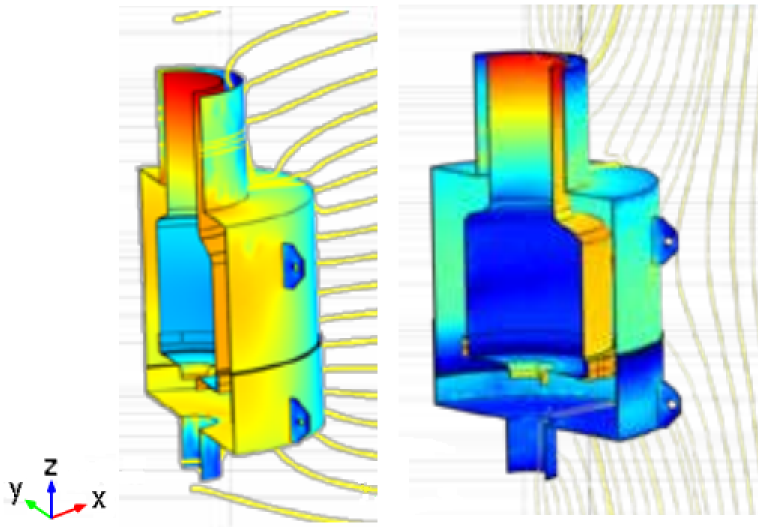

Figure 2.8: *3D cross section of the hybrid shield in a transverse applied field (left) and axially applied field (right) of* $100\,\mu T$*, including the magnetic flux lines predicted by the static COMSOL model provided by SRON.*

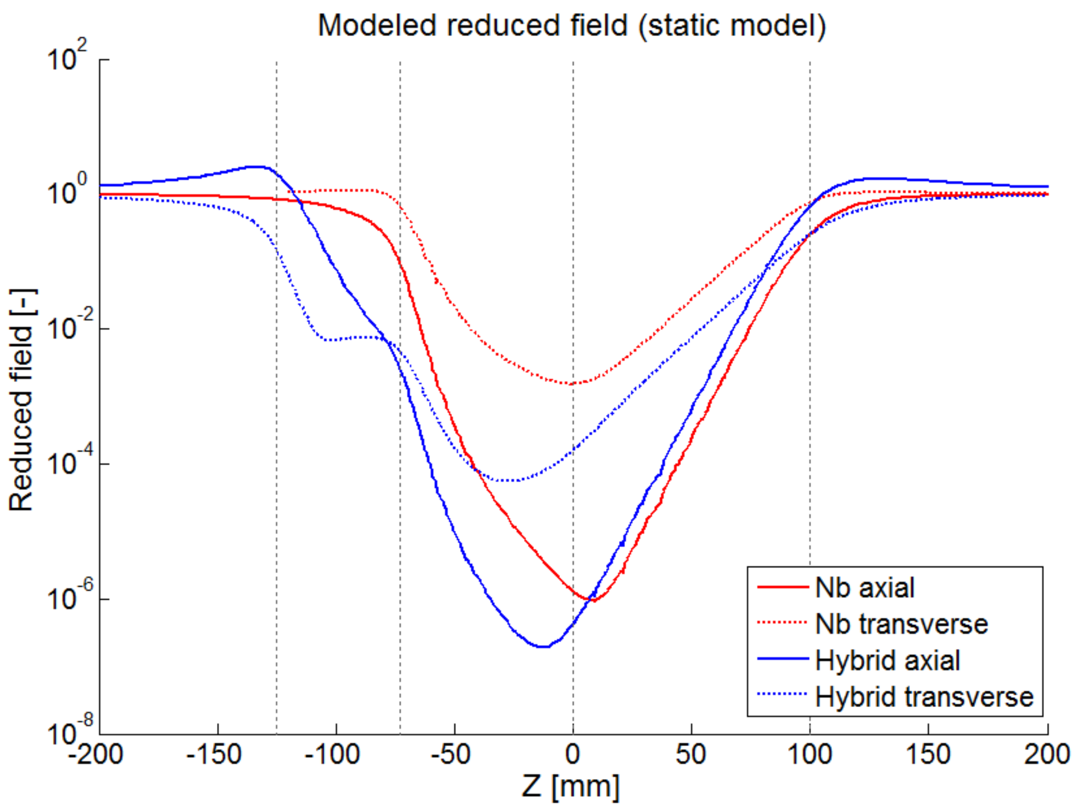

Figure 2.9: *Statically modeled reduced field (measured - divided by applied field) on the axis of rotational symmetry for the hybrid (blue) and superconducting Nb shield (red). Solid lines are for an applied field in axial direction, dotted lines for the transverse direction. The dashed vertical lines indicate – from left to right – the axial position of the bottom aperture in the* μ*-metal; the bottom aperture in the Nb; the TES array; and the top aperture of both materials. The model was provided by SRON.*

as an 'ideal conductor', i.e. a material with zero resistivity[3]. These steps are also sketched in figure 2.11. The ideal conductor has the property that all magnetic flux that penetrates its interior is frozen-in, even after removal of the external magnetic field. It is thus similar to a type II superconductor in the critical state, described in section 2.2.1. However, it should be stressed that flux creep is not included in the model. Whether this is justified will be determined by the experimental results.

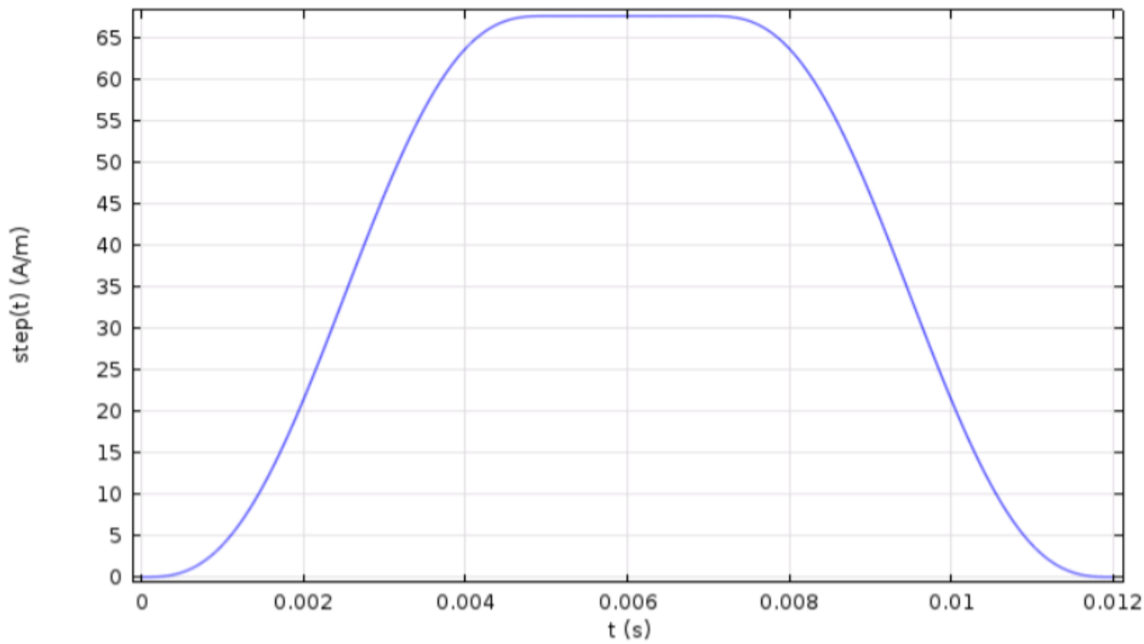

Figure 2.10: *The external field as a function of time in the H-formulation model designed by SRON. At* $t = 0.006\,s$ *the Nb shield is assumed to behave as an ideal conductor. Picture is extracted from the model designed and provided by SRON.*

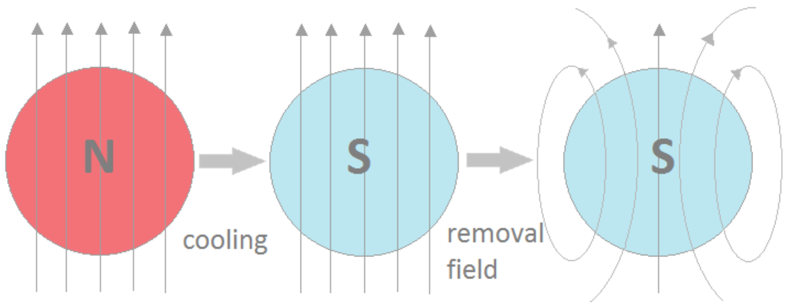

Figure 2.11: *Schematic overview of the FC procedure. A field is applied to the superconducting material in its normal state, then it is cooled and after this cooling the external field is removed during which flux pinning can occur. Note that the model describes the superconductor merely as an ideal conductor, Meissner currents are not taken into account.*

[3]For computational stability, in practice the resistivity is set to the arbitrarily low value of $10^{-15}\Omega m$

3 Experimental Aspects

The main objective of this chapter is to give a brief outline of the experiments done to characterize and validate the full hybrid shield and those that were performed to provide more insight in the dynamic behavior of the Nb shield by itself. The lay-out of the hybrid system, including the outer high-μ metal shield and inner superconducting enclosure, is described and the experimental campaign that was followed is sketched. In order to have a controlled environment, the experiments were done in a magnetically shielded room. Details of this room are also given in this chapter, as well as of the various sensors that were used. This chapter ends with a short description of the demagnetizing procedure that was needed in-between some of the measurements.

3.1 Hybrid system

As outlined in the previous chapters of this report, the hybrid system designed by SRON consists of an inner superconducting shield and an outer high μ-metal. In this section the two shield components are reviewed first separately and then the entire system is discussed.

3.1.1 Nb shield

Figure 3.1a shows a photo of the superconducting shield, in figure 3.1b this shield is shown schematically. X-ray photons can enter the shield via the top aperture to reach the TES detector array, which is located at $z = 0$. This z-axis (chosen as the axis of rotational symmetry and indicated in figure 3.1b) will be used as a reference throughout this report and coordinates will be cited in units of mm. The optical aperture with an inner diameter of $50\,mm$ is located $100\,mm$ above the TES array (i.e. at $z = 100$). At its largest, the shield's inner diameter is $93\,mm$. At the bottom (at $z = -73$), an aperture with diameter $24\,mm$ is needed for the fan-out of the wires connecting the TES array to the read-out electronics.

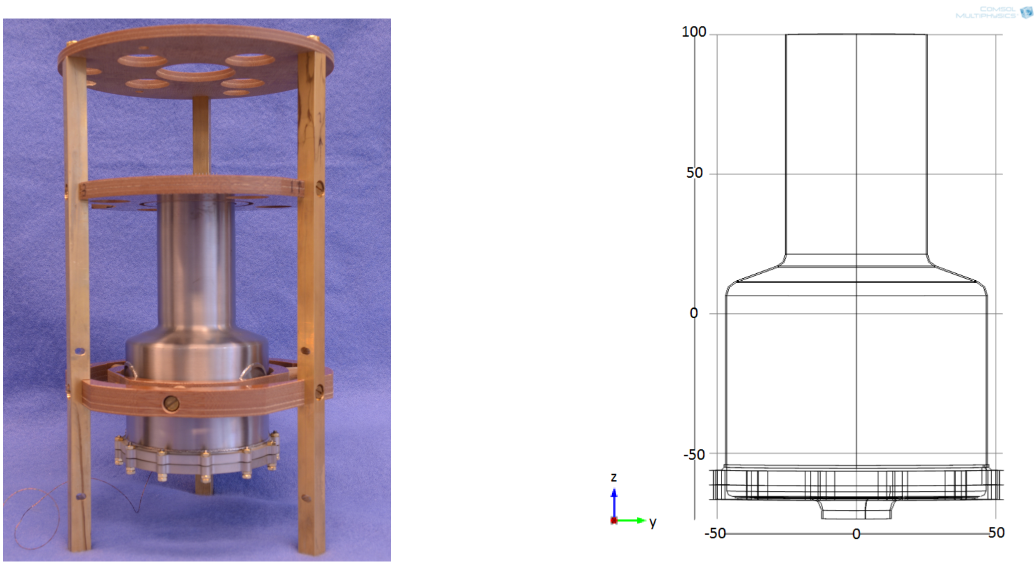

(a) *A photo of the Nb shield suspended in its experimental support structure.*

(b) *Schematic cross-section of the Nb shield in the yz-plane. Scales are in mm.*

Figure 3.1: *The superconducting Nb shield designed by SRON that forms the inner shield of the hybrid system.*

Niobium (Nb) was chosen as the superconducting material since its properties are well-documented and it is also used in other parts of the satellite[1]. Additionally Nb has the highest critical temperature of all pure elements: $T_c = 9.2\,K$ for the bulk metal[3]. Since it is a relatively malleable metal, complex shapes can be made out of it (though with some difficulty). As was discussed in section 2.2.1, a thin-walled structure is sufficient to reach the required shielding level. The typical length scale for the decay of the field inside the material is the London penetration depth, which is 47 nm for Nb[5]. A thickness of less than $1\,\mu m$ would thus suffice from a magnetic viewpoint, but to withstand the considerable accelerations associated with the satellite launch a thicker structure of $100 - 500\,\mu m$ is made. It should also be noted that the superconducting properties of Nb are known to depend on the purity of the material, with critical fields and -temperature generally decreasing with decreasing purity[38].

The superconducting Nb shield was made by Heraeus GmbH with a spin-forming technique[2]. This involves rapidly spinning a pre-formed curved mold together with an initially flat metal sheet. The sheet is slowly pushed against the mold by a stationary wheel. In this way seamless symmetrical structures can be formed out of a single sheet of material[39]. A Nb bottom lid was cold-worked in the same way (the shield must consist out of two detachable pieces to allow the detector to be inserted) and both parts were laser-welded to oxygen-hardened Nb flanges with a sharp knife-edge. When the shield parts are clamped together, these knife-edges cut into a relatively soft seal ring of annealed Nb and thus ensure a continuous superconducting connection between them.

The picture in figure 3.1a also shows the Tufnol/brass support structure that was designed to center the shield in the He bath cryostat and with respect to the outer Cryoperm shield that is discussed next. Tufnol and brass were chosen for their low magnetic signature. The shield is bolted to one of the Tufnol rings at three symmetrically placed treaded Nb washers which were laser-welded over three holes cut in the spin-formed top section.

3.1.2 Cryoperm shield

The outer high-μ metal shield, shown in figure 3.2, was made from the ferromagnetic material Cryoperm[2] This is a high-nickel Ni-Fe alloy that is specifically designed to have optimal magnetic properties at cryogenic temperatures. As shown in figure 3.3, its magnetic permeability increases with decreasing temperature. For comparison, pure Fe has a relative permeability at cryogenic temperatures of 1000, while for Cryoperm it is at least a factor 30 higher.

Figure 3.2: *Photo of the fabricated high μ-metal shield, made from Cryoperm[2].*

The Cryoperm shield was made from 1 mm thick plate, welding the various surfaces together to form a top and a bottom part. The outer diameter of the top part's bottom rim was reduced by machining, as was the inner diameter of the bottom. This way, the bottom lid slides tightly onto the tap part. The magnetic influence of the remaining gap is minimized by extending this overlap region to several centimeters.

[1]More particular Nb is used for the frequency domain multiplexing and for the cold electronics circuits[1].
[2]More specifically, Cryoperm 10.

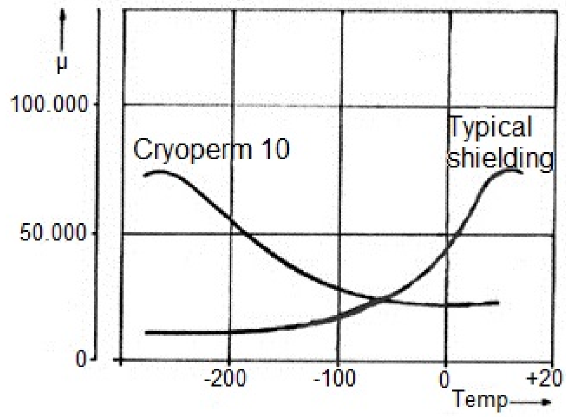

Figure 3.3: *Schematic drawing of the permeability as a function of temperature for Cryoperm and other typical shielding materials[40].*

3.1.3 Hybrid shield

The hybrid shield consists of the superconducting shield and Cryoperm enclosure described above. A photo is shown in figure 3.4a, a schematic cross-section in figure 3.4b. Using the coordinate system introduced with the Nb shield (figure 3.1b), the top aperture of the Cryoperm is positioned at $z = 100$ (just like the Nb) and has an inner diameter of $70\,mm$. Its bottom aperture with $30\,mm$ is at $z = -125$. At its widest, the shields inner diameter is $146\,mm$.

(a) *A photo of the Nb and Cryoperm shield combination.*

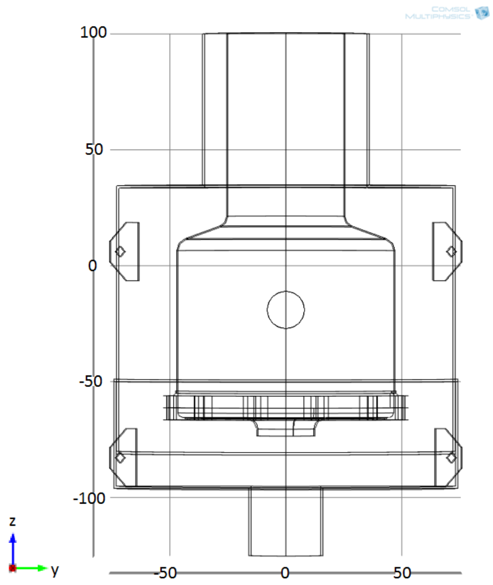

(b) *Schematic of the combined Nb and Cryoperm shields, scales are in mm.*

Figure 3.4: *The hybrid shield that was designed and fabricated by SRON. It consists of an outer high-μ metal shield and an inner superconducting shield.*

The Nb and Cryoperm are centered with respect to each other with the Tufnol ring discussed in section 3.1.1, which fits smoothly in the Cryoperm enclosure. The Cryoperm is loosely screwed to the brass legs of the support structure, allowing sufficient slack to avoid thermal stresses due to differential shrinkage.[3]

[3]Mechanical stresses are known to degrade the performance of high-μ metals[41].

3.2 Experimental campaign

Validation of the hybrid shield was for SRON the major objective of this study and therefore a detailed experimental protocol was agreed upon beforehand. This experimental campaign is outlined here. It should be noted, however, that these measurements were also done on the superconducting shield by itself. As mentioned in the introduction of this report, two different cool-down methods were used. Both shields (hybrid and just Nb) were ZFC and FC, as sketched schematically in figure 3.5. For ease of reference, different T-H states are numbered. The red arrows indicate a ZFC procedure ($0 \rightarrow 3$) while the blue arrows show the FC history ($0 \rightarrow 1 \rightarrow 2 \rightarrow 3$). In the FC procedure the shields are cooled in two field orientations; axial and transverse field. The shields were each time cooled by simply siphoning liquid helium into the cryostat, i.e in a non-controlled fashion. This will be made clearer in section 3.4.4.

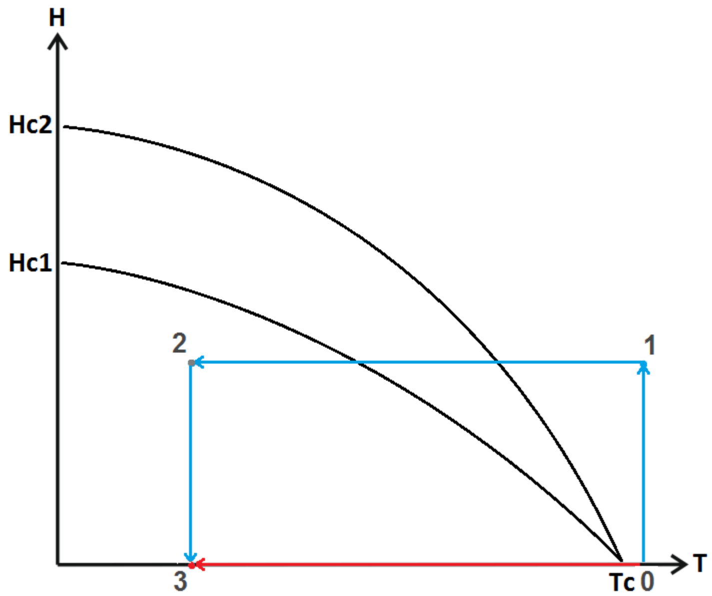

Figure 3.5: *Schematic diagram of the two cool-down procedures. Typical behavior of a type II superconductor is plotted with on the y-axis the applied field and on the x-axis the temperature. The blue arrows indicate the FC procedure while the red arrows describe the ZFC situation.*

In the ZFC situation, as is shown by the red arrow in figure 3.5, the reduced field was determined after the Nb shield was cooled past its superconducting transition point. This reduced field is defined as:

$$R = \frac{B_{measured}}{B_{applied}} \tag{1.1}$$

This means that to determine the reduced field a known magnetic field needs to be applied. Two coil sets, which are discussed in section 3.3, are used to apply a field either in horizontal or vertical direction. A triangular shaped field is applied with these coils at a frequency of 100 mHz and with a maximum amplitude of 100 μT, thus bipolar around point 3 of figure 3.5. However, due to the limit of the power supply for the vertical field coils a maximum applied field of 85 μT is reached. This applied signal is recorded with a data acquisition card, e.g. figure 3.6 top, as well as the measured SQUID's response, e.g. figure 3.6 middle. By plotting these signals against each other, e.g. figure 3.6 bottom, the reduced field is determined from the measured slope. The statistical error in this slope is below 0.1%. The reduced field is measured at different heights along the z-axis.

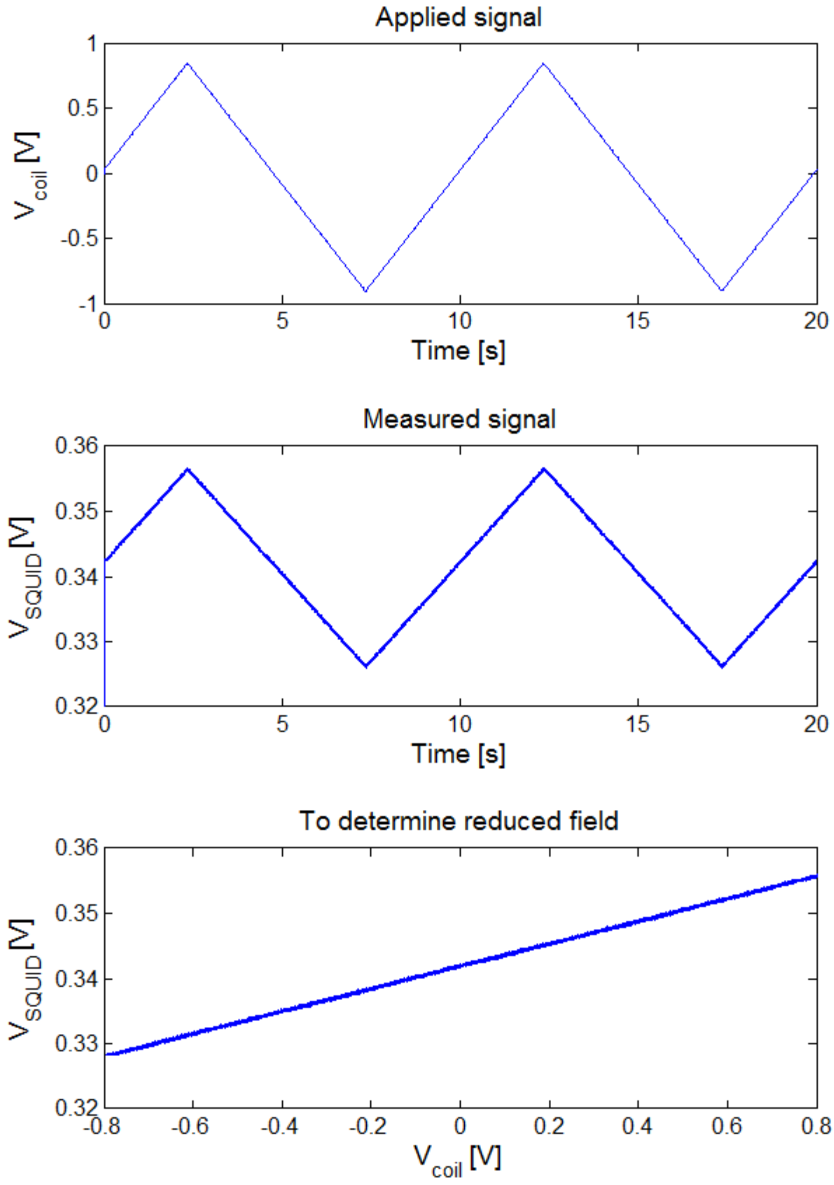

Figure 3.6: *Example of an applied signal (top), measured signal (middle) and the graph (bottom) to determine the slope and therefore the reduced field.*

In the FC situation, shown by the blue arrows of figure 3.5, a DC field was applied in axial or transverse direction with an amplitude of 85 μT and 100 μT respectively before cool-down. The absolute magnetic field was determined with a fluxgate at point 1 in figure 3.5, but also after the shields were cooled in the static field, 2, and after removal of this magnetic field, 3. The fluxgate sensor (section 3.4.2) is less sensitive than the SQUID (section 3.4.1), but has the advantage that it is capable of making absolute measurements. Additionally, after point 3 the reduced field was determined with the SQUID in a similar fashion as for the ZFC situation. Furthermore, off-axis attenuation measurements were done at the detector plane ($z = 0$). In between the four measurements on the hybrid (ZFC and FC; axial and transverse) the Cryoperm shield had to be demagnetized, which is discussed in a next section.

3.3 Magnetically shielded room

In order to correctly characterize the superconducting shield and hybrid design, it is essential to perform the measurements in a controlled magnetic field environment. Especially in the ZFC situation removal of the Earth's magnetic field[4] is required. This was achieved by placing the hybrid or superconducting shield, inserted in a cryostat, in a magnetically shielded room of $2.4 \times 3 \times 4\,m$, shown in figure 3.7. The background field at the center of this room was measured to be less than $10\,nT$. Two coil sets inside the room serve to apply either horizontal (x) or vertical (z) fields. A square coil set with windings in the yz-plane, has a coil constant of $56\,\mu T/A$ and is used to apply horizontal fields. A circular coil set with windings in the xy-plane and with a coil constant of $97.5\,\mu T/A$ applies a field in the vertical direction. Two remarks are in order: 1) we take the xyz-coordinate system the same for the coil description and for the shields (figure 3.1b and 3.4b), i.e. horizontal fields are transverse to the shields, vertical ones axial; and 2) the walls of the magnetic room influence the field profile of the two coil sets. By placing the coils symmetrically in the magnetically shielded room this effect is canceled, which can be achieved for the square coil set. In case of the circular coil set, on the other hand, this was not possible since space above the cryostat was required to move sensor probes up and down. To compensate for this off-symmetry, the following current distribution was applied:

$$I_{top} = 1,305 \cdot I_{bottom} \tag{3.1}$$

This value was determined by modeling the magnetically shielded room with the method of images and verified with preliminary flux-gate measurements without shield. Appendix B describes this simple model, as well as the resulting coil configuration, in more detail.

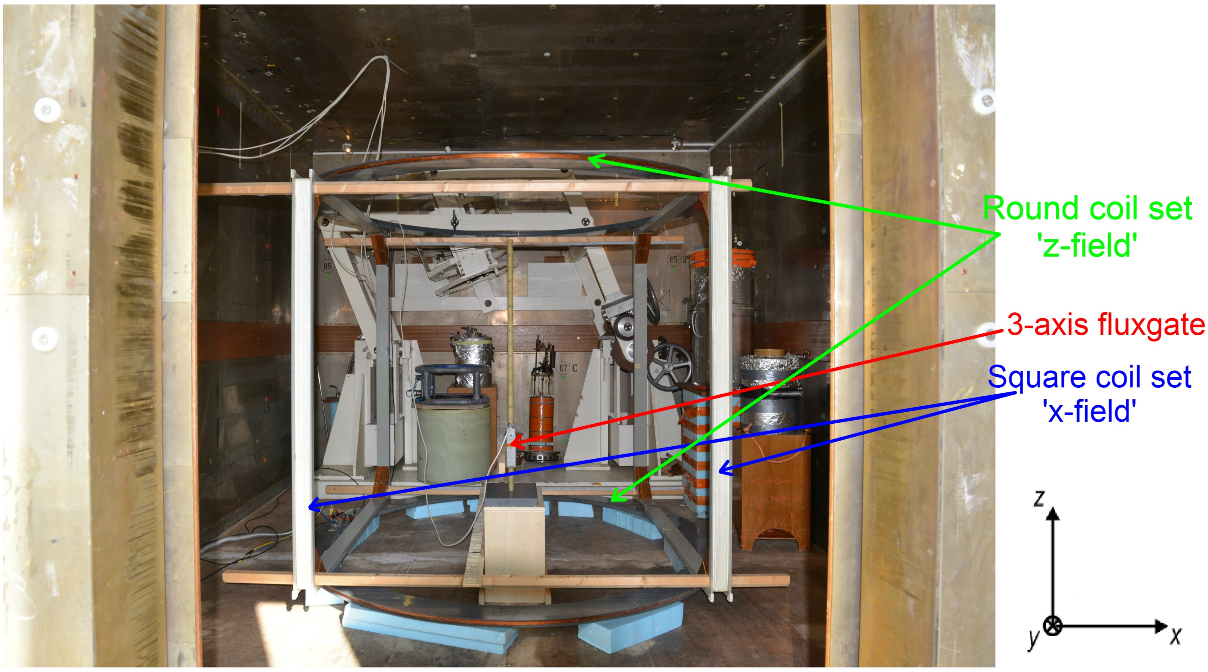

Figure 3.7: *Photo of the magnetically shielded room that provided a controlled magnetic field environment. The two coil sets were placed in this room to apply a homogeneous field either axial or transverse with respect to the shields.*

[4] As a reference the Earth's magnetic field was determined to be roughly $40\,\mu T$

3.4 Sensors

In this section the different sensors that were used to do the measurements are reviewed. This includes the two measurement probes, SQUID and fluxgate, as well as the Hall-probe sensor used to obtain additional off-axis field data. Lastly, the temperature sensor used to determine if and when the shield passed through its superconducting transition will be discussed.

3.4.1 SQUID

For the reduced field measurements, a superconducting quantum interference device or SQUID sensor was used. These sensors are known to have the highest sensitivity of all magnetometers. A SQUID works on basis of a superconducting weak link, also known as a Josephson junction, which is characterized by a reduction in the maximum current that is able to pass the weak link without dissipation. In the dc SQUID two junctions are connected in parallel to form a ring. The maximum current through this device depends on the magnetic flux enclosed by this loop and is maximum when an integral number of flux quanta is enclosed. By measuring the current, the enclosed magnetic field can in principle be determined. In practice, the ring is biased in its superconducting transition and a feedback coil couples sufficient flux into it to cancel variations in the external field and so to keep the voltage across the loop constant (figure 3.8). Variations in the feedback current are thus proportional to variations in the external field. However, the magnetic field in the loop before the device becomes superconducting is unknown, which means that only relative magnetic field measurements can be made[5][5].

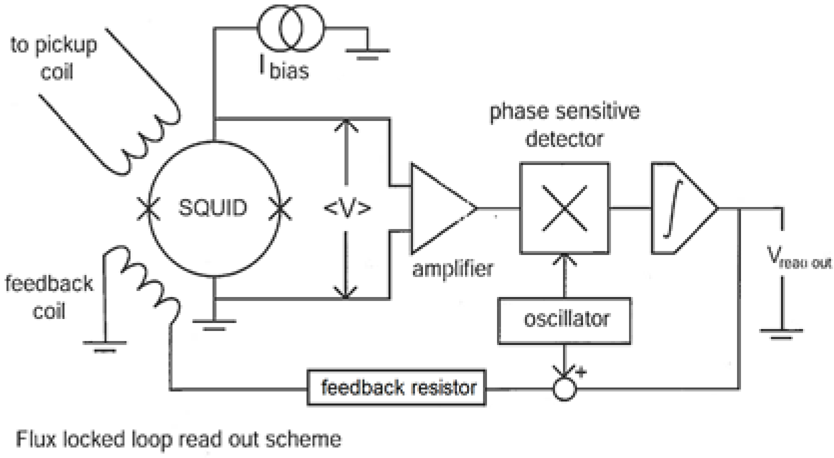

Figure 3.8: *Schematic diagram to sketch the principle of the SQUID and its read-out system[6].*

The commercial '3D' SQUID from the company Supracon AG (figure 3.9) that was used for the reduced field measurements has a sensitivity of $16\, pT/\sqrt{Hz}$ and can measure fields up to $5\,\mu T$ before the signal becomes saturated[42]. To be able to measure field signals at the outer ends of the hybrid, where the shielding is low, a lower applied field was therefore used. The SQUID block attached to its G10 insert is shown in more detail in figure 3.10. With this probe it was possible to measure all three magnetic field components.

The SQUID insert was also modified to do additional off-axis measurements of the reduced field at the detector plane. The SQUID block was moved $13\, mm$ from the insert line, as shown in figure 3.11 and figure 3.12. This was the maximum the SQUID could be moved as the probe still needed to fit through the top aperture of the hybrid shield. For these off-axis measurements the probe was rotated 360° and data points were measured every $22,5°$.

[5]Physically flipping over the SQUID (as done at SRON) allows to make absolute readings, but the present set-up did not have sufficient space for this.

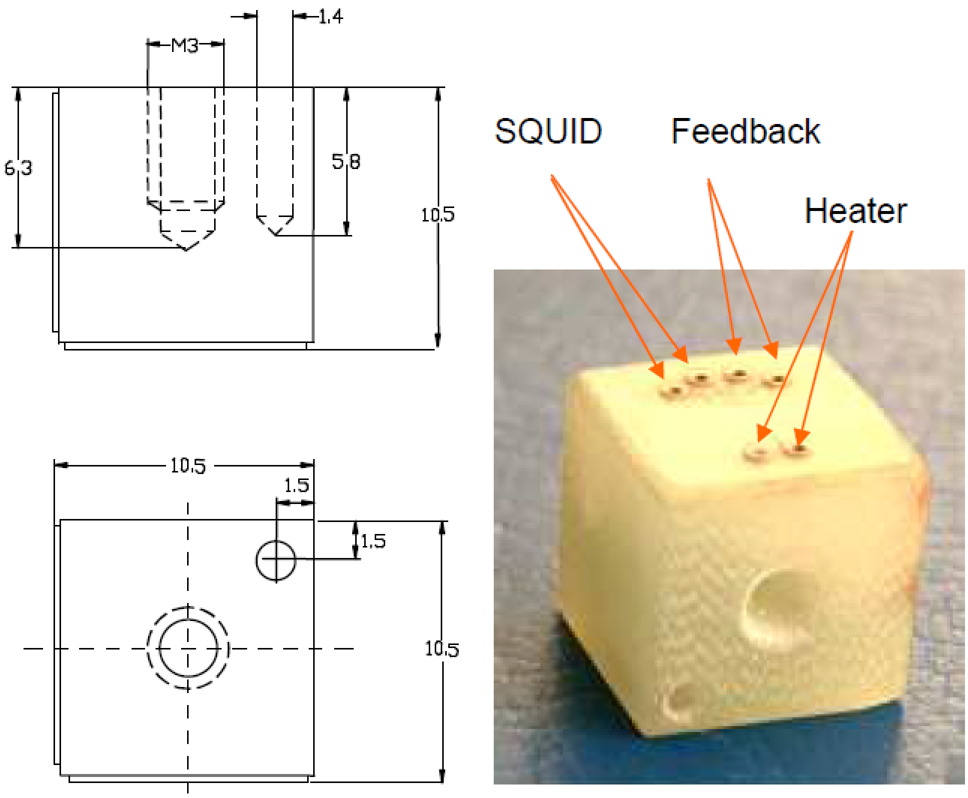

Figure 3.9: *Schematics of the commercially used SQUID (left) and a picture (right) from the company Supracon AG[42].*

Figure 3.10: *Photo of the SQUID block insert used for the reduced field measurements.*

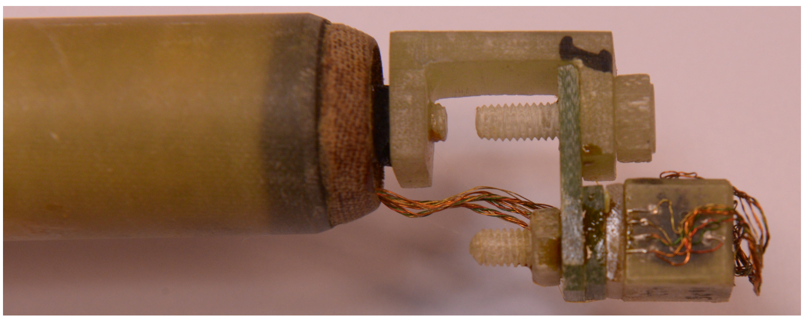

Figure 3.11: *Photo of the SQUID block after it was modified to be able to do off-axis measurements.*

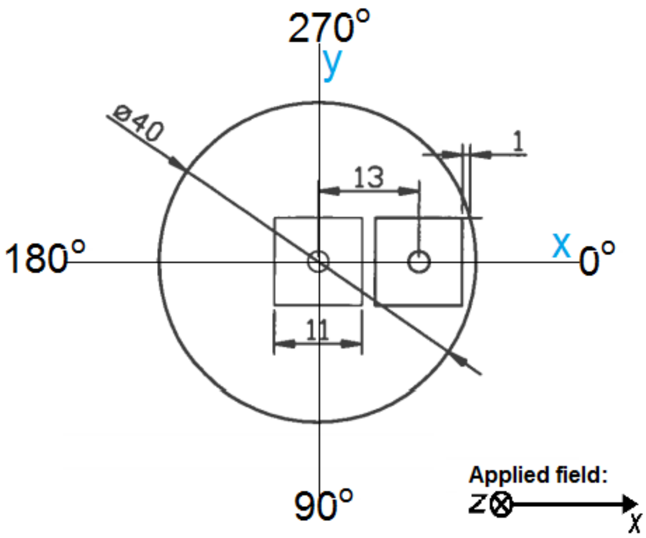

Figure 3.12: *Schematics of the displacement of the SQUID block for off-axis reduced field measurements including the different angles with respect to the applied field.*

3.4.2 Fluxgate

For the absolute magnetic field measurements used to determine flux profiles in the FC procedure a fluxgate had to be used since, as discussed above, it was difficult to measure absolute fields with the SQUID. The principle of the fluxgate is schematically shown in figure 3.13. This type of magnetometer consists of a magnetically susceptible core and two coils. With the first coil an AC field is applied that periodically saturates the core. The second pick-up coil will detect this change in magnetization as an electrical voltage. In case of a neutral background, the input current and output voltage will match. However, when an external field is applied to the core it will influence its response to become more easily saturated in one direction, which can be detected with the pick-up coil. The two coils are now no longer in sync and the difference in the two signals is a direct measure for the external magnetic field[43].

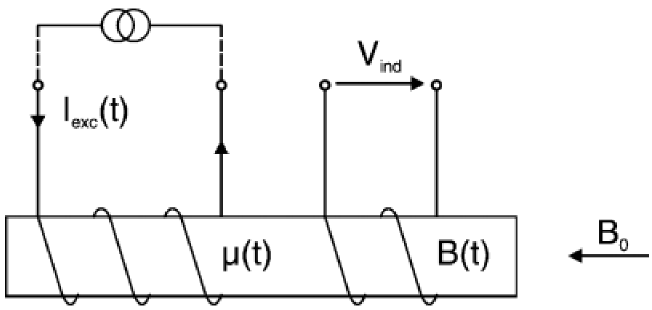

Figure 3.13: *Schematic diagram to sketch the principle of the fluxgate magnetometer. An alternating current is applied with one of the coils to the magnetically susceptible core and detected by the second coil.[43]*

The commercial fluxgate sensor that was used in this project was of the type Bartington MagF. It had a sensitivity of 1 nT and can measure fields up to 200 μT over a wide temperature range from liquid helium temperatures to $+30°C$[44].

3.4.3 Hall probe

A Hall probe sensor from the company ChenYang Technologies GmbH & Co. KG was used to provide additional off-axis field data (section 4.2.4). This sensor works on basis of the Hall-effect (figure 3.14). A conductor carries a current I and is placed in an orthogonal magnetic field, which exerts a force on the electrons and thus creates a small voltage across the plate. This can be measured and related to the applied field[45].

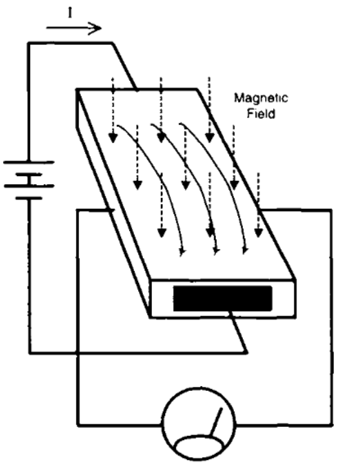

Figure 3.14: *Schematic diagram of principle behind Hall-effect sensors. A magnetic field will deflect the electrons of the applied current and induce a voltage across the plane[45].*

The used Hall-sensor is depicted in figure 3.15; it was placed on the 'shoulder' of the Nb shield. This sensor had a sensitivity of $\sim 2mV/mT$, however, it should be stressed there is some uncertainty on this calibration factor at cryogenic temperatures.

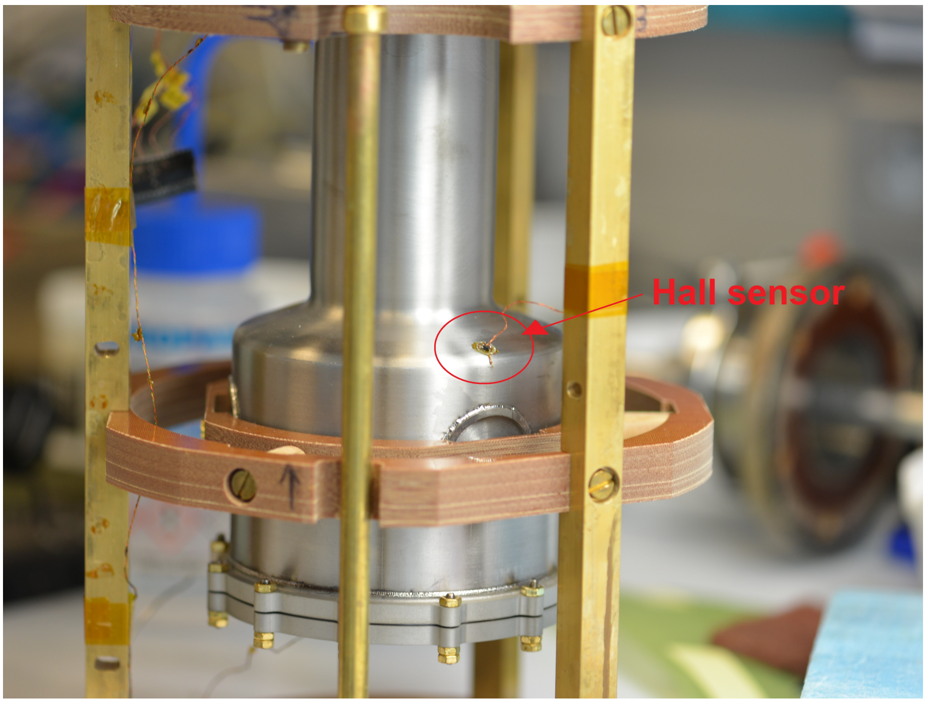

Figure 3.15: *Photo of the Hall sensor placed on the 'shoulder' of the Nb shield to get additional off-axis field data.*

3.4.4 Temperature sensor

A temperature sensor was placed on the Nb shield to determine if and when the Nb passed through its superconducting transition. This sensor is made from germanium and calibrated at cryogenic temperatures (up till $30\,K$). It was placed on the bottom of the shield. As mentioned above, the superconducting shield was cooled by siphoning liquid helium into the cryostat. In figure 3.16 the temperature during a typical cool-down is plotted as a function of the relative time in seconds. The red line marks the critical temperature of Nb. The cooling rate is of the order of $1K/s$. This is, however, not comparable to the cool-down for an in-flight situation. Future work will focus on better control of the temperature, both as a function of time and as function of position.

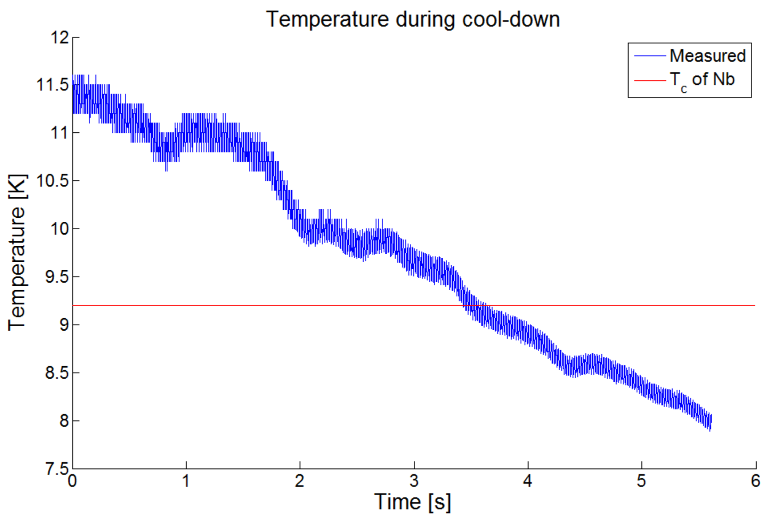

Figure 3.16: *Temperature as a function of time recorded for a typical cool-down process. The red line indicates the T_c of Nb.*

3.5 Demagnetization process

In between the measurements on the hybrid the Cryoperm shield had to be demagnetized, as this ferromagnetic material may have a remnant magnetization, e.g. $\mathbf{M} \neq 0$ if $\mathbf{H} = 0$, also schematically shown in figure 3.17. To be able to compare the different measurements on the hybrid it is essential that all measurements start from the same initial state, thus without a magnetization present. This also ensures that any unknown pre-magnetization does not influence the results.

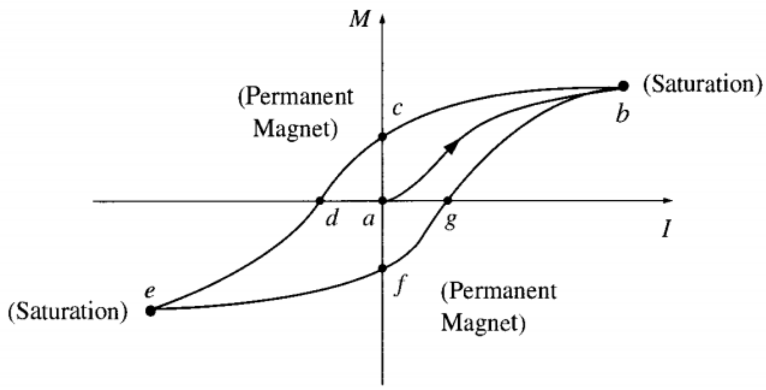

Figure 3.17: *Schematic plot of a typical hysteresis curve, where* $\mathbf{M}$ *is plotted as a function of* $\mathbf{I}$.*[13]*

For the demagnetization process five turns of copper wire were wound through the bore of the Cryoperm, as shown in figure 3.18. This wire was fed with a sinusoidal current at a frequency of 100 mHz and with a high enough amplitude to create a field of $> 100A/m$. The amplitude of the current was slowly brought down to zero to decrease the hysteresis curve as shown in figure 3.17 until no magnetization is left. This was done inside the magnetically shielded room.

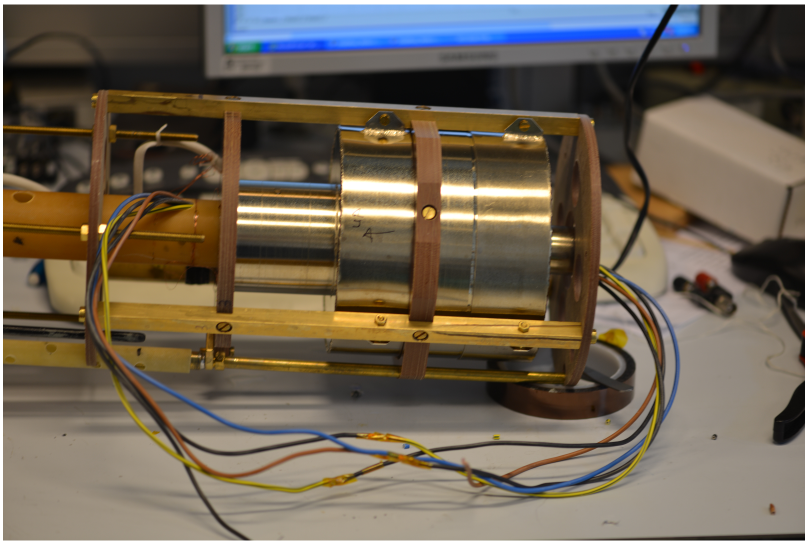

Figure 3.18: *Setup used to demagnetize the Cryoperm: a wire was wound through the bore and fed with a sinusoidal current that was slowly brought down to zero. This was done inside the magnetically shielded room.*

4 Results

The previous chapters described the models that were used and the experimental campaign that was followed. In this chapter the focus is on the experimental results. These fall in two categories: ZFC and FC measurements of the superconducting shield and hybrid design. Reduced field measurements were done for both cool-down procedures, while in the case of the FC situation also the absolute magnetic field was determined along the axis of rotational symmetry. To verify model predictions further, in this FC situation the field was determined off-axis as well. Furthermore, a measurement of the absolute magnetic field as a function of time after the superconducting shield was cooled in an external field provided information on possible flux creep. The results that were obtained from these measurements can be used to (1) investigate the dynamic behavior of superconductors (2) validate the hybrid design. In the next chapter the results are summarized and conclusions are drawn while in this chapter the obtained data are presented according to the structure listed in table 4.1.

Cooling	**Shield**	**Experiment**	**Section**	**Figure**
ZFC	Nb	$R_{\|\|}(z)$	4.1.1	4.1
ZFC	Nb	$R_{\perp}(z)$	4.1.1	4.2
ZFC	Hybrid	$R_{\|\|}(z)$	4.1.2	4.3
ZFC	Hybrid	$R_{\perp}(z)$	4.1.2	4.4
$FC_{\|\|}$	Hybrid	$B(0,0,z_0;t)$	4.2.1	4.5
$FC_{\|\|}$	Nb	$B(0,0,z)$	4.2.2	4.6
$FC_{\|\|}$	Nb	$R_{\|\|}(z)$; $R_{\perp}(z)$	4.2.2	4.7
$FC_{\perp}$	Nb	$B(0,0,z)$	4.2.2	4.9
$FC_{\perp}$	Nb	$R_{\|\|}(z)$; $R_{\perp}(z)$	4.2.2	4.10
$FC_{\|\|}$	Hybrid	$B(0,0,z)$	4.2.3	4.11
$FC_{\|\|}$	Hybrid	$R_{\|\|}(z)$; $R_{\perp}(z)$	4.2.3	4.12
$FC_{\perp}$	Hybrid	$B(0,0,z)$	4.2.3	4.13
$FC_{\perp}$	Hybrid	$R_{\|\|}(z)$; $R_{\perp}(z)$	4.2.3	4.14
$FC_{\|\|}$	Nb	$B(s_0,\phi,0)$	4.2.4	4.15

Table 4.1: *Overview of the experiments done and presented in this chapter, where $FC_{||}$ means field cooled in axial DC field, $FC_{\perp}$ field cooled in transverse DC field, $R_{||}$ the reduced field with an axially applied field and $R_{\perp}$ the reduced field with a transverse applied field.*

4.1 ZFC procedure

Ideally, the hybrid system would be cooled in a zero-magnetic field environment in order to prevent the superconductor from passing through its vortex state during cool-down. Although this is not possible in a satellite, experiments were done after this ZFC procedure to provide a useful benchmark, which will allow a comparison with the FC procedure. In this section the results for the ZFC procedure for both the superconducting and hybrid shield are presented.

4.1.1 Superconducting shield

The Nb shield, described in the previous chapter, was ZFC where after a field of 85 μT and 100 μT was applied in axial (z-direction) and transverse direction (x-direction), respectively. Figure 4.1 and 4.2 show the measured reduced field in these two situations for all three magnetic field components and compares the data to the static models that were provided by SRON. In the models only the reduced field of the component in direction of the applied field is shown. The experiments were done with the SQUID: the measured signal was plotted as a function of the applied magnetic field and the slope was used to calculate the reduced field, as was discussed in section 3.4.1. These figures show a good agreement between the predicted and measured results. As expected, the reduced field for an applied field in the transverse direction is higher than in axial direction (see section 2.1.1). The required axial reduced field of 10^{-5} is reached. Scattering in the data of the x- and y-components can be explained by small alignment variations in between the measurement points due to the vertical displacement of the probe. Additionally, the applied magnetic field is not perfectly aligned, see appendix B. This is also the case for the hybrid ZFC situation, the results of which are shown in the next section.

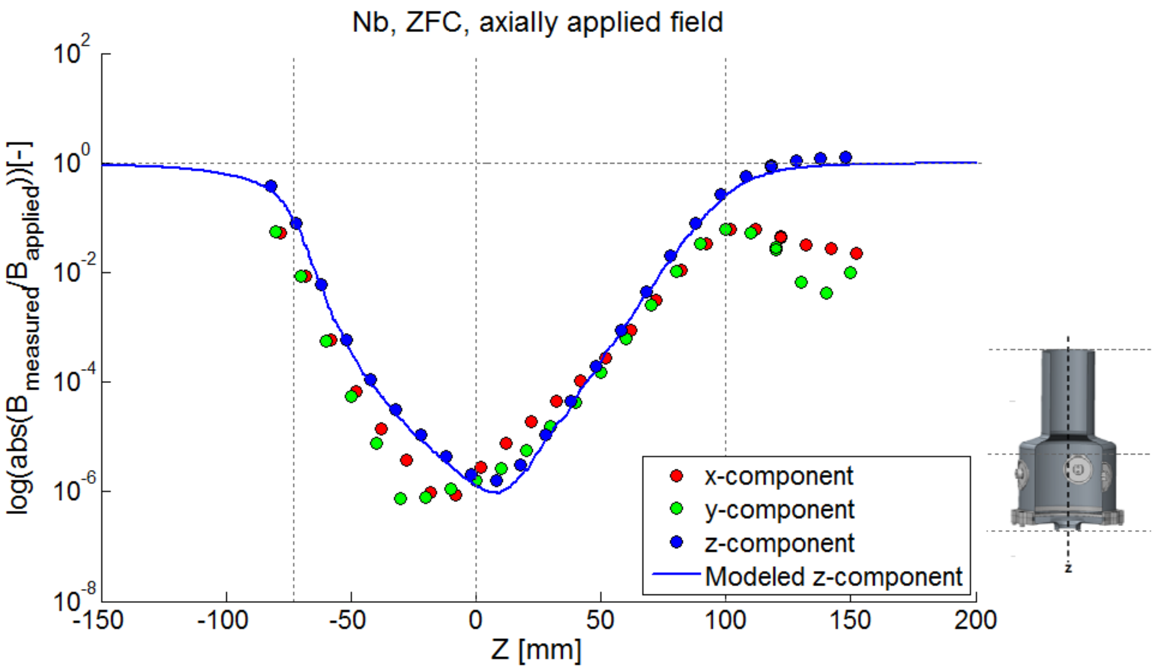

Figure 4.1: *Measured reduced field along the z-axis for the ZFC superconducting shield in case a magnetic field was applied in the axial direction of maximum* 85 μT. *All three field components were measured; the red, green and blue data points correspond to the x-, y- and z-components respectively. The blue line represents the modeled reduced field for the z-component that was determined with the static model provided by SRON. The vertical dotted lines indicate the bottom aperture, the TES array and the top aperture. Included is the schematics of the Nb shield.*

4.1.2 Hybrid system

A similar ZFC procedure was also used for the hybrid system. The reduced field for an applied field in axial direction is shown in 4.3, for a field in transverse direction in figure 4.4. Again there is a good agreement between the measured data and statically modeled predictions, especially for the measurements in an axial field. A minimum reduced field of $\sim 10^{-7}$ is reached in this situation, well below the requirements. In case of a transverse applied field the measured and modeled results show some deviation, which can be due to several effects. Although it is possible that there is some uncertainty in the position of the SQUID, the estimated error for this is $\pm$ 2 mm, i.e. not enough to explain (all of) the deviation. As can be determined from figure 4.3, the main deviations occur near the connection between the two parts of the hybrid shield and below the superconducting shield. Comparison with figure 4.2 shows that at this position, the high-μ metal is the major cause of magnetic field variation. The differences might well be explained by a non-ideal fit between the two shield halves or by a local change in the value of the permeability of the model and the actual permeability of the shield. This magnetic permeability depends on several factors, such as temperature, magnetic field, stress etc. In the next section the results for a FC procedure are presented, which is more representative for the in-flight situation.

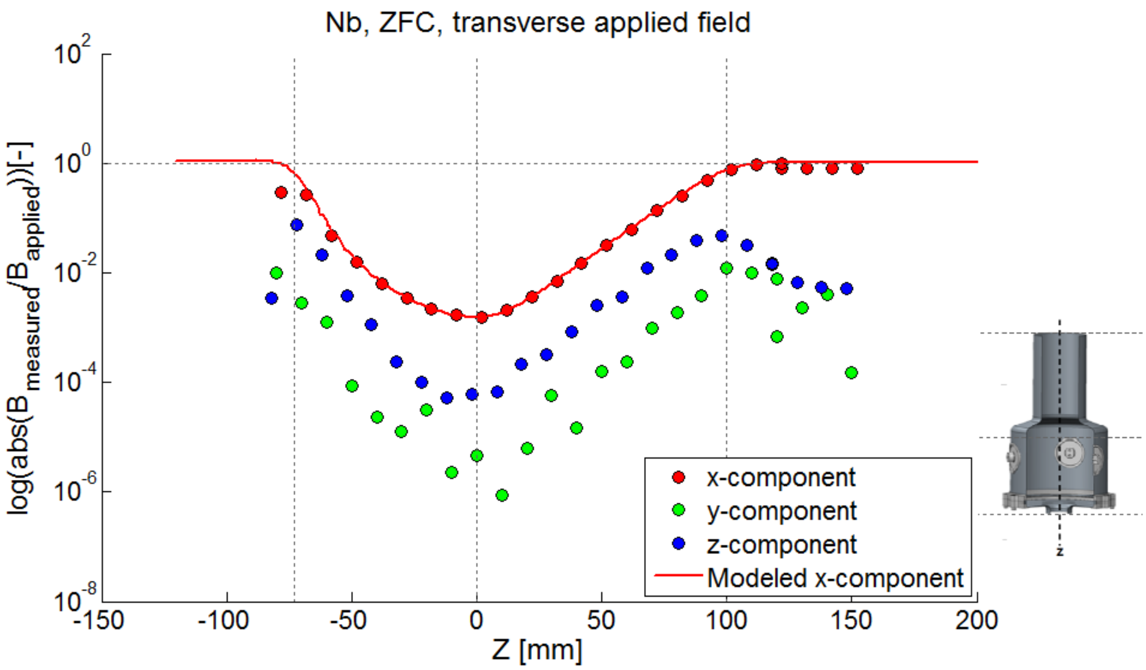

Figure 4.2: *Measured reduced field along the z-axis for the superconducting ZFC shield in a magnetic field applied in transverse direction. The red line represents the modeled reduced field for the x-component predicted by the static SRON model.*

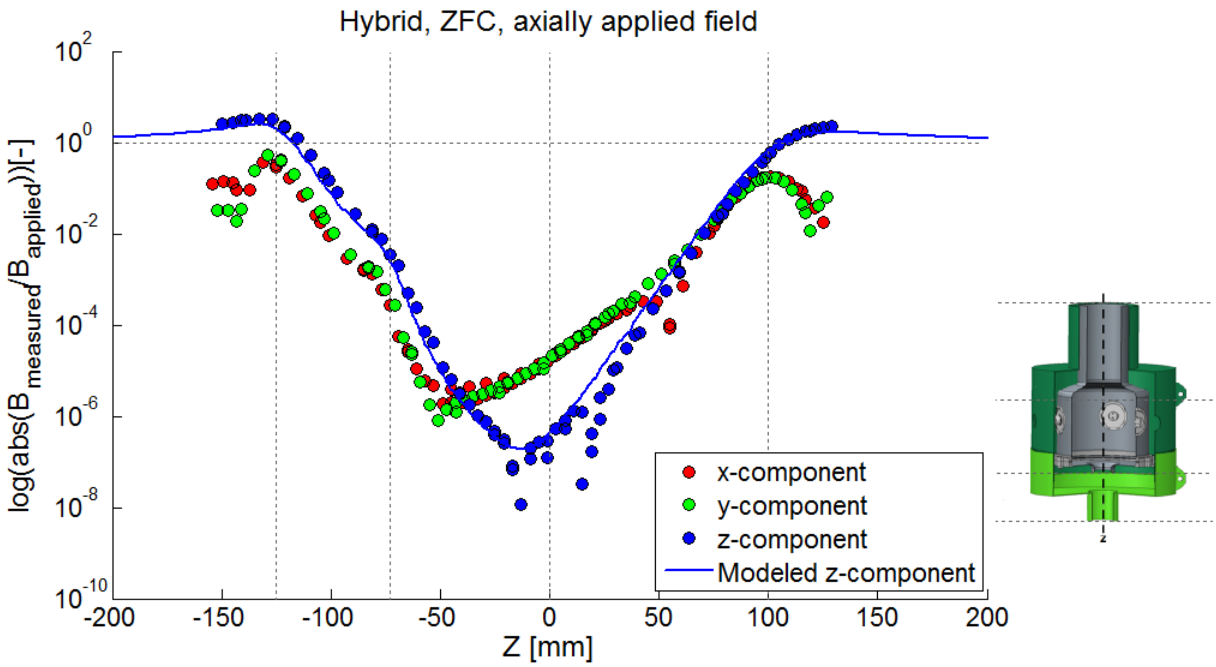

Figure 4.3: *Measured reduced field along the z-axis for the ZFC hybrid in an axial field. All three magnetic field components were measured; the red, green and blue points are the x-, y- and z-components, respectively. The blue line represents the reduced field for the z-component that was predicted by the static SRON model. The dotted vertical lines indicate, from left to right, the position of the bottom Cryoperm aperture, the bottom Nb aperture, the TES array and the top apertures of both enclosures. Also included is a schematic of the hybrid.*

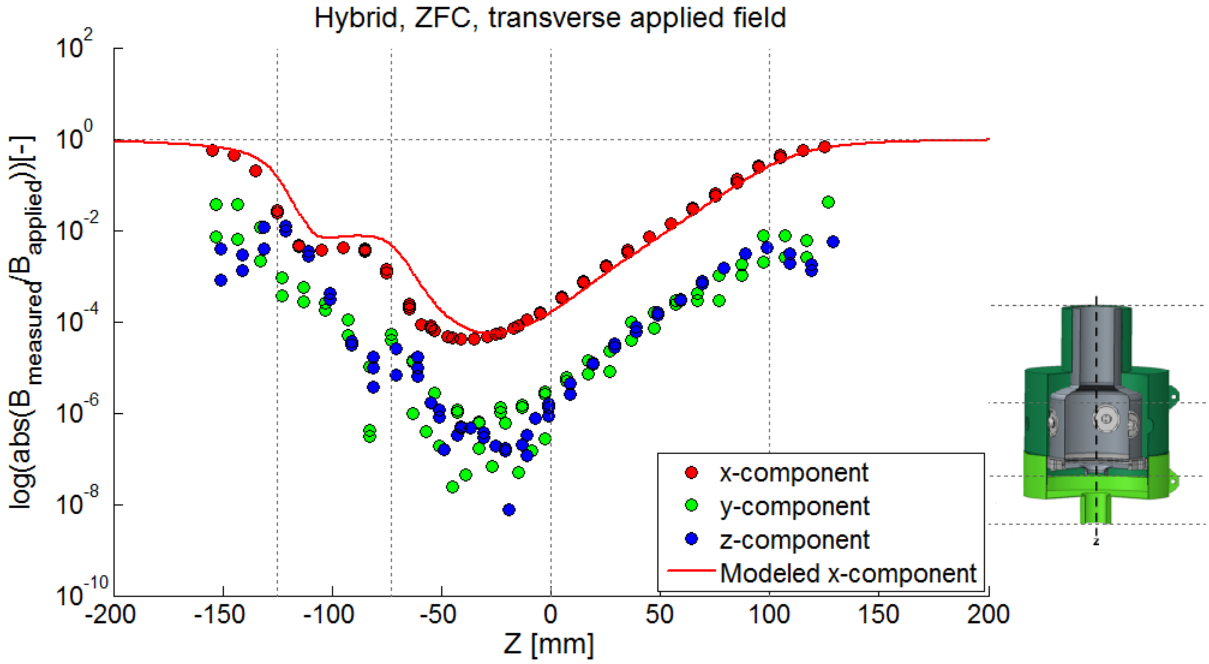

Figure 4.4: *Measured reduced field along the z-axis for the ZFC hybrid in a transverse field. The red line represents the prediction for the x-component with the static model provided by SRON.*

4.2 FC procedure

In this section the results for the FC procedure are evaluated. In a FC procedure the superconducting shield and hybrid need to pass through the vortex state of the superconductor. The absolute magnetic field is determined at T-H point 1, 2 and 3 of figure 3.5 and the reduced field is determined again for an applied field in axial and transverse direction, as explained in the previous chapter. These results and several off-axis measurements (section 4.2.4) will be evaluated, but first a measurement to determine whether flux creep occurs will be shown.

4.2.1 Flux creep

Figure 4.5 shows the absolute magnetic field measured in T-H state 3 as a function of time after the DC axial magnetic field was turned off. The magnetic field was measured at a fixed height on the z-axis of the hybrid. Already in 1962, Kim et al. showed that the amount of geometrically trapped flux (figure 1.5) in a Nb-Zr cylinder decayed logarithmically with time[33], an effect which Anderson dubbed 'flux creep' and successfully attributed to thermally activated vortex motion[34] and which was discussed in section 2.2.1. It can be quite easily determined from figure 4.5 that there is no observable creep on the time scale of our experiment, excluding thus flux creep as a dominant effect.

4.2.2 Superconducting shield

The superconducting shield was cooled in two situations: either the DC background field was applied in the axial or in the transverse direction. The results are divided in these two categories.

Cooled in axial field

For an axially applied DC field of 85 μT, the absolute magnetic field was measured along the axis of rotational symmetry. In figure 4.6 the absolute magnetic field in μT is plotted along the z-axis. Once more red, green and blue correspond to the measured x-, y- and z-components respectively. Measurements were done at three different T-H combinations during the cool-down procedure: 1) before cool-down, which is represented by the stars; 2) after cool-down but with the DC field still on, depicted by the open

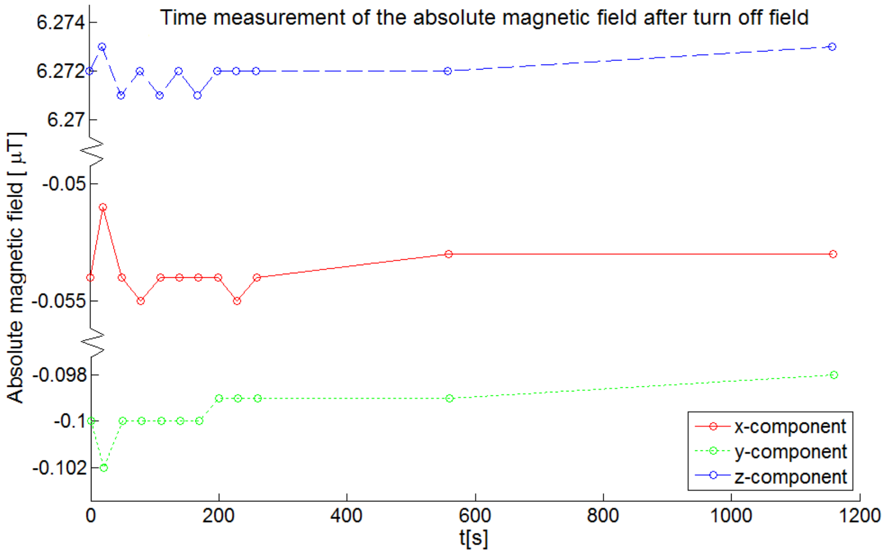

Figure 4.5: *Measurement of the absolute magnetic field in inside the hybrid shield as a function of time. The field was measured directly after the DC external axial magnetic field was turned off in the FC procedure. The measured magnetic field is roughly constant, the deviations are not significant indicating that there is no observable flux creep present.*

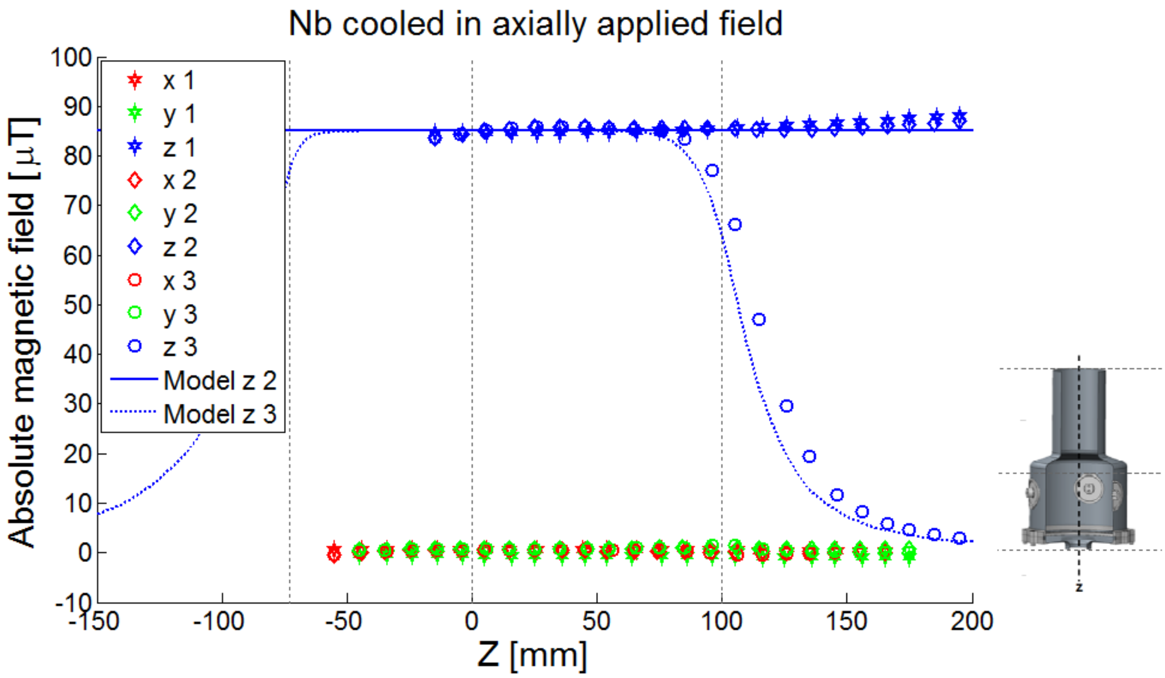

Figure 4.6: *The absolute magnetic field along the axis of rotational symmetry of the Nb shield. Red, green and blue are the measured x-, y- and z-components respectively. The stars indicate the measurements done in an axial DC field of 85 μT before cool-down, the diamonds after cool-down but with the applied field still on and the open circles after cool-down and turn-off of the field. The solid line is predicted by the dynamic model provided by SRON for the magnetic field after cool-down, the dotted line after cool-down and turn-off of the field. The dotted vertical lines indicate the positions of the bottom aperture, TES array and the top aperture.*

diamonds; and 3) after cool-down and turn-off of the magnetic field, displayed by the open circles. The figure also includes the dynamically modeled results represented by the solid line for situation 2 and the dotted line for situation 3. It is clear that there is a remarkable agreement between the measured and modeled results. Clearly, magnetic flux is frozen-in which may be due to geometric or microscopic flux trapping (or a combination of both). However, to be conclusive the results for the FC procedure with an applied field in transverse direction needs to be evaluated as the effect of geometric trapping should be less prominent in this situation.

In addition to these absolute magnetic field measurements, the reduced field along the z-axis was also determined after the shield was cooled in an axially DC applied magnetic field which was then switched off. These reduced field measurements were done in a similar fashion as the ZFC procedure: with the magnetic field applied either axially or transverse. The results are shown in figure 4.7. In blue are the measured (dots) and modeled (solid line) data for the z-component in an axially applied field, while in red the measured data and statistically modeled prediction for the x-component in a transverse field is given.

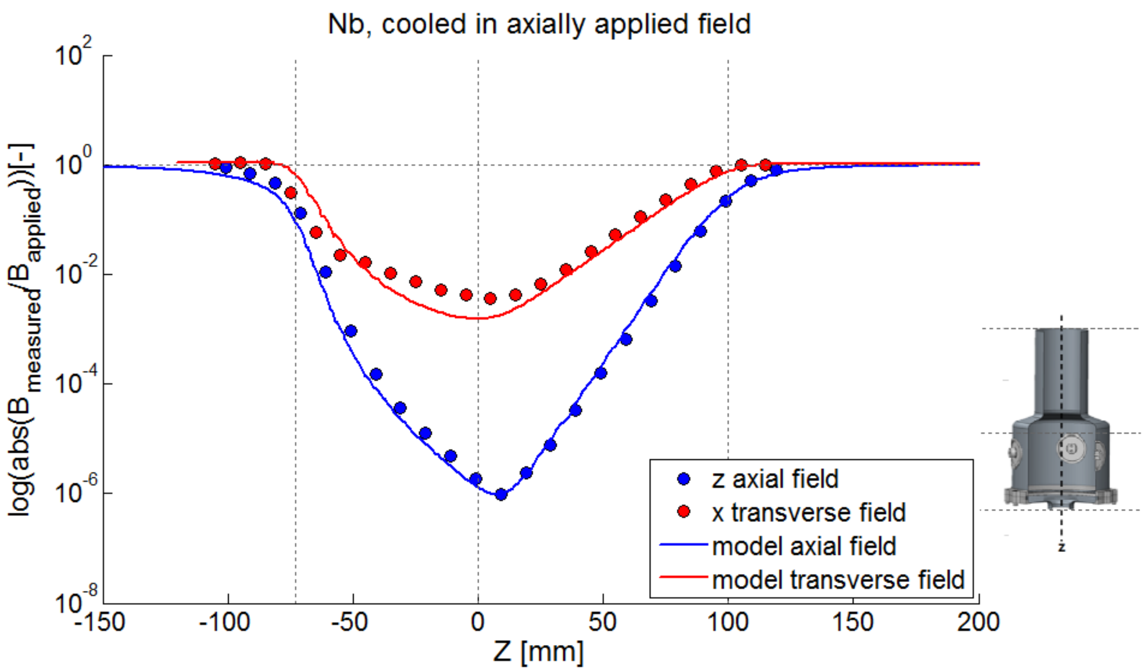

Figure 4.7: *The superconducting shield after a FC procedure in an axially applied DC magnetic field. The measured reduced field is shown for both an axially and transverse field along the axis of rotational symmetry. Only the field components that coincide with the direction of the applied field are depicted. In blue is the z-component (axially applied AC field) and in red the x-component (transverse AC applied field). Dots are the measured data, lines the predictions from SRON's static model. Also included is a schematic of the Nb shield.*

Just like figure 4.1 (ZFC), figure 4.7 shows how in case of an axially applied AC field, the data follow the model remarkably well suggesting there is little difference between the ZFC and FC behavior. This is, however, not the case for the data from the transverse field measurements. Between $z = -50$ and $z = 20$ data points deviate significantly from the model. This was not the case for the transverse attenuation in the ZFC experiment (figure 4.2), which did agree with the model prediction. Additionally, in this z-range the response of the SQUID deviated from the straightforward linear behavior with applied field (figure 3.6) but instead became significantly hysteretic (figure 4.8). This behavior is similar to a typical hysteresis loop in the Bean critical state (section 2.2.1, figure 2.6) indicating that the differences between the static model predictions and the observed reduced field can very likely be explained by movement of flux. It strongly suggests that the alternating magnetic field moves microscopic vortices that are pinned in the superconducting shield. Cool-down of the shield in a transverse field will give a further indication if this is indeed happening.

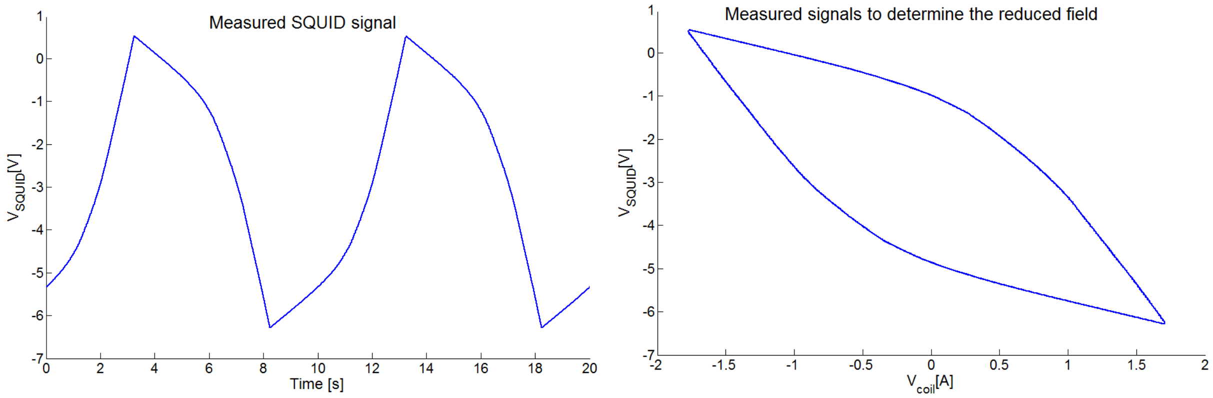

(a) *Measured response of one of the 'x'-SQUID in a transverse 'saw tooth' AC field as a function of time.*

(b) *SQUID signal plotted as a function of the applied magnetic field.*

Figure 4.8: *Hysteretic behavior in the measured SQUID signal was observed for those z-values where the reduced field deviates from the model predictions. The superconducting shield was cooled in an axially applied DC field and a triangular shaped AC field in the transverse direction was used to determine the reduced field.*

Cooled in transverse field

The superconducting shield was also cooled in a transverse applied DC field of 100 μT. The absolute magnetic field measured along the z-axis at different T-H states 1, 2 and 3 during the cool-down process is shown in figure 4.9. Red, green and blue symbols display the measured x-, y- and z-component of the magnetic field. Stars show the data before cool-down, open diamonds after cool-down and the open circles after turning-off of the external magnetic field. The solid line indicates the dynamically modeled field after cool-down and the dotted line after turn-off of the magnetic field. The measured data follow the dynamic model predictions reasonably well. The homogeneous flux density that is present in the normal state (1) remains virtually unchanged after cool-down (2). Note that at this temperature and field ($4.2K$; 100 μT) Nb should be in the Meissner state, since its first critical field is well above the applied field ($H_{c1} = 0,15\,T$[46]). Strikingly, also after switching off the external field (3) the flux density well inside the Nb enclosure remains the same. Since the external DC field was applied in the transverse direction it may be expected that geometric flux trapping only plays a minor role in this configuration, suggesting that trapped vortices treading the Nb walls are responsible for this prominent 'remanence'. Furthermore, in the dynamic model it was assumed that the superconductor behaves as an ideal conductor in this FC experiment. Since the measured and modeled data are in good agreement, it can be concluded that vortices are strongly pinned in the superconductor.

Figure 4.10 shows the measured AC reduced field along the z-axis of the superconducting shield after it was cooled in a static transverse magnetic field. Like before, to determine this reduced field a magnetic field was applied in axial or transverse direction. The data for the axial AC field direction are shown in blue, where the dots indicate the measured results and the lines the static model prediction. For an applied AC field in the transverse direction, the results are shown in red. In this last situation the measured data deviate from the model which, just like in figure 4.7, can be explained by vortex pinning in the superconducting shield, which is not accounted for in the static model. Next the hybrid shield is evaluated.

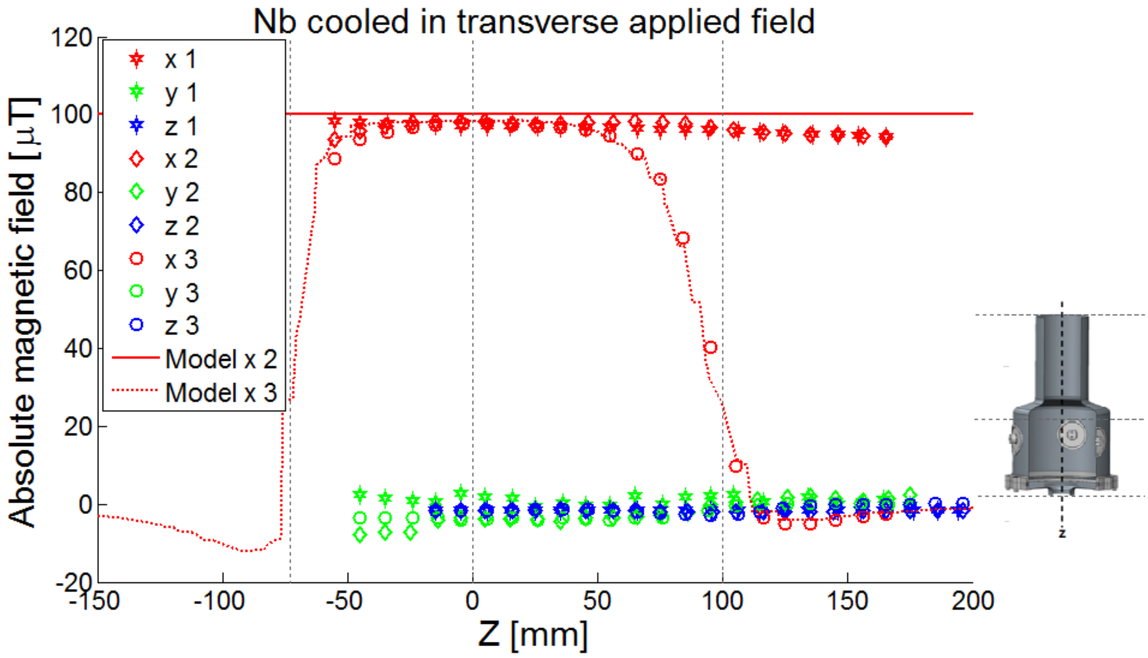

Figure 4.9: *The absolute magnetic field along the axis of rotational symmetry for the Nb shield at different stages of the cool-down in a transverse external DC magnetic field. Red, green and blue correspond to x-, y- and z-components of the magnetic field respectively. The stars indicate the measurements done before cool-down (state 1), the diamonds after cool-down (2) and the open circles after cool-down and turn-off of the magnetic field (3). The solid line is from the dynamic model prediction by SRON for the magnetic field after cool-down (2), the dotted line after turn-off of the field (3).*

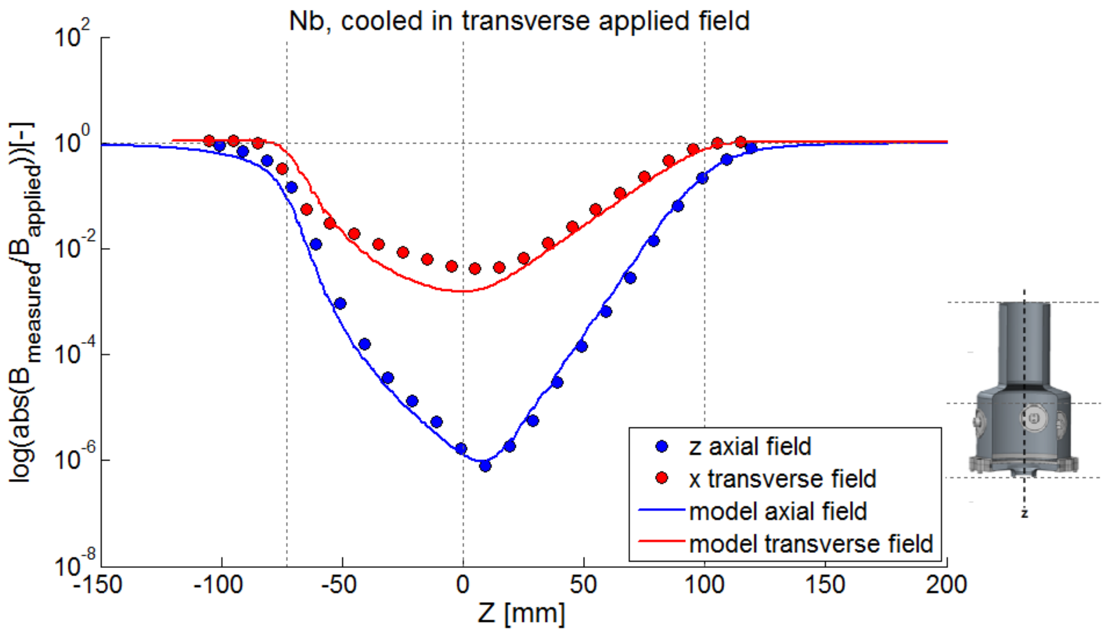

Figure 4.10: *The superconducting shield was cooled in a magnetic DC field applied in the transverse direction. In this plot, the measured reduced field for an axial and transverse AC field is shown along the axis of rotational symmetry. The components that coincide with the direction of the applied field are depicted. In blue is the z-component (axially applied field) and in red the x-component (transverse applied field). Dots are the measured results, lines the predictions from the static model provided by SRON.*

4.2.3 Hybrid system

The FC procedure was also applied to the hybrid system, the results are presented in this section. Just like with the Nb shield in section 4.2.2, magnetic field measurements were done at different stages during cool-down of the hybrid in an axial or transverse DC field, followed by AC reduced field experiments in the two field directions after the DC field was switched off.

FC in axial field

The hybrid system was cooled in an axially applied DC field of 85 μT. The absolute magnetic field was measured at three points in this cool-down process as was described in section 3.2 (figure 3.5). Figure 4.11 shows the experimental data and compares them to the dynamic model that was provided by SRON. Red, green and blue are the x-, y- and z-components respectively, the stars the measured data before cool-down (figure 3.5, 1), the diamonds after cool-down (2) and open circles after cool-down and turn-off of the magnetic field (3). The model predictions (solid and dotted lines) and measured results show good agreement. Comparison with figure 4.6 immediately shows that the general shape of the curves differs from the previous situation where just the superconducting shield was used. This is explained by the presence of the high-μ metal shield which provides a low magnetic field environment for the superconductor. However, after removal of the magnetic field there is still a significant amount of flux measured, especially near the top aperture of the hybrid (at $z = 100$). This is most likely due to geometric flux trapping.

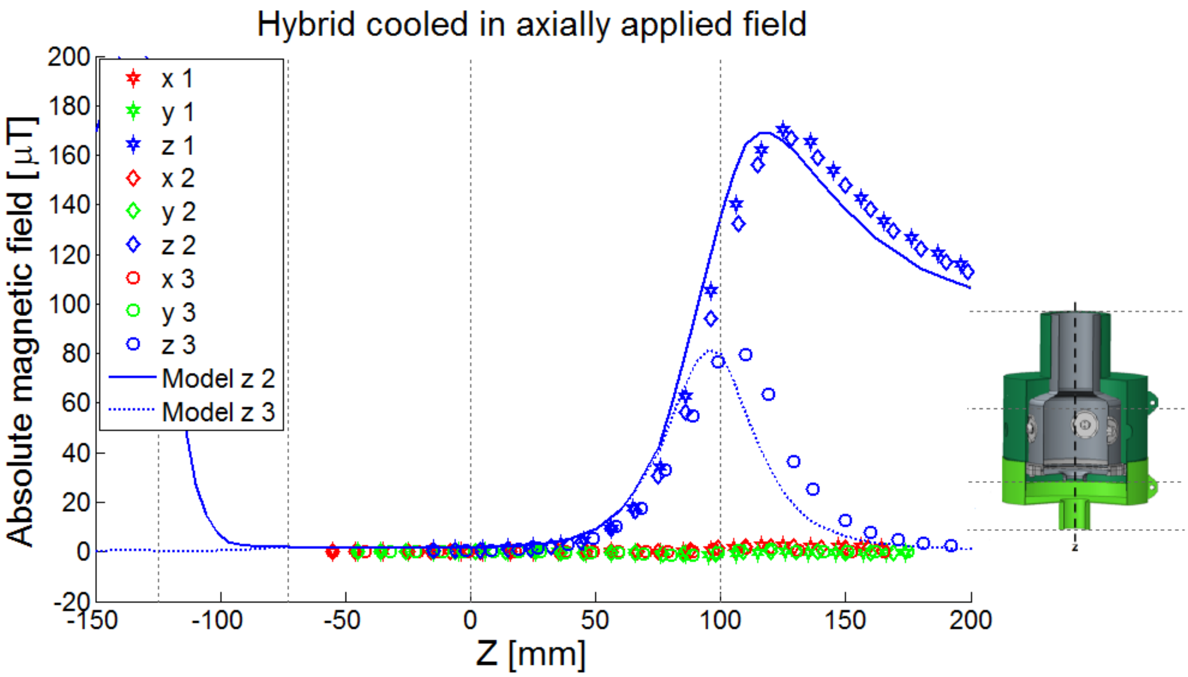

Figure 4.11: *The absolute magnetic field along the axis of rotational symmetry for the hybrid that was cooled in an axially external DC magnetic field. Red, green and blue are the measured x-, y- and z-components of the magnetic field. The stars indicate the measurements done before cool-down (1), the diamonds after cool-down (2) and the open circles after turn-off of the magnetic field (3). The solid line is from the model provided by SRON for the magnetic field after cool-down, the dotted line after turn-off of the field.*

Also in this situation reduced field measurements were performed, the results are depicted in figure 4.12. The data follow the modeled results in a similar fashion as for the ZFC measurements (figures 4.3 and 4.4). Like in the ZFC scenario, the agreement between model and observation is less good between $z = -125$ and $z = -25$. As discussed in section 4.1.2, this might be due to the imperfect behavior of the overlap region between the top and bottom Cryoperm parts. Unlike the deviations between model and data in figures 4.7 and 4.10 (FC Nb shield), however, no hysteresis was observed in the 'raw' SQUID signals for the hybrid shield. This implies that the model deviations in the present situation are not likely due to vortex motion.

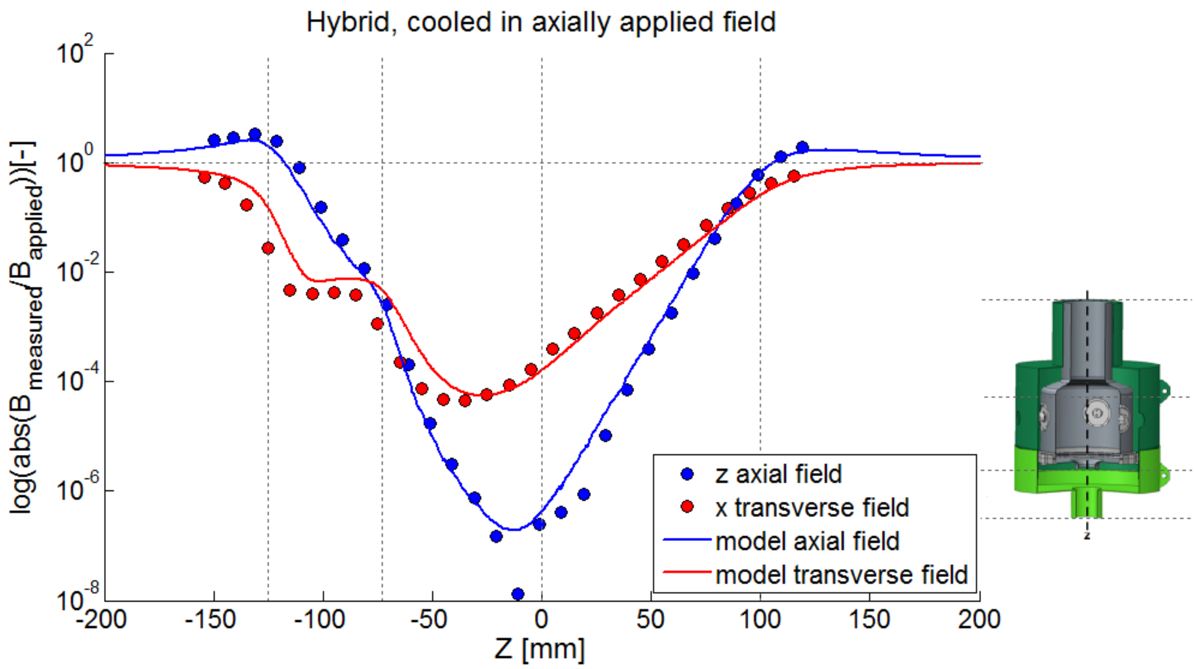

Figure 4.12: *The hybrid was cooled in a DC magnetic field applied in the axial direction. The measured reduced field for an axial and transverse AC field is shown along the axis of rotational symmetry. The components that coincide with the direction of the applied field are depicted. Blue is the z-component (axially applied field) and in red the x-component (transverse applied field). Dots are the measured data, lines the static model predictions from SRON.*

Cooled in transverse field

For the last measurement, the hybrid was cooled in a transverse DC field of 100 μT. Again both absolute magnetic field measurements and reduced field measurements were performed. Figure 4.13 shows the measured absolute magnetic field data before cool-down (1, stars), after cool-down (2, open diamonds) and after cool-down and turn-off of the magnetic field (3, open circles). Once more red, green and blue are the x-, y- and z-components. The solid line is the dynamic model prediction after cool-down and the dotted line after cool-down and turn-off of the magnetic field. Again there is good agreement between the measured and modeled results. Note how, in contrast to figure 4.11, no significant field is measured once the DC field has switched off. This confirms that the origin of flux trapping in the axially FC scenario is indeed geometrical and not microscopic. The modeled results are less smooth than in the previous cases due to a coarser mesh that was chosen in order to reduce computation time. In figure 4.14 the results for the reduced field measurements are shown. For axial AC fields there is no significant deviation from the modeled results while for a transverse AC field the results are similar as in the axial FC case. This implies that the high-μ metal shield works well to reduce the magnetic field environment for the superconducting shield. The desired shielding requirements are in this situation reached as will be concluded in chapter 5.

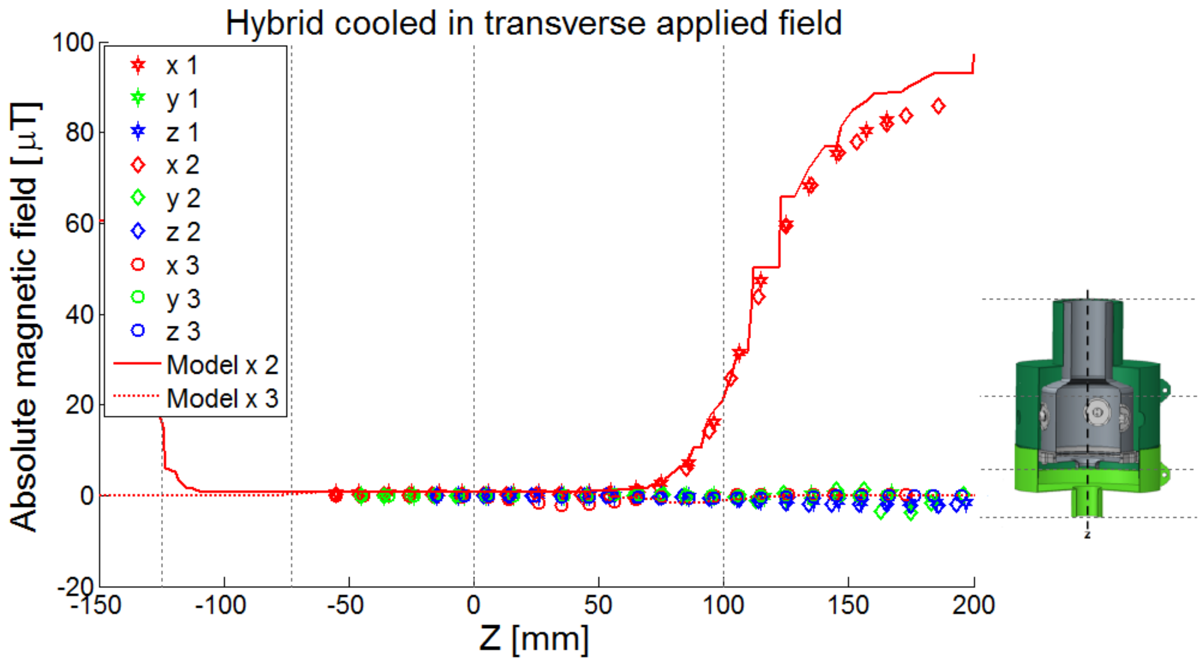

Figure 4.13: *The absolute magnetic field along the axis of rotational symmetry for the hybrid cooled in a transverse DC external magnetic field. Red, green and blue are the measured x-, y- and z-components of the magnetic field. The stars indicate the measurements done before cool-down (1), the diamonds after cool-down (2) and the open circles after cool-down and turn-off of the magnetic field (3). The solid line is from the dynamic SRON model after cool-down, the dotted line after cool-down and turn-off of the field.*

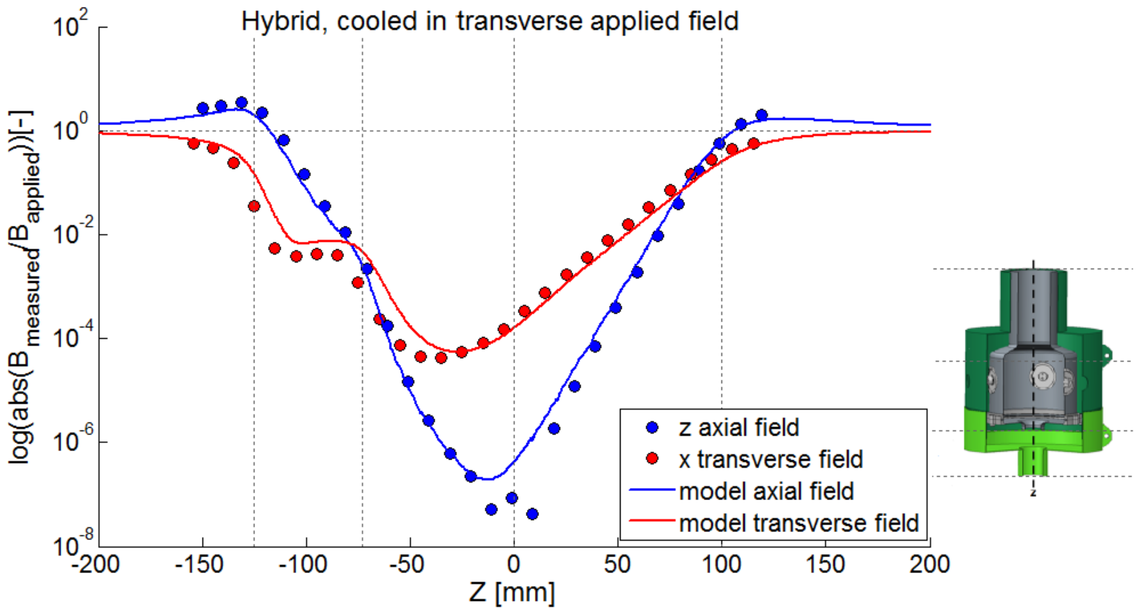

Figure 4.14: *The hybrid was FC in a transverse magnetic field. The measured reduced field for axially and transverse AC fields is shown along the axis of rotational symmetry. Only the components that coincide with the direction of the applied field are depicted. Blue is the z-component (axially applied field), red the x-component (transverse applied field). Dots are the measured results, lines the static model provided by SRON.*

4.2.4 Off-axis measurements

Until now, all presented measurements were taken on-axis, i.e. with the probes step-scanning the fields along the axis of rotational symmetry. To provide additional data for comparison with the static model, the SQUID probe was moved 13 mm off-axis (section 3.4.1, figures 3.10 and 3.11) and rotated in the plane of the TES array ($z = 0$) inside the Nb shield. The reduced field was measured in an axial AC field of 85 μT and plotted in figure 4.15. It is clear that the measurements points follow a sinusoidal shape.

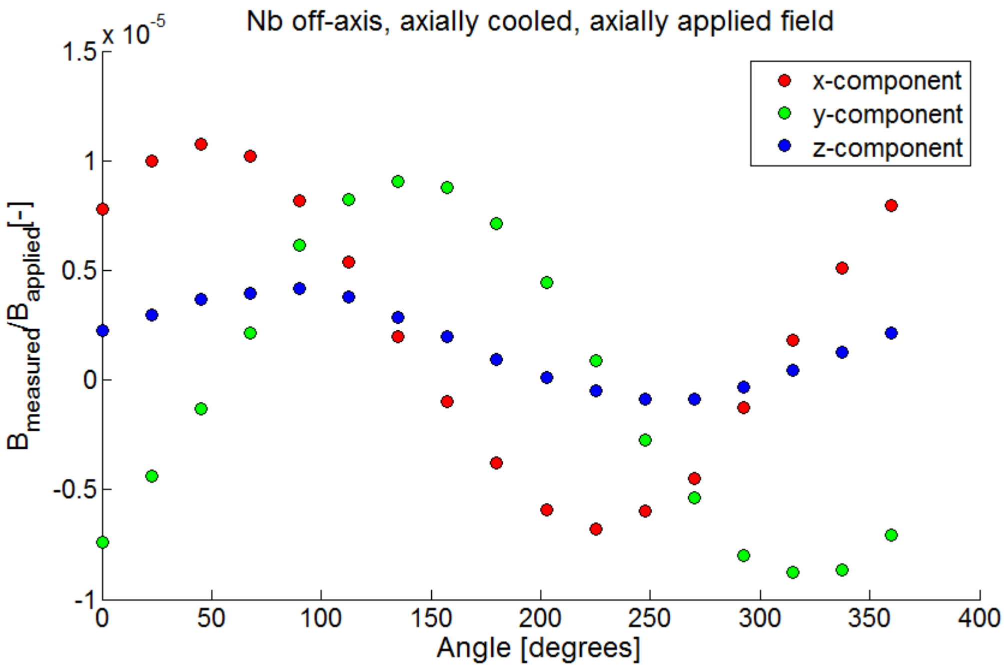

Figure 4.15: *The superconducting shield was FC in a DC magnetic field applied in the axial direction. The measured reduced field for an axially applied AC field is shown as a function of the rotation angle around the symmetry axis. The height was held constant at $z = 0$, for the z-component of the SQUID. Red, green and blue are the measured x-, y- and z-components respectively.*

The FC data for the Nb shield in the T-H situation 2 (after cooling but before switching of the field) in figures 4.6 and 4.9 indicate that large amounts of flux remain trapped in the shield, even if it should be – thermodynamically speaking – in its Meissner state. To confirm this non-trivial observation, it was decided to glue a Hall-probe on the sloped 'shoulder' of the shield (figure 3.15) and to measure the flux density also in this location with an independent technique. The results are in table 4.2. Although the calibration factor of the probe is somewhat uncertain, the measured flux densities before and after cooling are consistent with the on-axis absolute filed measurements made with the fluxgate. Note that the slope of the Nb shoulder is $\sim 20°$. Note also that the Hall-probe measurements are taken outside the Nb enclosure. The latter observation implies that the flux cannot be due to geometric flux trapping but must correspond to microscopic flux directly treading the Nb walls, thus confirming the conclusions drawn from the hysteresis in figure 4.8.

Measurement point	Axially FC $H_z = 85\ \mu T$	Transverse FC $H_x = 100\ \mu T$
$T > Tc$	74.3 μT	-33.5
$T < Tc$	84.2 μT	-25.2

Table 4.2: *Measured magnetic field with the Hall-probe in case of axially FC and transverse FC situation, before and after the Nb shield passed its superconducting transition.*

5 Discussion and Conclusion

At the end of this report we look back to the research questions formulated in the introduction of this report. An attempt is made to answer the four questions with the models and experimental data that have been shown in the previous chapters. This includes some further discussion of the various obtained results. This chapter ends with a short discussion of possible future work.

5.1 Research questions

In the introduction of this report several research questions were formulated to be answered within this study. These research questions were divided in two different sections. From a technological point of view, and essential to SRON, the main question was to determine whether the hybrid design meets the Athena shielding requirements. This design needs to reach a minimum DC reduced field of 10^{-2} and minimum AC reduced field of 10^{-5}, both for the magnetic field component normal to the detector plane. Figures 4.11 and 4.14 display the relevant results and show that **the hybrid provides the required shielding capacity** even in the realistic FC situation. This means that the hybrid design can be used in the satellite in order to shield the TES detector array.

The second more technological question was formulated as follows: 'how do the model predictions compare to the experimental results? (I.e. are the modeling tools used in the design adequate?)' This question needs to be answered twofold, depending on the cool-down procedure. In case of an ideal ZFC situation, the static model and experimental results show a remarkably good agreement, especially in view of the relative simple modeling assumptions (boundary conditions 2.6 and 2.7). This was displayed in the reduced field graphs of figure 4.1 and 4.4. **The ZFC experimental and modeled results agree well for both superconducting shield and hybrid system.** Although it can be improved to describe the high-μ metal more accurately, as momentarily it assumes that the permeability is infinitely large ($\mu \to \infty$). In the FC situation the static model breaks down for the superconducting shield. This can be seen in figures 4.7 and 4.10 where the modeled and experimental data deviate significantly when a transverse field is applied independent of the direction of the external DC field used during cool-down. It should be stressed, however, that this is true only for the superconducting shield. The models give accurate predictions for the hybrid system.

The predictions of the dynamic model, shown in figure 4.6, 4.9, 4.11 and 4.13, seem to agree well with the experimental FC data. However, some remarks are in order. In their H-formulation model SRON disregarded the typical E-J power-law relationship to describe the superconductor as it would drastically increase computation time. This turned out to be a valid assumption for the present cold-worked Nb shield and relatively fast cool-down. Nevertheless, there is a major difference between the E-J power-law and the ideal conductor picture, namely flux creep. Although our measurements of the magnetic field as a function of time showed no observable logarithmic decay (figure 4.5), the hysteretic response of the FC Nb shield during the AC reduced field measurements (figure 4.8) shows that the vortex system is, in fact, mobile and that pinning is therefore not arbitrarily strong.

Furthermore, it should be stressed that the assumption of an ideal conductor is made at point 2 of figure 5.1. The used H-formulation can describe the influence of a varying magnetic field on the superconductor e.g. from point 2 to 3, but it cannot describe the cool-down process itself (from point 1 to 2). This requires a thermodynamic approach, which can be explained with aid of figure 5.2. This shows the typical M-H and B-H diagrams of a type II superconductor in equilibrium, i.e. no vortex pinning occurs (in contrary to our experimental results). It displays the superconducting behavior at different temperatures, where the temperatures match those as shown in figure 5.1. The linear relationship between the magnetization and applied magnetic field of the curves shown in figure 5.2a correspond to the Meissner state, where the applied magnetic field is exactly compensated by the shielding currents. These figures show that by decreasing the temperature, thus moving from T_4 to T_0, at a constant value of the

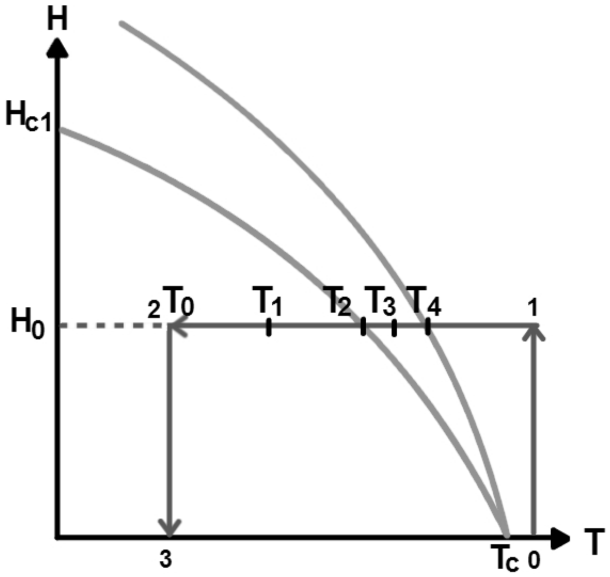

Figure 5.1: *H-T diagram of a typical type II superconductor where the arrows denote the FC situation e.g. from point 1 to 3. During cool-down the superconductor experienced a phase change. The external magnetic field is held constant at H_0 and the temperature is changed. The behavior of the superconductor at different cool-down points, from T_0 to T_4, will be discussed.*

magnetic field of H_0, vortices are pushed from the material and the Meissner state is reached at T_2. If this is indeed happening one would expect that there is no difference between a ZFC and FC situation. However, the data from the absolute magnetic field measurements on the Nb shield (figures 4.6 and 4.9) showed almost no difference between the magnetic field before and after cool-down. Furthermore, the reduced field measurements on the Nb shield (figures 4.7 and 4.10) showed a clear deviation between the model and measured data which suggests that the superconductor is not in equilibrium. Hysteresis-like behavior in the SQUID signal (figure 4.8) reinforces this conclusion. Hysteresis indicates that dissipation effects occur which is, for a superconductor, caused by the movement of vortices.

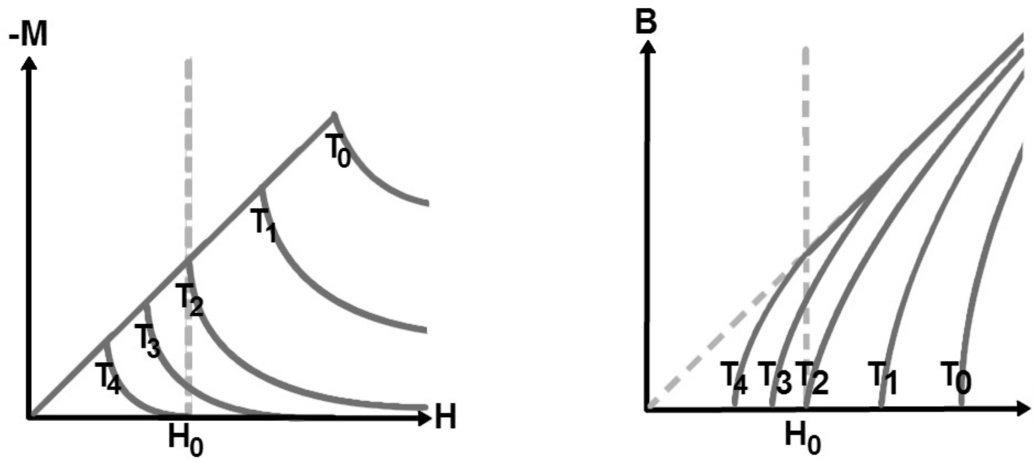

(a) *Schematic -M vs. H plot.*

(b) *Schematic B vs. H plot.*

Figure 5.2: *Schematic diagrams of a type II superconductor in equilibrium i.e. no flux pinning for different temperature values that match those of figure 5.1. If no flux pinning occurs it is expected that at H_0 and below T_2 the superconductor is in the Meissner state.*

The previous discussion indicates that vortices are trapped in the material, which is confirmed by the Hall-probe measurements outside the shield, summarized in table 4.1. **There is thus observable difference between the shielding properties of the superconductor in the ZFC and FC situation** which is caused by microscopic flux pinning. This occurs when the vortex state is passed during the FC procedure, in line with previous studies[7].

Lastly, it was asked which types of model are available to describe the superconducting properties in the FC situation. This was discussed, for the most part, in chapter 2 which focused on the various ways to model the superconductor and high-μ metal in the two cool-down scenarios and was commented upon above. The unconstrained H-model can be used to describe the effect of a varying magnetic field on a type II superconductor. However, it cannot delineate the cool-down process since this needs to be modeled thermodynamically. This is especially the case for a superconductor in non-equilibrium. **Thus the models to describe the FC procedure of a superconductor needs improvement for future work**. However, it can be determined that the behavior of a type II superconductor after cool-down (e.g. situation 2 to 3 of figure 5.1) is best to be described with the H-formulation.

5.2 Future outlook

As mentioned in the introduction of this report, the main goal of the SRON-UT collaboration was to validate the designed hybrid system. This has been done successfully. However, in wider terms, within this collaboration ideas were formulated which might, in the future, make a superconducting shield by itself sufficient. This present assignment also served to provide the baseline observations needed for such a development and hence we can formulate some recommendations. First of all, a deeper scientific understanding of the different processes happening in a superconductor during the FC procedure is advised. From a theoretical point of view, non-isothermal modeling of the vortex system, both on a micro- and macroscopic scale should replace the relative crude cool-down description in the dynamic models used in this report. Preferably, they should be tested and validated on relatively simpler geometries with better defined and controllable micro-structure. In combination with vortex image techniques, such as the scanning SQUID microscope, the vortices could be mapped and it could be shown if and when these vortices are pinned to material defects and remain pinned when the vortex state is passed. This would also further strengthen the conclusions of the present study.

Single-crystalline or controlled thin-film samples of niobium would allow for an explicit study of the superconductor in different, and more importantly, controlled cool-down situations. In this study, cool-down was uncontrolled and relatively fast (figure 3.13), which is not comparable to the in-flight situation where the shield is cooled over a much larger time. A slower cool-down might lead to better results, although the applied temperature gradient is probably more important, as was proposed in [6]. Concisely, this idea can be explained as follows. A large temperature gradient is applied to the material that turns superconducting, a normal-superconducting interface is thus induced inside. Generally, vortices are pinned to material defects. However, if this defect remains within the typical superconducting length scale of the interface, the coherence length[1], no vortex is induced. Or, in other words, the T_c distribution of the defect should be smaller than the overall temperature gradient. At the time of the writing of this Msc report, the first − albeit relative crude − controlled cool-down experiments at SRON on a simple Nb shield with different temperature gradients seem to confirm this idea, in the sense that they show that the remanence can be influenced by thermal gradients.

[1]The coherence length is the characteristic scale over which variations of the order parameter occur and can be thought of as the 'width' of a superconductor-normal interface.[5]

References

[1] Markus Bauer. Athena to study the hot and energetic universe. `http://sci.esa.int/jump.cfm?oid=54241`, June 2014.

[2] H.J. van Weers et al. TES-detector based focal plane assembly key-technology developments for ATHENA and SAFARI. *Proc. of SPIE*, 9144, 24 July 2014.

[3] V.L. Ginzburg and E.A. Andryushin. *Superconductivity.* World Scientific Publishing, 2004.

[4] D. Barret, J.W. den Herder, and L. Piro et al. The Hot and Energetic Universe: The X-ray Integral Field Unit (X-IFU) for Athena+, 2013. Supporting paper for the science theme.

[5] P. Muller, A.V. Ustinov, and V.V. Schmidt. *The Physics of Superconductors.* Springer, 1997.

[6] Tymen Goluke, Erik Krooshoop, Marc Dhallé, and Marcel ter Brake. The influence of remanence and flux trapping on the magnetic shielding properties of mu-metals and superconductors. Master's thesis, University of Twente, August 2013.

[7] K. Kuit. *Hybrid Magnetometers for Unshielded Operation.* PhD thesis, University of Twente, 2010.

[8] M.A. Taber et al. Production of ultralow magnetic fields for gravity probe B (GB-B). *Advances in Cryogenic Engineering*, 39(A), 1993.

[9] M. M. Fang, J. R. Clem, and D. K. Finnemore. Magnetic flux expulsion from superconducting shields. *IEEE Transactions on Magnetics*, MAG-23, 1987.

[10] Q. Geng, H. Minami, K. Chihara, J. Yuyama, and E. Goto. Sweeping of trapped flux in superconducting films by a micro-heat-flushing method. *Journal of Applied Physics*, 72(6), 1992.

[11] Bu xin Xu and W. O. Hamilton. Combined mu-metal and niobium superconductor shielding for dc squid operation. *Review of Scientific Instruments*, 58(2), 1986.

[12] E. Perinati, A. Santangelo, and C. Tenzer. Background studies for ATHENA: towards a new assessment phase. *Proceedings of SPIE, Space Telescopes and Instrumentation*, 9144, 2014.

[13] David J. Griffiths. *Introduction to Electrodynamics.* Pearson Education, third edition, 2008.

[14] J. R. Claycomb and J. H. Miller. Superconducting magnetic shields for SQUID applications. *Review of Scientific Instruments*, 70(12), 1999.

[15] S. Stavrev et al. Comparison of Numerical Methods for Modeling of Superconductors. *IEEE Transactions on Magnetics*, 38(2), 2002.

[16] N. Nibbio. Effect of the geometry of HTS on AC loss by using Finite Element Method simulation with B-dependent E-J power law. *IEEE Transactions on Applied Superconductivity*, 11(1), 2001.

[17] D. Ruiz-Alonso, T. Coombs, and A.M. Campbell. Computer Modelling of high-temperature superconductors using an A-V formulation. *Superconductor Science and Technology*, 17(5), 2004.

[18] N. Amemiya et al. Numerical Analysis of AC Losses in High Tc Superconductors Based on E-j Characteristics Represented with n-Value. *IEEE Transactions on Applied Superconductivity*, 7(2), 1997.

[19] B. V. Vasil'ev, V. K. Ignatovich, and E. V. kolycheva. Shielding of weak magnetic fields by superconducting shells. *Soviet Physics - Technical Physics*, 23(9), 1978.

[20] N. Amemiya et al. Numerical modelings of superconducting wires for AC loss calculations. *Physics C*, 1998.

[21] A Stenvall and T Tarhasaari. Programming finite element method based hysteresis loss computation software using non-linear superconductor resistivity and t formulation. *Superconductor Science and Technology*, 23(10), 2010.

[22] V. Lahtinen, M. Lyly, A. Stenvall, and T. Tarhasaari. Comparison of three eddy current formulations for superconductor hysteresis loss modelling. *Superconductor Science and Technology*, 25(11), 2012.

[23] A. Badia and H. C. Freyhardt. Meissner state properties of a superconducting disk in a non-uniform magnetic field. *Journal of Applied Physics*, 83(5), 1997.

[24] Roberto Brambilla, Francesco Grilli, and Luciano Martini. Development of an edge-element model for AC loss computation of high-temperature superconductors. *Superconductor Science and Technology*, 20(1), 2006.

[25] R. Pecher t al. 3D-modelling of bulk type-II superconductors using unconstrained H-formulation.

[26] M. A. J. Paavola et al. High Performance Magnetically Shielded Room for Clinical Measurements. *Biomag 96: Proceedings of the Tenth International Conference on Biomagnetism*, 1/2, 2000.

[27] Clayton R. Paul. *Introduction to Electromagnetic Compatibility.* John Wiley and Sons, second edition, 2006.

[28] Jan Awrejcewicz. *Numerical Analysis - Theory and Application.* InTech, 2011.

[29] J. N. Reddy. *An Introduction to the Finite Element Method.* McGraw-Hill Book Company, 1984.

[30] C. P. Bean. Magnetization of hard superconductors. *Physical Review Letters*, 8(6), 1962.

[31] C. P. Bean. Magnetization of high-field superconductors. *Review of Modern Physics*, 36(1), 1964.

[32] C. Navau, N. Del-Valle, and A. Sanchez. Macroscopic Modeling of Magnetization and Levitation of Hard Type-II Superconductors: The Critical-State Model. *IEEE Transactions on Applied Superconductivity*, 23(1), 2013.

[33] Y. B. Kim, C. F. Hempstead, and A. R. Strnad. Critical Persistent Currents in Hard Superconductors. *Physical Review Letters*, 9(7), 1962.

[34] P. W. Anderson. Theory of flux creep in hard superconductors. *Physical Review Letters*, 9(7), 1962.

[35] Andrzej Krawczyk and John A. Tegopoulos. *Numerical Modelling of Eddy Currents.* Oxford University Press, 1993.

[36] Gerrit Mur. Edge Elements, their Advantages and their Disadvantages. *IEEE Transactions on Magnetics*, 30(5), 1994.

[37] Cu-Xing Chen, James A. Brug, and Ronald B. Goldfarb. Demagnetization Factors for Cylinders. *IEEE Transactions on Magnetics*, 27(4), 1991.

[38] W. DeSorbo. Effect of dissolved gases on some superconducting properties of niobium. *Physical Review*, 132(1), 1963.

[39] J. T. Black and R. A. Kohser. *DeGarmo's Materials and Processes in Manufacturing.* John Wiley and Sons, eleventh edition, 2012.

[40] `www.cryopermshielding.com`. Visited on 7-11-2014.

[41] M. Masuzawa, A. Terashima, and K. Tsuchiya. Magnetic Properties of Shielding Materials for Superconducting Cavities. *IEEE Transactions on Applied Superconductivity*, 22(3), 2012.

[42] 3D Green. `http://www.supracon.com/en/3d_green.html`, Visited on 01-2015.

[43] P. Ripka. Advanced in fluxgate sensors. *Sensors and Actuators A-physical*, 106(1-3), 2003.

[44] Mag-01 and Mag-01H single axis fluxgate magnetometers. `http://www.bartington.com/`, 2014.

[45] Edward Ramsden. *Hall-effect Sensors: Theory and Application*. Newnes, 2006.

[46] J. A. Thompson. Characterization of Niobium Films and a Bulk Niobium Sample with RRR, SIMS and a SQUID Magnetometer. *Journal of Undergraduate Research*, 3(1), 2004.

A Solving the Laplace equation

As was shown in chapter 2, the static magnetic field in the presence of a superconducting shield in the Meissner state or a high-μ metal can be determined by solving the Laplace equation for the magnetic potential with the appropriate boundary conditions:

$$\nabla^2 \psi = 0 \tag{A.1}$$

$$\mathbf{H}_{\perp,sc} = 0 \tag{A.2}$$

$$\mathbf{H}_{\parallel,\mu} = 0 \tag{A.3}$$

The subscripts sc and μ indicate the superconducting material and high μ-metal respectively. This equation can be solved in a numerous of ways, most commonly used is separation of variables which is illustrated below.

E.g. Claycomb et al.[14] use the method of separation of variables to solve the Laplace equation for a superconducting tube. This geometry is best described in cylindrical coordinates, so that the Laplace equation is rewritten as:

$$\frac{1}{s}\frac{\partial}{\partial s}\left(s\frac{\partial \psi}{\partial s}\right) + \frac{1}{s^2}\frac{\partial^2 \psi}{\partial \phi^2} + \frac{\partial^2 \psi}{\partial z^2} = 0 \tag{A.4}$$

Separation of variables means that a trial solution is used of the form:

$$\psi = S(s)\Phi(\phi)Z(z) \tag{A.5}$$

Substituting this in equation A.4, dividing by $S(s)\Phi(\phi)Z(z)$ and rearranging gives:

$$\frac{1}{sS(s)}\frac{\partial S(s)}{\partial s} + \frac{1}{S(s)}\frac{\partial^2 S(s)}{\partial s^2} + \frac{1}{s^2\Phi(\phi)}\frac{\partial^2 \Phi(\phi)}{\partial \phi^2} = -\frac{1}{Z(z)}\frac{\partial^2 Z(z)}{\partial z^2} \tag{A.6}$$

In this last equation it the left-hand side depends on both s and ϕ, while the right-hand side depends only on z. This can only be true for all positions (s, ϕ, z) simultaneously when the two are equal to the same constant. If this separation constant is $-l^2$, the right-hand side can be rewritten as:

$$-\frac{1}{Z(z)}\frac{\partial^2 Z(z)}{\partial z^2} = -l^2 \tag{A.7}$$

This has as general solution:

$$Z(z) = a_1 e^{lz} + a_2 e^{-lz} \tag{A.8}$$

For the field to remain finite when z tends to infinity, only the negative exponent is retained (i.e. $a_1 = 0$). Next the left-hand side of equation A.6 is rewritten as:

$$\frac{s}{S(s)}\frac{\partial S(s)}{\partial s} + \frac{s^2}{S(s)}\frac{\partial^2 S(s)}{\partial s^2} + l^2 s^2 = -\frac{1}{\Phi(\phi)}\frac{\partial^2 \Phi(\phi)}{\partial \phi^2} \tag{A.9}$$

Again this can only be true if both sides are equal to a new separation constant, m^2, yielding:

$$-\frac{1}{\Phi(\phi)}\frac{\partial^2 \Phi(\phi)}{\partial \phi^2} = m^2 \tag{A.10}$$

This time the general solution is:

$$\Phi(\phi) = b_1 \sin(m\phi) + b_2 \cos(m\phi) \tag{A.11}$$

Note that single-valuedness of ψ requires that m takes on integer values only. Finally the left-hand side of A.9 needs to be evaluated. This equation can be rewritten to:

$$s\frac{\partial S(s)}{\partial s} + s^2\frac{\partial^2 S(s)}{\partial s^2} + (l^2 s^2 - m^2)S = 0 \tag{A.12}$$

This is Bessel's differential equation with solutions (taking only the Bessel functions of the first kind into account, the second kind diverges when $s \to 0$):

$$S(s) = cJ_m(ls) \tag{A.13}$$

This gives the following general solution for the magneto-static potential:

$$\psi = J_m(ls)(b_1 \sin(m\phi) + b_2 \cos(m\phi))e^{-lz}) \tag{A.14}$$

The corresponding magnetic field can be determined using 2.1:

$$\begin{pmatrix} H_s \\ H_\phi \\ H_z \end{pmatrix} = - \begin{pmatrix} \frac{\partial \psi}{\partial s} \\ \frac{1}{s}\frac{\partial \psi}{\partial \phi} \\ \frac{\partial \psi}{\partial z} \end{pmatrix} \tag{A.15}$$

To make this more specific, let's consider the case of a superconducting tube in an axial field. Applying boundary condition 2.7 on the inside tube wall leads to $H_s = 0$ or, in terms of ψ:

$$\frac{\partial}{\partial(ls)} J_m(ls) = 0 \text{ at } s = a \tag{A.16}$$

Here a is the radius of the superconducting tube. The boundary condition implies that only an infinite but discrete set of values is allowed for l (i.e. those values for which $J_m(la)$ corresponds to a minimum or maximum in the $J_m(ls)$ curve). We denote these values l_{mn} and the general solution for the superconductor thus becomes:

$$\psi = \sum_{m=0}^{\infty} \sum_{n=1}^{\infty} J_m(l_{mn}s)(b_{mn1} \sin(m\phi) + b_{mn2} \cos(m\phi))e^{-lmnz} \tag{A.17}$$

If, moreover, we know that the field is applied in the axial direction, symmetry indicates that there is no ϕ dependence and A.11 shows that only the $m = 0$ term remains:

$$\psi = \sum_{n=1}^{\infty} c_n J_0(l_n s)e^{-lnz} \tag{A.18}$$

For the slowest mode of decay, $n = 1$, the root of the derivative of the Bessel function $J - 0$ is found to be $l_1 = 3,83$. This means that the magnetic field will be proportional to:

$$H_{axial,sc} \propto exp\left(-3,83\frac{z}{a}\right) \tag{A.19}$$

For the high-μ metal in an axial field the boundary condition is different. In this situation the tangential component of the magnetic field on the tube wall needs to be zero, $H_z = 0$ at $s = a$. The smallest root of the Bessel function is now equal to $l_1 = 2,41$, so that:

$$H_{axial,fer} \propto exp\left(-2,41\frac{z}{a}\right) \tag{A.20}$$

In case of a field applied in transverse direction the solutions change since only the odd order Bessel functions contribute to a nonzero radial magnetic field. This means that $m = 1$ and the following expressions are found:

$$H_{trans,sc} \propto exp\left(-1,84\frac{z}{a}\right) \tag{A.21}$$

$$H_{trans,fer} \propto exp\left(-3,83\frac{z}{a}\right) \tag{A.22}$$

Note that z is the 'depth' in the tube, i.e. the distance from the tube's end. Comparing equations A.19 and A.20 shows that with a superconductor, the field lines 'dip' deeper into the aperture than with a high-μ metal.

B Coil configuration

Validation of the hybrid had to be done in a controlled magnetic field environment which was achieved by placing the hybrid, inserted in a cryostat, in a magnetically shielded room. Two coil sets are placed inside this room to apply fields either in horizontal or vertical direction. A circular coil set, placed in the xy-plane, applies a field in the vertical direction and will be referred to as the z-coils. A square coil set, in the yz-plane, provides a field in the horizontal direction and will be referred to as the x-coils. Usually the homogeneous region of a coil set is at its geometric center, however, the μ-metal walls, ceiling and floor, of the magnetically shielded room influence the field profile of the coils. The x-coils are placed symmetrically in the room with respect to its magnetic field direction, so the effect will cancel[1]. For the z-coils this is not possible. Space above these coils is needed to be able to move probes up and down. Therefore a different solution was used. To explain this properly, first the influence of the shielded room on the field profile will be determined.

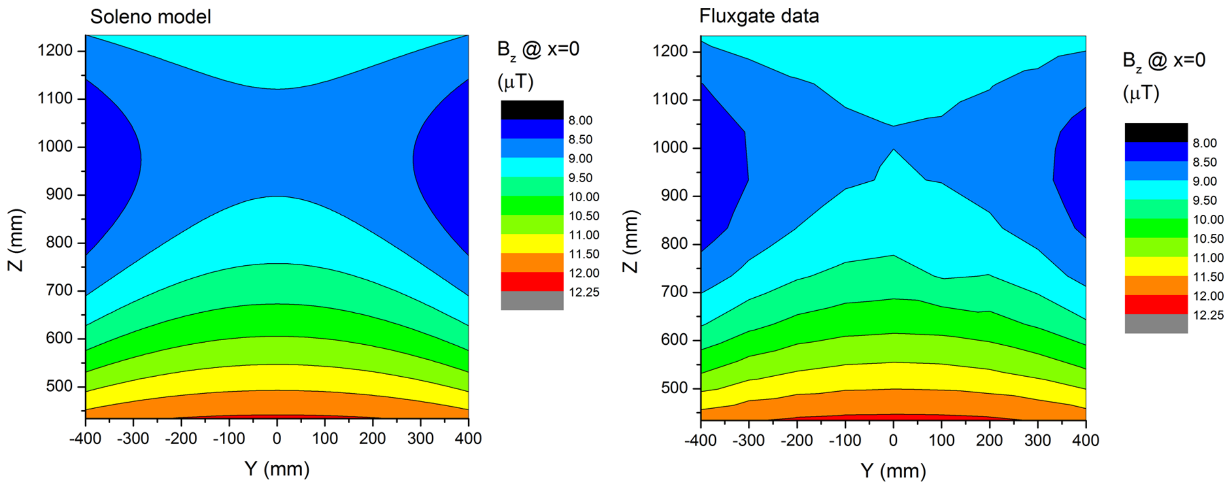

(a) *Modeled field profile for the same region.* (b) *Measured field profile for the same region.*

Figure B.1: *The magnetic field profile of the circular z-coil set that was measured and modeled. The magnetically shielded room is taken into account and it is clear that the floor has an effect on the field profile: the homogeneous region around the minimum in B_z is not at 851 mm from the floor where it might be expected just taking into account the coils but is lifted to 1005 mm from the floor due to the relatively nearby floor.*

The influence of the magnetically shielded room can be modeled by using the 'method of images'[13]. The floor and roof of the shielded room is used as a symmetry plane or mirror plane. By adding mirrored virtual current loops the influence of the shielded room can be determined. The main idea behind the mirror image method is the fact that the boundary conditions at the μ-metal surfaces are approximately $H_{\|}$ (equation 2.6), i.e. field lines must fall perpendicular onto the surface. Placing coils identical to the real ones at an identical distance behind (or above, below, etc.) the surface automatically satisfies this condition. Inside the room, these virtual mirror coils produce the same field as the actual magnetization currents in the μ-metal. This modeling was done with the Excel macro 'Soleno' developed in EMS to evaluate the Biot-Savart law for any co-axial coil system with elliptical integrals at any arbitrary point. Virtual third order reflections were needed to get agreement between this model and the measured field within 1%. With this model it was then possible to try new configurations. For a perfect coil configuration, the homogeneous field regions of the x- and z-coils overlap and enough space above the z-coils is

[1] At least qualitatively

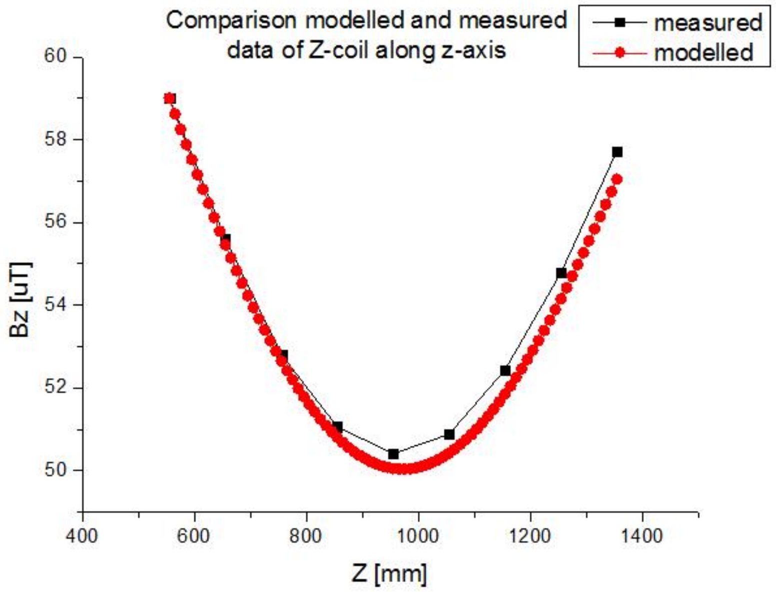

Figure B.2: *Measured (black) and modeled (red) magnetic field along the z-axis of the z-coils with a current ratio of* $I_{top} = 1,305 \cdot I_{bottom}$.

left for the measuring probes.

Figure B.1 shows the field profile of the original configuration of the z-coils (measured and modeled). It is quite clear that the most homogeneous field is found significantly above its geometric center: the shielded room adds to the field of the bottom coil which raises the field profile. One way to compensate this effect is to apply a higher current to the upper coil and balance the field of the coil and shielded room. With the described model it was possible to determine the optimum current ratio to be:

$$\frac{I_{top}}{I_{bottom}} = 1,305 \tag{B.1}$$

As seen in figure B.2 the most homogeneous field is now found at the geometric center of the x-coils and there is a good agreement between the model and measured data. Figure B.3 shows this optimal configuration schematically.

Figures B.4 to B.7 provide additional detail on the coils, while figures B.8 to B.13 compares the measured and modeled data on different planes. These measurements were done with a fluxgate.

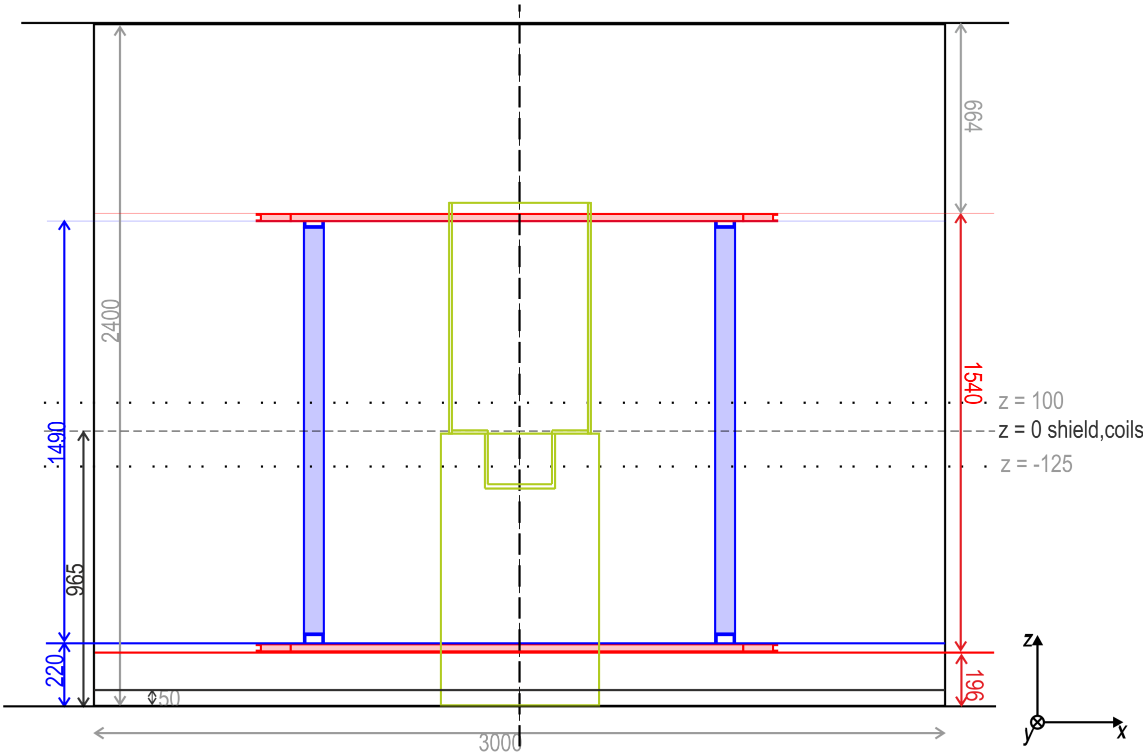

Figure B.3: *Schematics of the magnetically shielded room and the two coil set in optimum position. Values are in mm.*

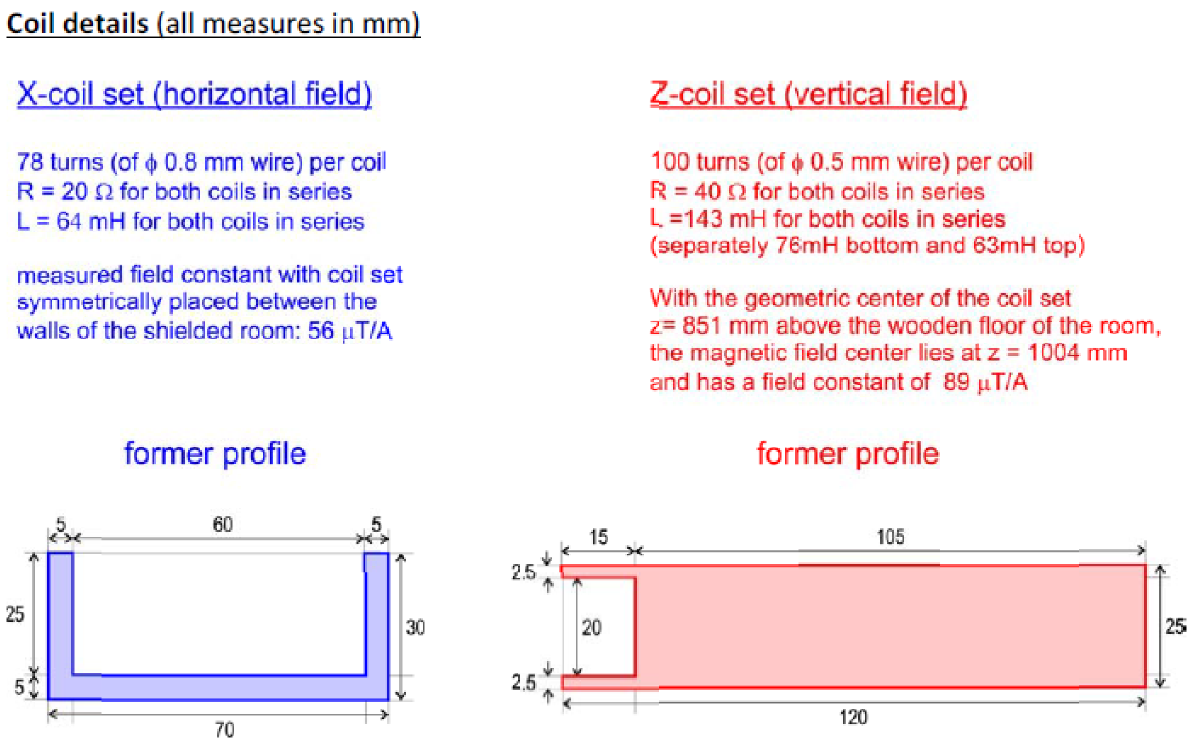

Figure B.4: *Coil details of the x-coil set (horizontal field) and z-coil set (vertical field) including the former profiles.*

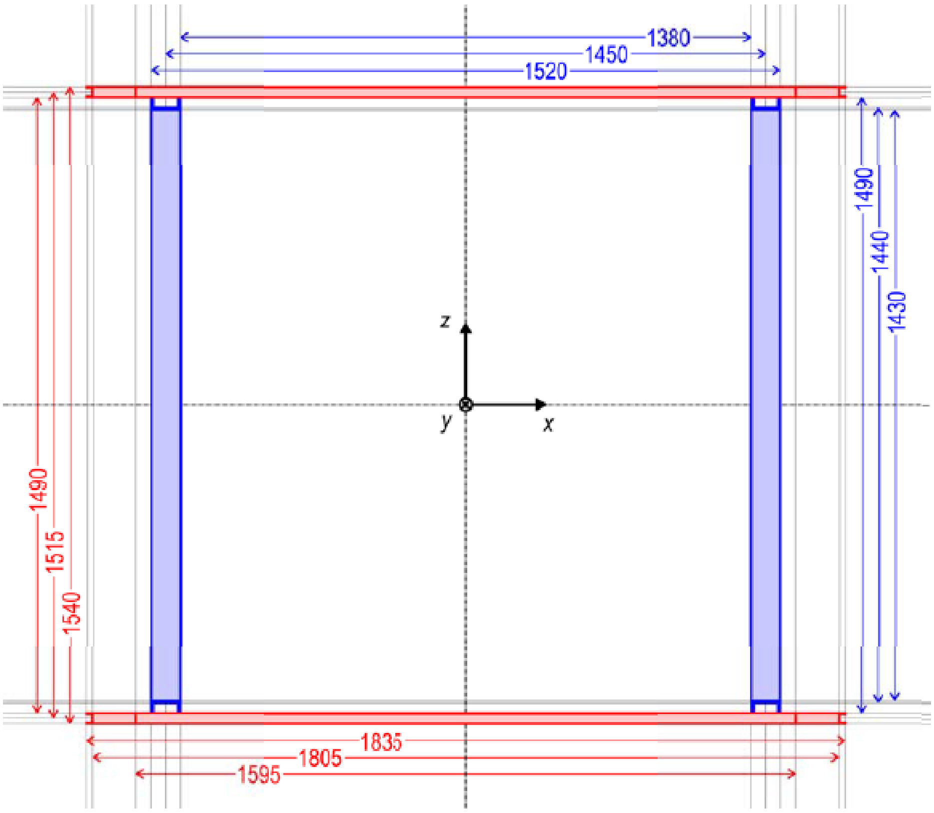

Figure B.5: *Schematics of the two coils in the zx-plane.*

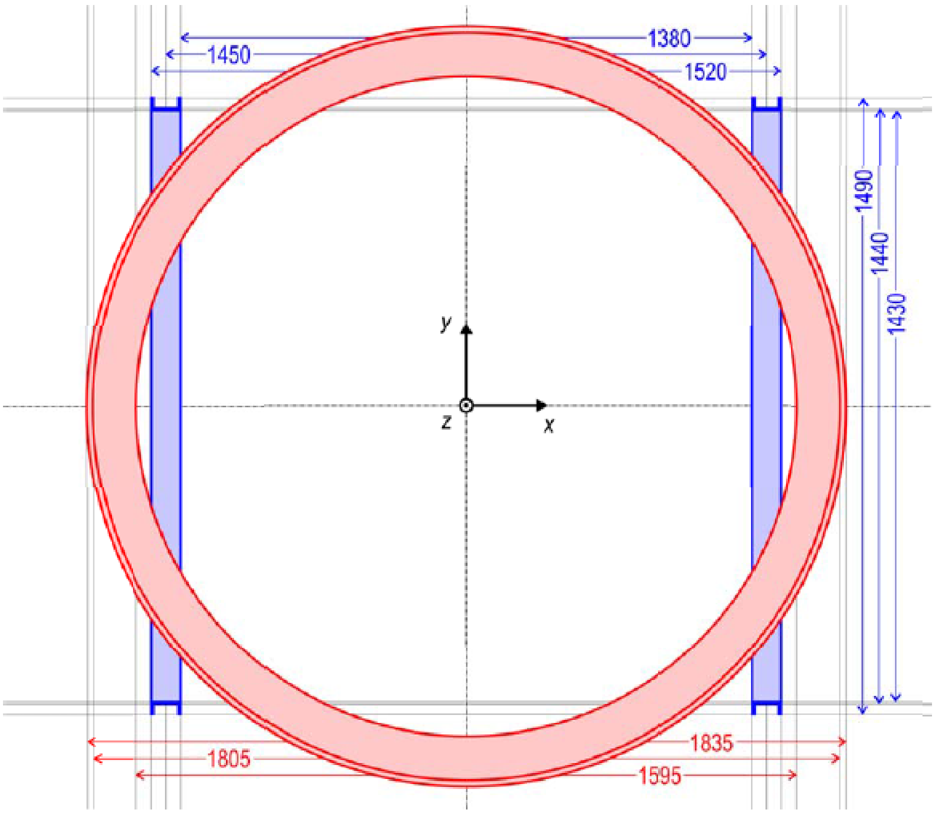

Figure B.6: *Schematics of the two coils in the yx-plane.*

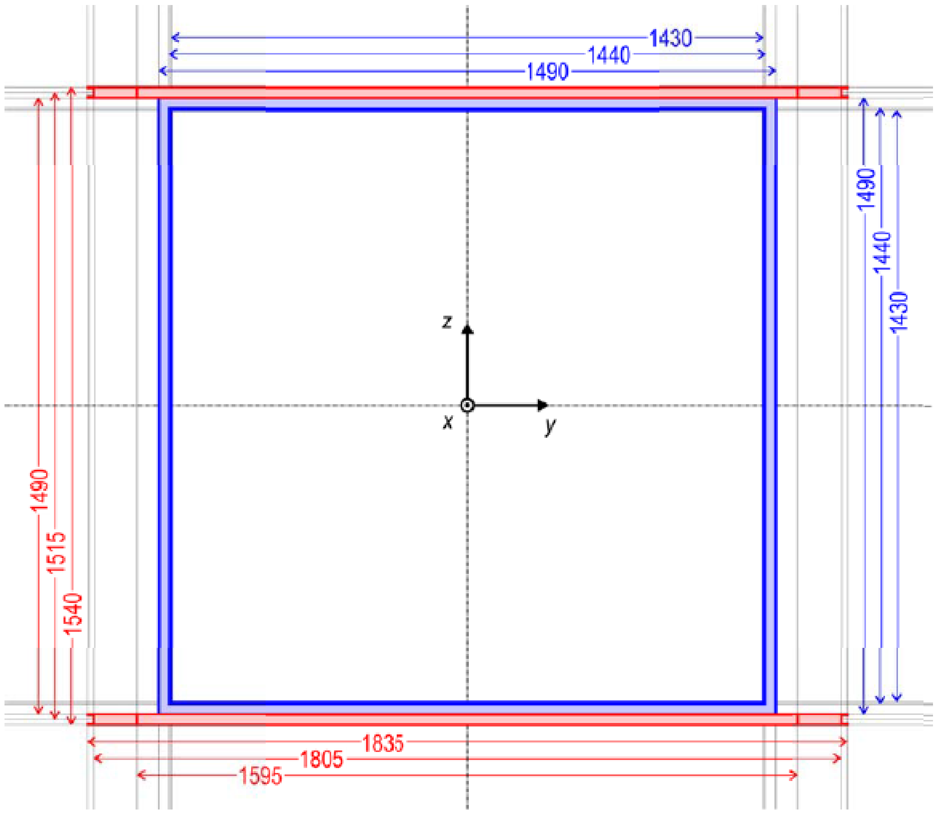

Figure B.7: *Schematics of the two coils in the zy-plane.*

X-coil field: x-component at *x* = 0 (0.1A coil current)

Standard deviation data/model 70nT

Modeled coil constant in center 56.1 μT/A

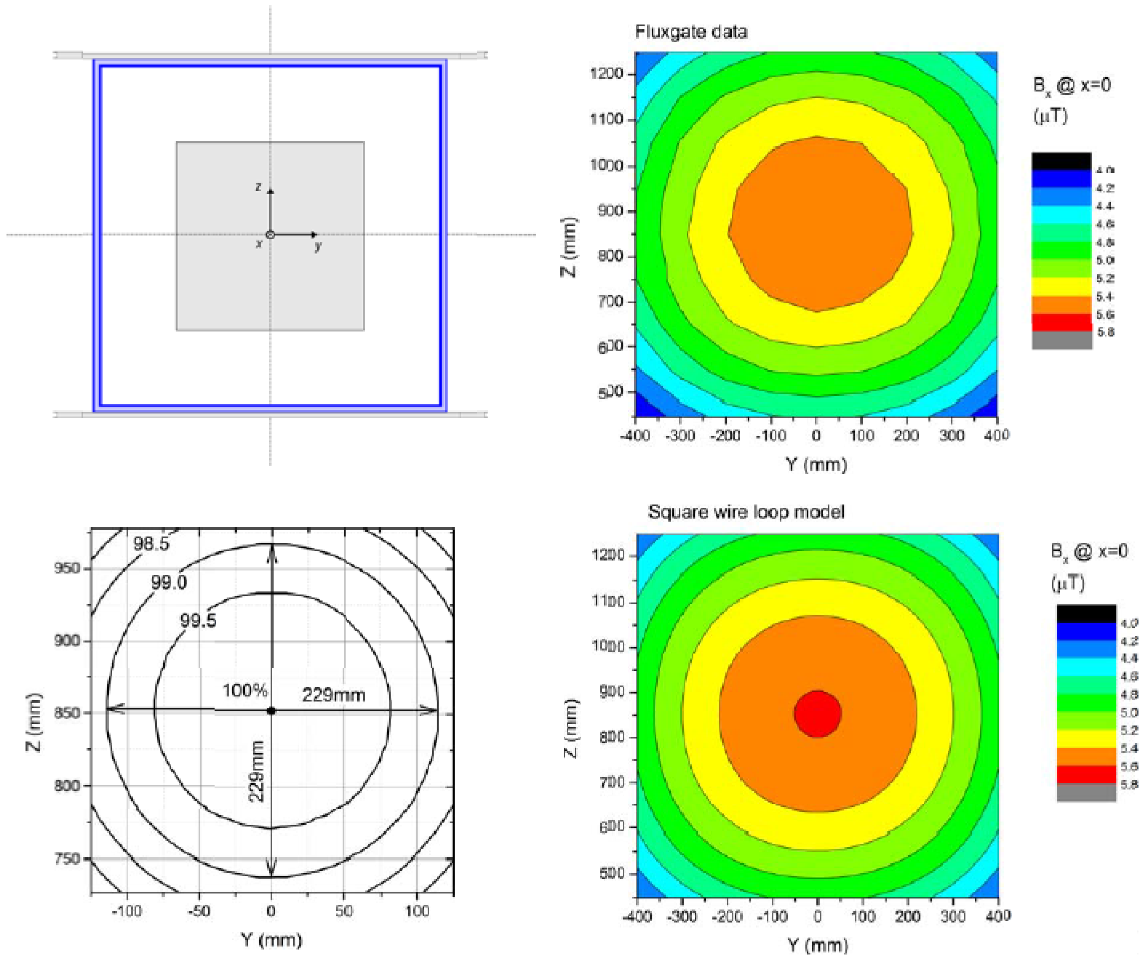

Figure B.8: *Measured and modeled data of the x-coil field in the zy-plane, at $x = 0\,mm$.*

X-coil field: x-component at y = 0 (0.1A coil current)

Standard deviation data/model 57nT

Modeled coil constant in center 56.1 μT/A

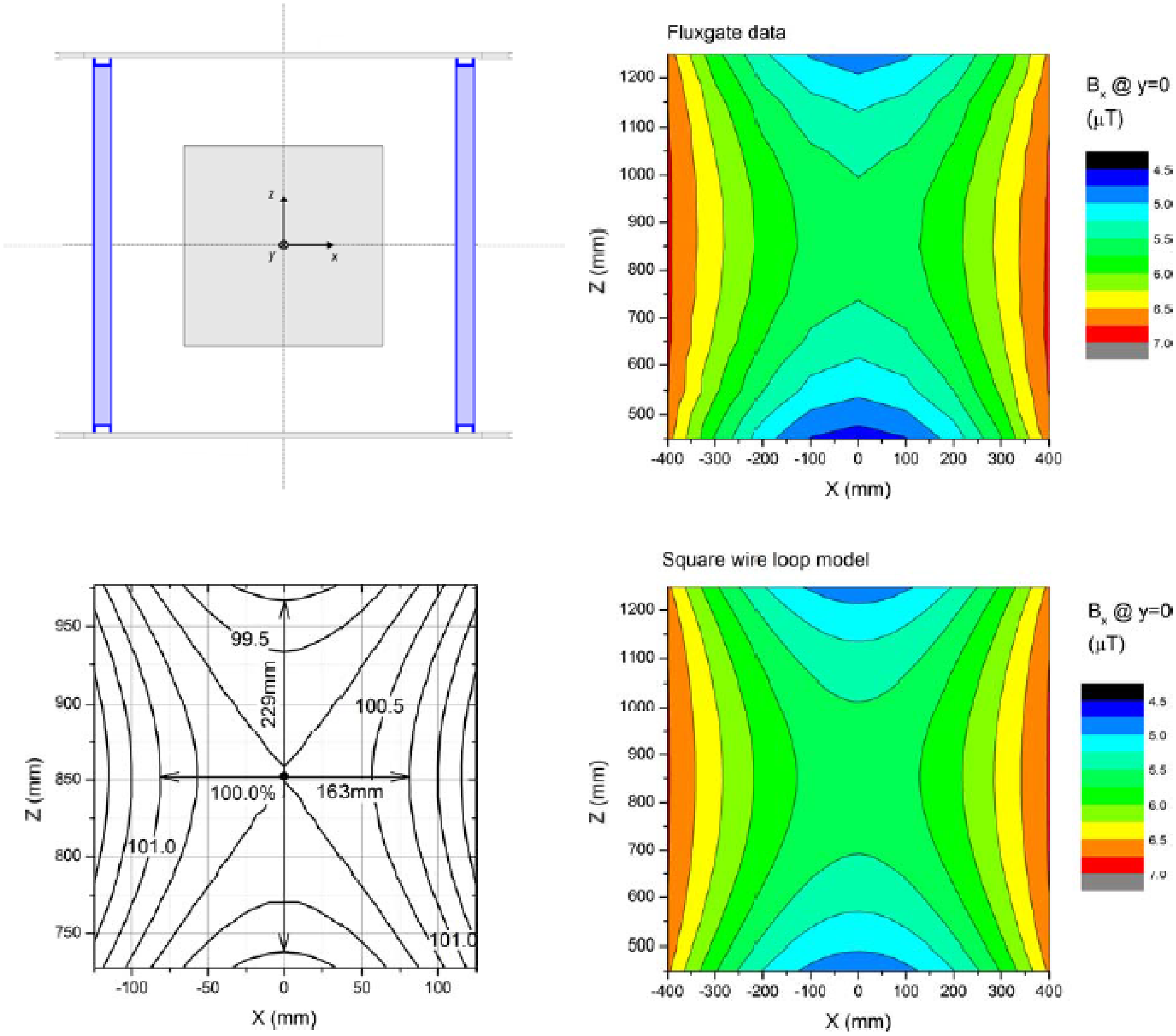

Figure B.9: *Measured and modeled data of the x-coil field in the zx-plane, at* $y = 0\,mm$*.*

X-coil field: x-component at *z* = 999 (0.1A coil current)

Standard deviation data/model 21nT

Modeled coil constant in center 56.1 μT/A

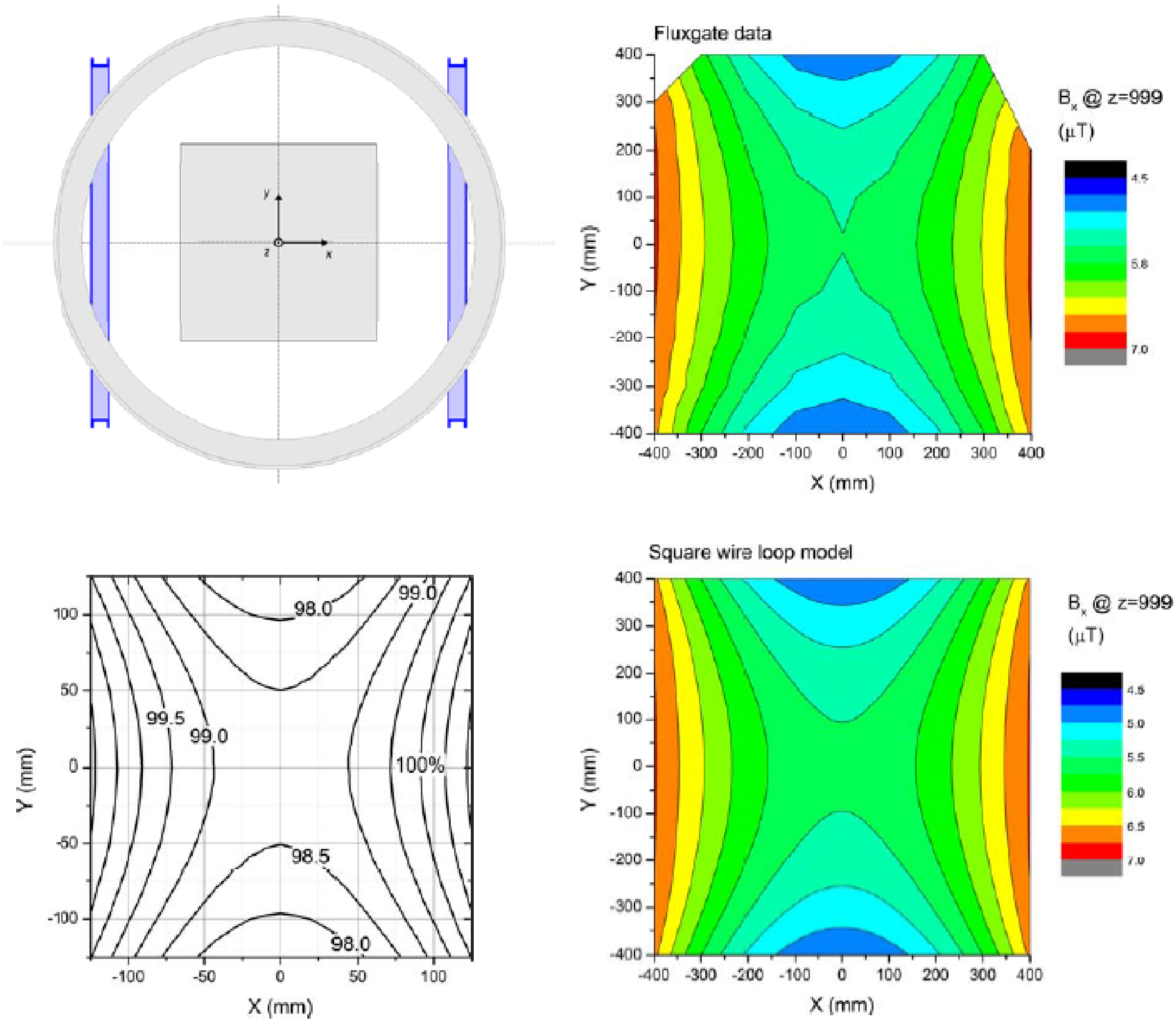

Figure B.10: *Measured and modeled data of the x-coil field in the yx-plane, at* $z = 999\,mm$.

Z-coil field: z-component at *x* = 0 (0.1A coil current)

Standard deviation data/model 87nT

Modeled coil constant in center 88.9 μT/A

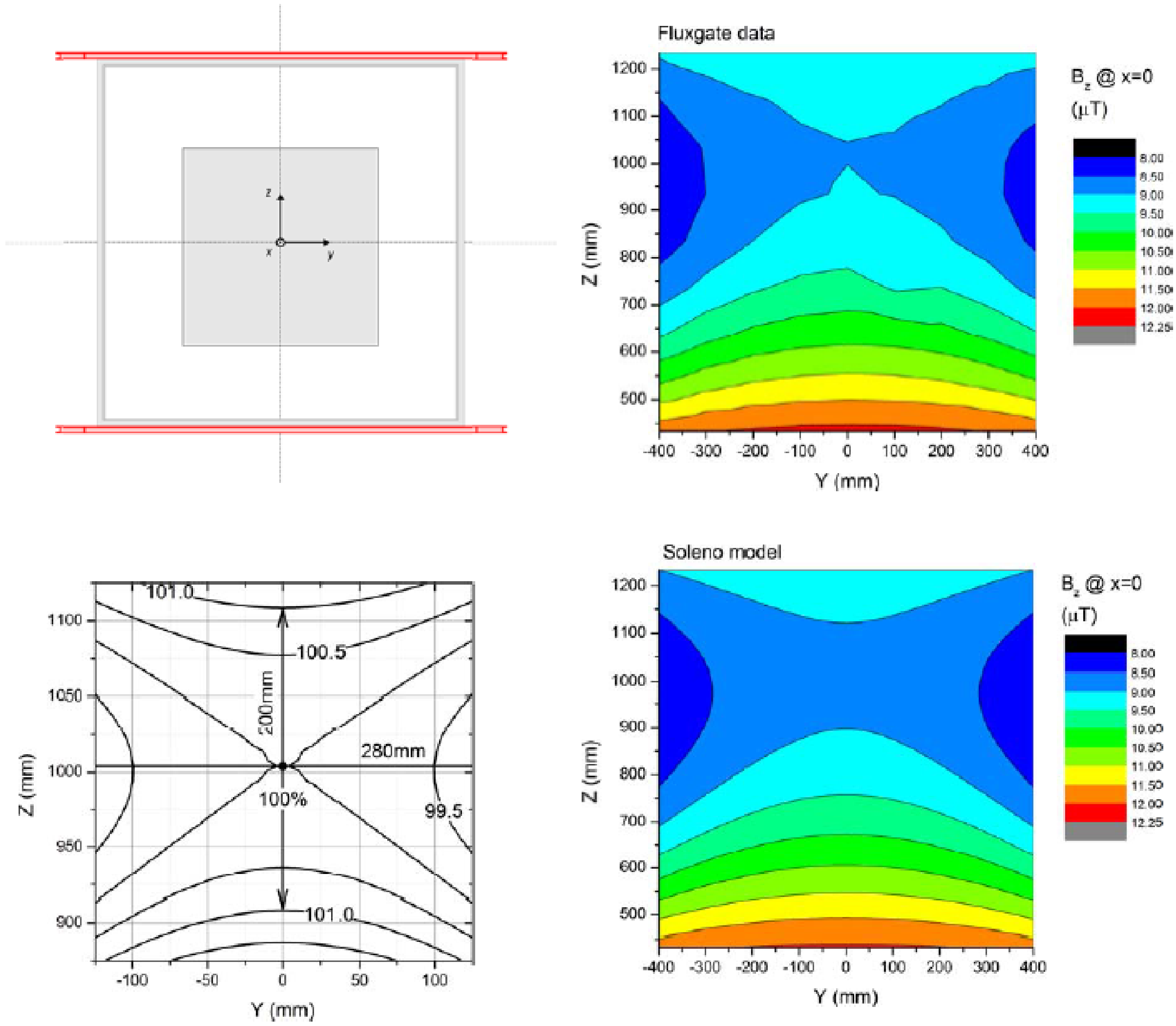

Figure B.11: *Measured and modeled data of the z-coil field in the zy-plane, at $x = 0\,mm$.*

<u>Z-coil field: z-component at *y* = 0</u> (0.1A coil current)

Standard deviation data/model 82nT

Modeled coil constant in center 88.9 µT/A

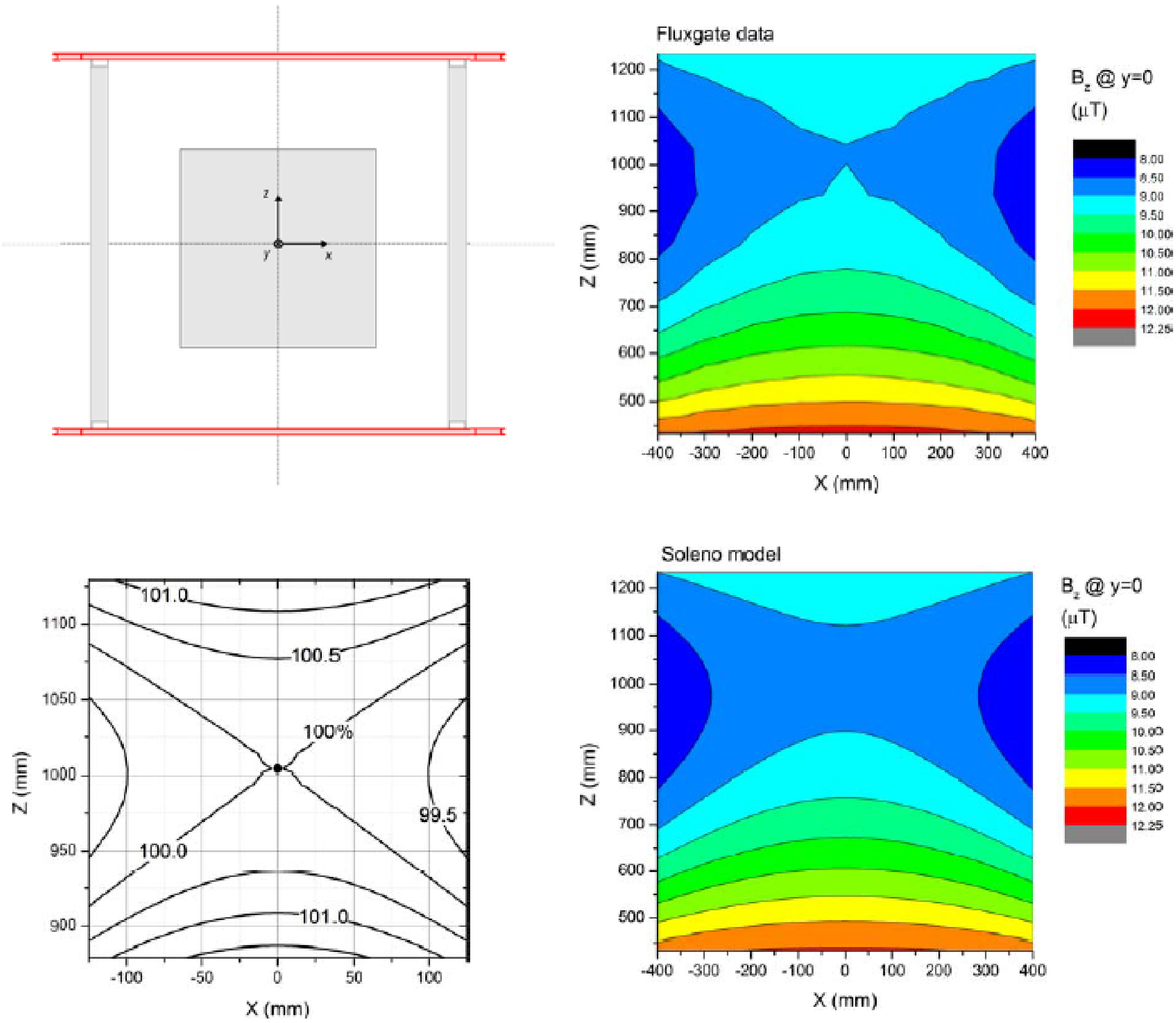

Figure B.12: *Measured and modeled data of the z-coil field in the zx-plane, at* $y = 0\,mm$.

Z-coil field: z-component at *z* = 984mm (0.1A coil current)

Standard deviation data/model 103nT

Modeled coil constant in center 88.9 μT/A

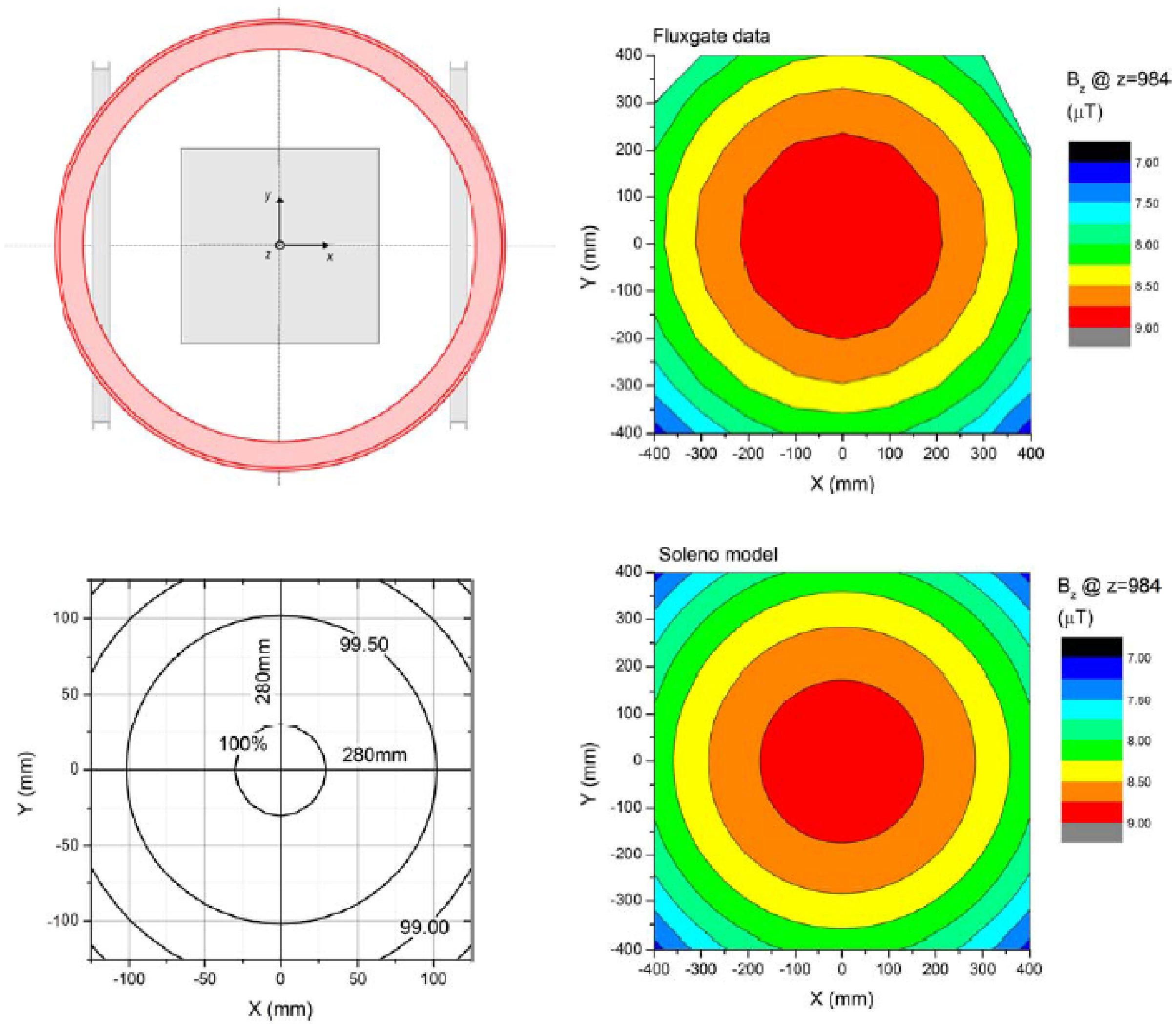

Figure B.13: *Measured and modeled data of the z-coil field in the yx-plane, at* $z = 984\,mm$.